

Series in Astronomy and Astrophysics

STELLAR EXPLOSIONS

Hydrodynamics and Nucleosynthesis

Jordi José

Department of Physics, Technical University of Catalonia (UPC), Barcelona



CRC Press

Taylor & Francis Group

Boca Raton London New York

CRC Press is an imprint of the
Taylor & Francis Group, an **informa** business

CRC Press
Taylor & Francis Group
6000 Broken Sound Parkway NW, Suite 300
Boca Raton, FL 33487-2742

© 2016 by Taylor & Francis Group, LLC
CRC Press is an imprint of Taylor & Francis Group, an Informa business

No claim to original U.S. Government works

Printed on acid-free paper
Version Date: 20151110

International Standard Book Number-13: 978-1-4398-5306-1 (Hardback)

This book contains information obtained from authentic and highly regarded sources. Reasonable efforts have been made to publish reliable data and information, but the author and publisher cannot assume responsibility for the validity of all materials or the consequences of their use. The authors and publishers have attempted to trace the copyright holders of all material reproduced in this publication and apologize to copyright holders if permission to publish in this form has not been obtained. If any copyright material has not been acknowledged please write and let us know so we may rectify in any future reprint.

Except as permitted under U.S. Copyright Law, no part of this book may be reprinted, reproduced, transmitted, or utilized in any form by any electronic, mechanical, or other means, now known or hereafter invented, including photocopying, microfilming, and recording, or in any information storage or retrieval system, without written permission from the publishers.

For permission to photocopy or use material electronically from this work, please access www.copyright.com (<http://www.copyright.com/>) or contact the Copyright Clearance Center, Inc. (CCC), 222 Rosewood Drive, Danvers, MA 01923, 978-750-8400. CCC is a not-for-profit organization that provides licenses and registration for a variety of users. For organizations that have been granted a photocopy license by the CCC, a separate system of payment has been arranged.

Trademark Notice: Product or corporate names may be trademarks or registered trademarks, and are used only for identification and explanation without intent to infringe.

Visit the Taylor & Francis Web site at
<http://www.taylorandfrancis.com>

and the CRC Press Web site at
<http://www.crcpress.com>

1

Computational Hydrodynamics

“For many problems in the theory of the stellar interior the speed of numerical integrations by hand is entirely sufficient. A person can usually accomplish more than twenty integration steps per day for a set of differential equations [...] Thus for a typical single integration consisting of, say, forty steps less than two days are needed. Correspondingly, if, for example, a set of models is to be determined and if these models are to be constructed of a one-parameter family starting from the surface and a one-parameter family starting from the core, and if each of these two families can be represented with sufficient accuracy by, say, six individual integrations, then the entire numerical work for this fairly typical case can be accomplished by one person in one month. However, if extensive evolutionary model sequences including a variety of physical complications are to be derived, then numerical integrations by hand may become prohibitive and the advantage of large electronic machines will be incontestable.”

Martin Schwarzschild, *Structure and Evolution of the Stars* (1958)

The big picture that emerged from the theory of stellar evolution owes substantial credit to computational astrophysics. Certainly, a number of observational breakthroughs have helped to pave the road by shedding light onto long-standing enigmas of the physics of stars. But only through numerical simulation have astrophysicists witnessed the full lifecycle of a star, from birth to death, spanning millions/billions of years of evolution, or have experienced the extreme conditions that characterize stellar interiors during their titanic explosions. Computational astrophysics has experienced a dramatic progress in recent years. The computational capabilities now available (Figure 1.1) were just a dream a few decades ago. Indeed, the concept of numerical models *integrated by hand*, as stressed in the quote from Martin Schwarzschild, can hardly be taken seriously anymore, in the era of state-of-the-art, multidimensional simulations.

Stars can be described by the set of conservation equations of fluid dynamics (i.e., mass, energy, and momentum conservation), together with supplementary relations that account for energy production (e.g., nuclear reactions), energy transport (by radiation, conduction, or convection), plus a suitable equation of state that describes the thermodynamics of the fluid. The evolution of continuous, Newtonian fluids¹ can be described by the Navier–Stokes equations, a set of nonlinear, partial differential equations with no known analytical solu-

¹Fluids are often classified according to different properties. For instance, we distinguish between compressible and incompressible fluids, depending whether they undergo significant changes in density as they flow. Even though all real fluids are compressible, to some extent, liquids can be approximated as incompressible fluids; gases, instead, are highly compressible. Viscous forces acting on a fluid can be large or small compared to inertial forces. This yields to the distinction between viscous and inviscid fluids. Inviscid flows, for instance, are characterized by a *Reynolds number* $R_e \gg 1$ (i.e., ratio of inertial to viscous forces defined as $R_e = \rho u L / \mu$, where ρ is the density, u the velocity, L a characteristic length, and μ the dynamic viscosity of the fluid). Fluids are called Newtonian (non-Newtonian) when the viscous stresses arising from their flow are (are not) linearly proportional to the local strain rate, or rate of variation of its deformation over time. Finally, we can distinguish between laminar and turbulent flows, depending on the way the fluid flows (in parallel vs. random, superposed layers). Flows characterized by $R_e > 5000$ are typically—but not necessarily!—turbulent, while those at low Reynolds numbers usually remain laminar. In the case of a flow moving through a straight pipe with a circular cross-section, transition between laminar and turbulent flows occurs at a Reynolds number of ~ 2000 .

**FIGURE 1.1**

The MareNostrum supercomputer, located inside an ancient chapel at the Technical University of Catalonia (UPC, Barcelona). In its current configuration, MareNostrum has 48,896 Intel SandyBridge processors in 3056 nodes, and 84 Xeon Phi 5110P in 42 nodes, with a peak performance of 1.1 petaflops. A color version of this picture is available at <http://fisica.upc.edu/ca/users/jjose/CRC-Downloads>. Image courtesy of Barcelona Supercomputing Center (www.bsc.es).

tion. Unless a number of simplifications are introduced, Navier–Stokes equations require a numerical approach. To this end, they have to be rewritten in a suitable, computer-friendly form (e.g., finite differences, finite elements, particles) that does not always bear full resemblance to the original equations. In this framework, numerical solutions have to be taken with caution and must be considered only as approximate solutions. Indeed, the robustness of the solution has to be checked against any control parameter or simplification undertaken (e.g., from time-step constraints to the size of the computational domain, or the resolution adopted). From a wider perspective, numerical codes should undergo extensive verification and validation, testing their performance in the framework of physical problems with a well-established solution. Unfortunately, test problems with analytical solution are frequently so simple that only a subset of modules or subroutines, rather than the full performance of the code, are actually checked. A thorough comparison of results obtained with similar codes turns out to be a reliable alternative, although it is hard to overcome the natural reluc-tancy of competing teams in sharing information to this end. Intuition on the behavior of the expected solution may also help (particularly when intuition proves right, which is not

always the case!). Laboratory experiments offer an appealing but challenging alternative for validation of numerical codes. However, the framework in which such experiments can be actually conducted is often far from the conditions achieved in the stellar interiors. Besides, one can easily figure out the problems faced by experiments aimed at validating models of thermonuclear explosions, not only because of the extreme physical conditions required, but also because of the classified nature of such tests.

The arsenal of mathematical methods used in astrophysics encompasses many aspects of linear algebra and calculus (in particular, the solution of ordinary and partial differential equations). This is a very rich field, certainly too broad for an in-depth analysis in an introductory book on stellar explosions. Interested readers can find a wealth of information on these topics in many specialized publications [209, 227, 637, 1448, 1500, 1812]. This chapter, instead, specifically focuses on the realm of stellar evolution codes (with particular emphasis on Lagrangian hydrodynamic formulations), reviewing the basic equations of stellar physics, the numerical techniques frequently adopted, and a suite of specific hydrodynamic concepts often encountered at different stages during the evolution of stars [209, 279, 988, 1083, 1634].

1.1 To Grid or Not to Grid: A Primer on Hydrocodes

Fluids are substances (i.e., liquids, gases, plasmas, and even solids with large plasticity) that deform under the influence of shear stresses. As such, they are ubiquitous in the universe on all scales, which in turn makes fluid dynamics one of the widest research areas, with interests spanning from weather predictions to airplane design, or stellar evolution. Even though the physical conditions describing a star or, say, a terrestrial cloud (e.g., temperature, density, pressure ...) differ by orders of magnitude, the numerical tools used in their analyses share many common features and rely on a similar set of coupled, partial differential equations, which are not usually amenable to analytical solutions, except under highly restrictive conditions. Numerical solutions are actually obtained for a finite, discrete number of points of the computational domain (either a volume, a surface, or a line), which often, but not always, relies on a computational mesh or grid, representing a subdivision of the domain into cells or elements. These computational domains can be mapped by means of structured and unstructured (or even hybrid) meshes. Structured (or regular) meshes are families of gridlines, topologically equivalent to Cartesian grids. They are usually applied to simple computational domains, since complex problems may result in unwanted grid distortions and consequently may lead to a computational failure. Unstructured meshes instead are more versatile and better suited for arbitrary domains. However, they are more difficult to implement. All numerical methods that rely on a mesh, whether structured or not, are usually referred to as *grid-* or *mesh-based* methods. In contrast, *gridless* or *meshfree* methods directly rely on the simulated object, avoiding mesh tangling and distortion, which are frequently encountered in traditional mesh-based methods in the presence, for instance, of nonlinear behavior, discontinuities, or singularities.

Two different prescriptions are frequently adopted in the analysis of fluid flows (see Figures 1.2 and 1.3). In the first one, a computational grid is attached to the fluid, which yields what is commonly termed as Lagrangian (or comoving) representation. A second approach relies on a reference frame that is fixed in space, allowing material to flow through the grid. This yields a Eulerian representation².

²Some codes combine the best of both worlds into what is known as an Arbitrary Lagrangian–Eulerian (ALE) approach. See Hirt, Amsden, and Cook [808] for the pioneering paper on ALE methods.

**FIGURE 1.2**

A diving sequence is followed by means of a Lagrangian grid attached to the diver. Severe grid distortion and tangling results. Obviously, the diver will never leave the computational domain. A color version of this picture is available at <http://fisica.upc.edu/ca/users/jjose/CRC-Downloads>. Diver sequence by Jennifer Williams; reproduced with permission. Artwork by h2o creative communications Ltd.

Let's consider a scalar variable T (e.g., temperature) that depends upon position, r , and time, t . In the Eulerian approach, the total rate of change of T is simply given by $\partial T / \partial t$, evaluated at a fixed location, r . In the Lagrangian approach, however, the total rate of

**FIGURE 1.3**

Same as Fig. 1.2, but for a Eulerian grid fixed in space. No grid distortion results, although the diver, who moves across the grid, may leave the computational domain. A color version of this picture is available at <http://fisica.upc.edu/ca/users/jjose/CRC-Downloads>.

change of variable T (also known as material or substantial time derivative) is expressed as:

$$\frac{DT}{Dt} = \frac{\partial T}{\partial t} + \frac{\partial T}{\partial x} \frac{dx}{dt} + \frac{\partial T}{\partial y} \frac{dy}{dt} + \frac{\partial T}{\partial z} \frac{dz}{dt} \quad (1.1)$$

Interpreting the time derivatives of the space coordinates x, y, z as components of a (Eu-

lerian) velocity vector, the material time derivative can be written as:

$$\frac{DT}{Dt} = \frac{\partial T}{\partial t} + \frac{\partial T}{\partial x} v_x + \frac{\partial T}{\partial y} v_y + \frac{\partial T}{\partial z} v_z \quad (1.2)$$

or in a more compact form,

$$\frac{DT}{Dt} = \frac{\partial T}{\partial t} + \vec{v} \cdot \nabla T, \quad (1.3)$$

with ∇T being the gradient of variable T . Whereas DT/Dt represents the time derivative of T for a moving fluid element (Lagrangian frame), $\partial T/\partial t$ is the local time derivative of T at a fixed point (Eulerian frame), and $\vec{v} \cdot \nabla T$ represents an advective change (also known as *convective* velocity) driven by the fluid displacement.

By construction, the independent variables used in Lagrangian formulation are mass, m , and time, t , whereas spatial coordinates, r , and time, t , are better suited for Eulerian formulations. Transformation between the two coordinates m and r is handled through application of the chain's rule. For spherical coordinates,

$$\frac{\partial}{\partial m} = \frac{\partial}{\partial r} \frac{\partial r}{\partial m} = \frac{1}{4\pi r^2 \rho} \frac{\partial}{\partial r}. \quad (1.4)$$

Both Lagrangian and Eulerian approaches present pros and cons, and no obvious choice can be made *a priori*. For non-turbulent fluids, Lagrangian formulation is probably the simplest choice, since the grid is directly attached to the fluid, and therefore boundary conditions are easy to implement. Moreover, mass is conserved by default, since no material is transferred between adjacent cells. However, since the computational grid moves with the fluid, severe mesh distortion may result. In the Eulerian approach, the computational grid is fixed and the fluid may flow through the mesh. Boundary conditions are therefore harder to implement, since fluid boundaries do not necessarily coincide with the edges of the computational domain. An advantage with respect to a Lagrangian frame is the lack of distortion, since a Eulerian grid is fixed in space. Nevertheless, Eulerian grids are usually larger than their Lagrangian counterparts, as there is some risk that the fluid may leave the computational domain (particularly in rapid fluid flows like those characterizing stellar explosions).

To date, detailed nucleosynthesis simulations coupling hydrodynamics and large nuclear reaction networks have mostly been performed with Lagrangian, 1D codes³, since Lagrangian frames do not induce artificial mixing between adjacent cells. In 2D and 3D, turbulent flows may cause large distortions of a Lagrangian grid, and, accordingly, a Eulerian approach is frequently adopted.

Different discretization strategies can be implemented to transform the original set of coupled, partial differential equations into a system of algebraic equations that could be solved numerically (that is, the mathematical model describing the system in a continuous way is discretized in space and transformed into a discrete model with a finite number of degrees of freedom). Finite differences are a form of discretization frequently adopted in stellar evolution codes⁴. They are simple and effective, although their applicability is restricted to structured meshes. In this technique, variables are assigned to individual grid points (either

³According to Bill Rider (Sandia National Labs), the first hydrodynamic calculation appeared in a report from Los Alamos National Laboratory on June 20, 1944. The leading author was Hans Bethe, while the calculation leader was Richard Feynman. The work is still classified. The first codes were 1D and Lagrangian. Eulerian codes were first developed for weather prediction and used in weapons labs already in the mid-1950s.

⁴Other techniques, widely used in physics and engineering, include finite element methods, finite volume methods, spectral methods (which are based on global transformations of the system of equations—often

located at the edges, corners, or centers of each computational cell; see Section 1.4.1), and the corresponding derivatives are evaluated as differences of variables in neighboring cells.

Let's consider, for instance, a given function $F(x, t)$. For a fixed time, t , F can be approximated by means of a Taylor series expansion, in the form

$$F(x_o + \Delta x) = F(x_o) + \left(\frac{\partial F}{\partial x} \right)_{x_o} \Delta x + \left(\frac{\partial^2 F}{\partial x^2} \right)_{x_o} \Delta x^2 + O(\Delta x^3). \quad (1.5)$$

Truncation of the Taylor polynomial to first order yields

$$\left(\frac{\partial F}{\partial x} \right) = \frac{F(x_o + \Delta x) - F(x_o)}{\Delta x}, \quad (1.6)$$

which corresponds to the first-order space derivative of F in a forward-difference approximation (that is, between x_o and the *next* grid point located at $x_o + \Delta x$). A similar expression, the backward-difference approximation, results from a Taylor expansion of F between x_o and $x_o - \Delta x$:

$$\left(\frac{\partial F}{\partial x} \right) = \frac{F(x_o) - F(x_o - \Delta x)}{\Delta x}, \quad (1.7)$$

which, like the forward-difference expression, is first-order accurate. Any of these finite-difference expressions can be used in principle to approximate space derivatives and therefore turn out to be essential in the numerical analysis of differential equations. However, in the process of replacing differential equations by algebraic equations based on finite differences, unexpected surprises may arise. Truncation errors, for instance, can lead to unacceptable solutions when many integration steps are required and first-order, finite-difference expressions may no longer be appropriate. Often, more complex numerical schemes are required to handle differential equations efficiently⁵. This reflects the intricacies and difficulties in the art of numerical modeling. As an example, combining both forward- and backward-Taylor expansions of F up to third order, one gets:

$$\left(\frac{\partial F}{\partial x} \right) = \frac{F(x_o + \Delta x) - F(x_o - \Delta x)}{2\Delta x}, \quad (1.8)$$

relying on Fourier transforms—into a sum of functions that must satisfy the original differential equations [864]), and meshfree methods (like the *smoothed-particle hydrodynamics*, or *SPH* method; see Section 1.5).

Finite elements and finite volumes are particularly suited for arbitrary meshes (unstructured grids, in particular). Finite elements operate by splitting the domain of the problem into a number of subdomains, called *finite elements*, each represented by a set of equations [250, 912]. But in contrast to the direct (*strong-form*) approach adopted in finite difference techniques (also in SPH), by which the partial differential equations are directly discretized and solved, finite element methods rely on an indirect or *weak-form* approach, in which the original equations are transformed, often in integral form, on the basis of trial solutions and weighting functions. The collection of local equations is then reassembled into a global system of equations through a transformation of coordinates.

Finite-volume methods [507, 1855] are gaining popularity as a suitable form of discretization in multidimensional codes. They are somewhat similar to finite-difference and finite-element methods, since they rely on the discretization of a system of partial differential equations onto a discrete set of points of a grid-based geometry. To this end, the computational domain is divided into a set of discrete, nonoverlapping discretization cells or *control volumes*, with physical variables assigned to the centroid of each control volume. The set of partial differential equations is then integrated over each control volume, resulting in balance equations that are subsequently discretized. The cornerstone of finite-volume methods is the discretization of the fluxes at the boundaries of each control volume. This discretization technique guarantees conservation of physical magnitudes for any control volume as well as for the overall computational domain. Note that discretization is again performed on local balance equations rather than on the original partial differential equations (as in finite-differences). For more information on these and other methods used in computational fluid dynamics, the reader is referred to LeVeque et al. [1083] and Toro [1812].

⁵See, e.g., Fryxell, Müller, and Arnett [566], Benz [153], Gershenfeld [637], or Bodenheimer, Laughlin, Różyczka, and Yorke [209] for a detailed account on the most extensively used numerical schemes (e.g., Lax–Wendroff, Crank–Nicolson, DuFort–Frankel, Gauss–Seidel, Jacobi, alternating direction implicit (ADI) methods).

which is second-order accurate, while being as simple to implement as any of the former, first-order expressions.

1.1.1 From One-Zone Models to Multidimensional Codes

The specific literature on stellar explosions and their associated nucleosynthesis is sometimes confusing with regard to the numerical tools undertaken in the study of such events. In fact, it is extremely important to clarify the framework in which such simulations have been performed to properly assess the applicability and generality of the conclusions reached.

One-zone models have extensively been used in nucleosynthesis studies of classical novae and X-ray bursts (see Chapters 4 and 6). They rely on the time evolution of the temperature, T , and density, ρ , of a selected single layer. Such thermodynamic quantities are calculated by means of semianalytical models, or correspond to T - ρ profiles directly extracted from hydrodynamic simulations. This approach, while representing an extreme oversimplification of the physical conditions governing a star, has been widely used to overcome the time limitations that arise when large nuclear reaction networks are coupled to computationally intensive numerical codes. More recently, one-zone models have also been used to estimate the impact of nuclear uncertainties on the final yields, in a number of astrophysical sites (e.g., classical novae [880], or type I X-ray bursts [1385, 1386]), requiring thousands of test calculations that would be prohibitive with standard hydrodynamic codes. A somewhat related approach involves postprocessing, multizone calculations based on a suite of T - ρ profiles extracted from hydrodynamic simulations at different locations of the computational domain. This has extensively been used, for instance, in supernova nucleosynthesis calculations (see Chapters 5 and 7), as well as in reaction-rate sensitivity studies [1388].

The state-of-the-art modeling of stellar explosions and nucleosynthesis relies, however, on *hydrodynamic models*. Until the 1990s, most of the available hydro codes were 1D, that is, assumed spherical symmetry. This simplifying hypothesis excludes an entire sequence of events in the modeling of stellar explosions, for instance, the way in which an ignition front develops and propagates. In fact, spherical symmetry demands that ignition simultaneously occurs along a spherical shell, while it most likely initiates at one, maybe several, spots. Moreover, 1D models face severe limitations in the treatment of convective mixing, a key mechanism for energy transport in stars that can only accurately be modeled in three dimensions (see Section 1.2.4.3).

Multidimensional models are extremely time consuming and often require the use of parallelization techniques to distribute the overwhelming computational load among different processors. There has been a large number of multidimensional simulations of supernova explosions to date. In sharp contrast, multidimensional models of novae or X-ray bursts have been not only scarce, but limited to somewhat small computational domains (i.e., a box containing a fraction of the overall star) and to reduced nuclear reaction networks that include only a handful of isotopes to approximately account for the energetics of the explosion. Hence, while appropriate to tackle key phenomena that truly require a three-dimensional approach (e.g., convection and mixing, turbulence, shear), multidimensional models still need to rely on postprocessing techniques for detailed nucleosynthesis studies that require huge nuclear reaction networks.

1.2 Equations of Stellar Structure

Stars are massive spheres of plasma held together by gravity. Indeed, gravity is the driving force behind stellar evolution, leading the way toward thermonuclear fusion through matter compression (see Chapter 2). The structure of a star is stabilized by the internal (thermal) pressure, which prevents the otherwise inevitable collapse. Indeed, when these two forces—gravity and pressure—are not in balance, the star destabilizes, and a suite of different explosive events may result (see Chapters 4–7). Stars are also characterized by an internal energy source, often powered by thermonuclear processes—although occasionally driven by gravitational contraction. A fraction of this energy, transported through the star either by radiation, convection, or conduction, is ultimately emitted into space. In this framework, a star can be described by a set of conservation equations (mass, momentum, and energy), energy sources, and transport mechanisms:

- Mass conservation
- Momentum conservation
- Energy conservation
- Energy transport

These four basic equations, supplemented by a suitable equation of state, an account of the main processes contributing to stellar opacity (a measure of how opaque—transparent—the plasma is to the radiation field), and to nuclear energy generation and nucleosynthesis, constitute the building blocks of a stellar evolution code⁶.

The simplest, commonly used stellar codes rely on spherical symmetry, and on the assumption of local thermodynamic equilibrium (LTE), under which temperature is assumed to be identical both for matter and radiation (photons). This approximation often turns out to be appropriate, since the photon mean free path, or average distance covered between successive collisions, is much smaller than the length over which the temperature varies substantially. In the following subsections, we will describe the basic equations of stellar structure under these assumptions and will later reconsider their validity.

1.2.1 Mass Conservation: The Continuity Equation

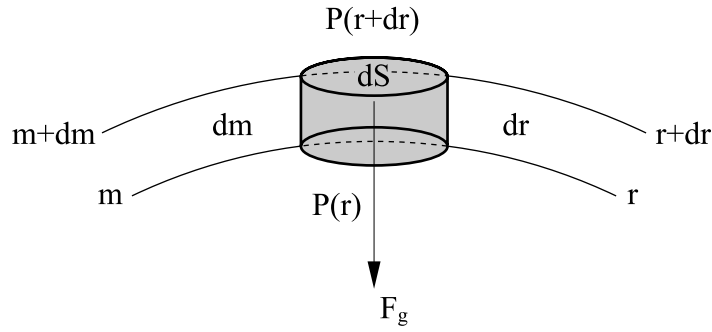
Let's consider a tiny element of mass dm within a star, small enough to guarantee that its temperature, density, and chemical composition are approximately uniform.

In spherical symmetry, dm corresponds to a thin shell comprised between radii r and $r + dr$ (Figure 1.4), hence occupying a volume $dv = 4\pi r^2 dr$. In terms of the density, ρ ,

$$dm = \rho dv = \rho 4\pi r^2 dr. \quad (1.9)$$

Under the assumption of spherical symmetry, the physical properties that characterize a star depend only on the radial distance from its center, r . Unfortunately, it is often the case that the radius of a star varies dramatically by orders of magnitude during the course of its evolution. Hence, relying on the mass enclosed in a sphere of radius r (hereafter, $m(r)$)

⁶Two types of stellar evolution codes are usually mentioned in the literature: hydrostatic and hydrodynamic. Essentially, they rely on the same set of equations, but hydrodynamic codes allow for an acceleration term, du/dt , in the momentum conservation equation, resulting from the imbalance between the gravitational force and the pressure gradient. When $du/dt = 0$, as in hydrostatic codes, the momentum conservation equation simply reduces to the hydrostatic equilibrium equation.

**FIGURE 1.4**

Schematic of the relevant forces acting on a mass element, dm , located at a distance r from the center of a star.

rather than on the radial distance itself, turns out to be more useful. Note that $m(r)$ acts exactly as a pointlike mass located at the stellar center exerting an inward gravitational acceleration equal to $G m(r)/r^2$.

Rearranging terms in Equation 1.9, one obtains:

$$V \equiv \frac{1}{\rho} = 4\pi r^2 \frac{\partial r}{\partial m} = \frac{4}{3}\pi \frac{\partial r^3}{\partial m}, \quad (1.10)$$

where V is known as the specific volume. Equation 1.10 is usually referred to as the *mass conservation* or *continuity* equation.

1.2.2 Energy Conservation

The first law of thermodynamics, an expression of the principle of energy conservation, states that the internal energy of a system can be modified by heat exchange and work. If δQ is the amount of heat absorbed (> 0) or emitted (< 0) by a mass element dm , and δW the work done on dm over a time δt , the change in internal energy per unit mass, δE , can be expressed as:

$$\delta E dm = \delta Q + \delta W. \quad (1.11)$$

The work done on the system (contraction) is taken as $-P dv$, whereas the work done by the system during expansion is $P dv$. Therefore, one can write:

$$\delta W = -P \delta(dv) = -P \delta \left(\frac{dv}{dm} dm \right) = -P \delta \left(\frac{1}{\rho} \right) dm, \quad (1.12)$$

where mass conservation has been assumed. Note that a compression ($\delta(dv) < 0$) requires an addition of energy to the mass element, whereas an expansion ($\delta(dv) > 0$) is achieved at the expense of the element's own energy.

Two sources of heat for a mass element dm can be considered:

- Nuclear energy, often expressed in terms of an energy generation rate, ε , or energy released per unit mass and unit time.
- The net balance of energy fluxes entering/leaving the mass element, expressed in terms of the luminosity, L , or energy flux per unit time.

Hence, for a spherically symmetric thin shell (Figure 1.4), we have:

$$\delta Q = \varepsilon dm \delta t + L(m) \delta t - L(m + dm) \delta t. \quad (1.13)$$

Using a first-order Taylor expansion of $L(m + dm)$, in the form

$$L(m + dm) = L(m) + \left(\frac{\partial L}{\partial m} \right) dm, \quad (1.14)$$

Equation 1.13 can be rewritten as:

$$\delta Q = \left[\varepsilon - \left(\frac{\partial L}{\partial m} \right) \right] dm \delta t. \quad (1.15)$$

Plugging Equations 1.12 and 1.15 into Equation 1.11, one gets

$$\delta E dm = \delta Q + \delta W = \left[\varepsilon - \left(\frac{\partial L}{\partial m} \right) \right] dm \delta t - P \delta \left(\frac{1}{\rho} \right) dm. \quad (1.16)$$

Eliminating dm ,

$$\delta E = \left[\varepsilon - \left(\frac{\partial L}{\partial m} \right) \right] \delta t - P \delta V \quad (1.17)$$

and rearranging terms, one finally gets the *energy conservation equation*

$$\frac{\partial E}{\partial t} = \varepsilon - \frac{\partial L}{\partial m} - P \frac{\partial V}{\partial t}. \quad (1.18)$$

Note that under thermal equilibrium conditions (i.e., $\frac{\partial}{\partial t} = 0$), Equation 1.18 reduces to

$$\varepsilon = \frac{\partial L}{\partial m}. \quad (1.19)$$

The previous expression can be integrated over the entire star, in the form

$$\int_o^M \varepsilon dm = \int_o^M dL, \quad (1.20)$$

where $\int_o^M dL$ corresponds to the overall luminosity of the star, L . Defining $\int_o^M \varepsilon dm$ as a *nuclear luminosity*, L_{nuc} , or energy released by nuclear processes per unit time, one finally gets

$$L = L_{\text{nuc}}. \quad (1.21)$$

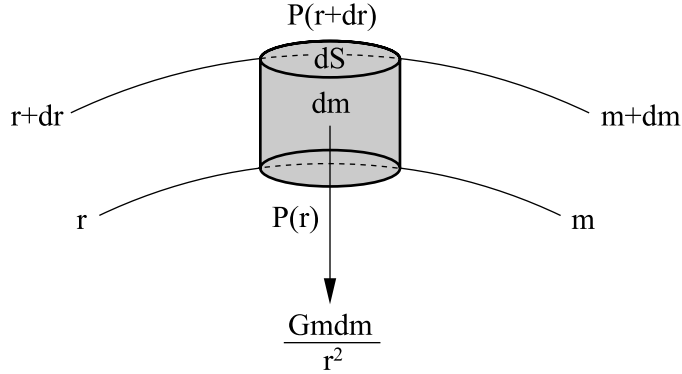
1.2.3 Momentum Conservation

Newton's second law states that the net force acting on a body (of constant mass) leads to its acceleration, in the form $a = F/m$. More generally, the net force applied to a body is equal to the time derivative of its momentum, $F = dp/dt$, with $p = mv$.

Let's now consider a small cylindrical volume element within a star, dv , with a cross-sectional area dS , and an axis of length dr , radially comprised between r and $r + dr$. The mass contained in this volume element can be expressed as:

$$dm = \rho dv = \rho dr dS. \quad (1.22)$$

As shown in Figure 1.5, the forces acting on the volume (mass) element are:

**FIGURE 1.5**

Net forces acting on a volume (mass) element within a star.

- The gravitational force, $-G m dm/r^2$, exerted onto a mass element dm by the mass m enclosed in a sphere of radius r , as described by Gauss's law for gravity.
- Forces associated with the pressure gradient along the surrounding gas.

In this context, the equation of motion for the mass element dm can be written as:

$$dF = dm a \rightarrow -Gm \frac{dm}{r^2} + P(r) dS - P(r+dr) dS = \frac{\partial^2 r}{\partial t^2} dm. \quad (1.23)$$

Note that pressure forces acting on both vertical sides of the cylinder (Figure 1.5) cancel mutually in the framework of spherical symmetry.

Equation 1.23 can be rearranged by using a first-order Taylor expansion of $P(r+dr)$ in the form:

$$P(r+dr) = P(r) + \left(\frac{\partial P}{\partial r} \right) dr, \quad (1.24)$$

which leads to

$$\frac{\partial^2 r}{\partial t^2} dm = -Gm \frac{dm}{r^2} - \left(\frac{\partial P}{\partial r} \right) dr dS = -Gm \frac{dm}{r^2} - \left(\frac{\partial P}{\partial r} \right) \frac{dm}{\rho}. \quad (1.25)$$

Dividing all terms by dm ,

$$\frac{\partial^2 r}{\partial t^2} = -G \frac{m}{r^2} - \left(\frac{\partial P}{\partial r} \right) \frac{1}{\rho}, \quad (1.26)$$

replacing the second-order space derivative by the first-order derivative of the velocity, u , and applying the chain's rule to transform $\frac{\partial P}{\partial r}$ into $\frac{\partial P}{\partial m}$ as follows,

$$\frac{\partial P}{\partial r} = \frac{\partial P}{\partial m} \frac{\partial m}{\partial r} = \rho 4\pi r^2 \frac{\partial P}{\partial m}, \quad (1.27)$$

one finally obtains the *momentum conservation* equation:

$$\frac{\partial u}{\partial t} = -G \frac{m}{r^2} - 4\pi r^2 \left(\frac{\partial P}{\partial m} \right). \quad (1.28)$$

If the acceleration term becomes negligible, Equation 1.28 reduces to the *hydrostatic equilibrium* equation:

$$\frac{\partial P}{\partial m} = -\frac{Gm}{4\pi r^4}. \quad (1.29)$$

It is worth noting that since the right-hand side of this equation is always negative, P must decrease outward.

1.2.4 Energy Transport

The energy emitted by a star through its surface frequently originates from deep inside reservoirs. Radiation, conduction, and convection are the mechanisms by which heat, and sometimes blobs of matter, can be carried throughout the star, aided by a temperature gradient between the central, hot layers (occasionally, the envelope base, like in novae or X-ray bursts) and the outer, cooler regions.

1.2.4.1 Radiation

Radiative transfer is a mechanism of energy transport by means of electromagnetic radiation—that is, photons. In their voyage through the dense stellar plasma, photons are affected by absorption, emission, and scattering processes, resulting from the tight interaction between radiation and matter.

Analytic solutions to the differential equation governing radiative transfer only exist for simple cases, because of the complexity posed by the multiple interactions faced by photons and the fact that radiation is emitted from the source in various directions and at different energies—or, equivalently, frequencies.

The distance travelled by a photon between two consecutive interactions is known as the *mean free path*, l_{phot} , and is given by:

$$l_{\text{phot}} = \frac{1}{\kappa\rho}, \quad (1.30)$$

where κ is the mean absorption coefficient or opacity (a measure of the cross-section or probability of interaction per unit mass and averaged over frequency).

For a star like the Sun, the mean free path of a photon, based on average values for the density and opacity (i.e., $\rho \sim 1 \text{ g cm}^{-3}$, $\kappa \sim 1 \text{ cm}^2 \text{ g}^{-1}$), is about $\sim 1 \text{ cm}$ (i.e., the Sun is nearly opaque to radiation). This is very short⁷, compared with the typical length scale at which structural changes occur within the star. Since the temperature gradient between the center and the surface of the Sun is $dT/dr \sim 10^{-4} \text{ K cm}^{-1}$, the radiation field is expected to be highly isotropic and close to thermal equilibrium. In such conditions, the radiation field can be approximated by a blackbody through Planck's intensity function⁸ or spectral radiance, which quantifies the power emitted by a blackbody at temperature T per unit surface area and unit solid angle at a frequency ν :

$$B_\nu(T) = \frac{2h\nu^3}{c^2} \frac{1}{e^{h\nu/kT} - 1}, \quad (1.31)$$

where h is the Planck constant, c is the speed of light in vacuum, and k is the Boltzmann constant. In thermodynamic equilibrium, the spectral radiance is related to the (spectral) energy density, $U_\nu(T)$, and to the radiation pressure, $P_{\text{rad},\nu}$, as

$$U_\nu(T) = \frac{4\pi}{c} B_\nu(T) \quad (1.32)$$

$$P_{\text{rad},\nu} = \frac{4\pi}{3c} B_\nu(T). \quad (1.33)$$

⁷Close to the center, the mean free path of a photon is even shorter because of the large local density, while it becomes longer in the outer regions (e.g., at the Sun's photosphere) following the drop in density.

⁸Note that while the radiation field is described in terms of a constant temperature, T , a net flux of radiation resulting from a nonzero (macroscopic) temperature gradient throughout the star is simultaneously assumed. This is commonly referred to as local thermodynamic equilibrium.

**FIGURE 1.6**

Radiation emitted by human bodies at infrared wavelengths ($T = 61^\circ\text{F} = 16^\circ\text{C}$). In the image, light areas are hotter than dark regions. A color version of this image is available at <http://fisica.upc.edu/ca/users/jjose/CRC-Downloads>.

Integration of the spectral radiance over the entire frequency range yields

$$B(T) = \int_0^{\infty} B_{\nu}(T)d\nu = \frac{2k^4\pi^4}{15h^3c^2}T^4 = \frac{\sigma}{\pi}T^4, \quad (1.34)$$

where σ is the Stefan–Boltzmann constant. Note that σT^4 is the power radiated by a blackbody per unit surface area across all wavelengths (Stefan’s law). Maximum emission, corresponding to a maximum of the spectral radiation function, peaks at a specific wavelength (or frequency) that depends only on the blackbody temperature, as described by Wien’s displacement law:

$$\lambda_{\max}T = 0.2898 \text{ cm K}. \quad (1.35)$$

Hence, while the Sun, characterized by a (photospheric) blackbody temperature of about 5780 K, has a peak emission at about 500 nm (i.e., visible light), mammals like humans emit predominantly in the infrared ($T \sim 310 \text{ K} \rightarrow \lambda_{\max} \sim 9 \mu\text{m}$; see Figure 1.6).

Since the mean free path of a photon in the optically thick regions of a star is very small compared with its characteristic length—the radius R —, radiative transport can be approximated as a diffusion process⁹. Accordingly, the flux of particles per unit area and unit time, \vec{j} , between two points characterized by different particle densities, n , can be expressed as [988]

$$\vec{j} = -D\nabla n, \quad (1.36)$$

where D is a diffusion coefficient determined by the average speed of the particles and their mean free path. In spherical symmetry, the radiative energy flux, F , has only a radial component. Hence, averaging over all possible wavelengths, and replacing n by the radiation energy density, $U = aT^4$, yields:

$$F = -D_{\text{rad}}\frac{\partial T}{\partial r}, \quad (1.37)$$

⁹A more detailed description of radiative transfer can be found, e.g., in references [224, 296, 1242, 1641].

where D_{rad} is the radiative diffusion coefficient defined as

$$D_{\text{rad}} = \frac{4ac}{3} \frac{T^3}{\bar{\kappa}\rho} \quad (1.38)$$

and $\bar{\kappa}$ is the average opacity integrated over the whole range of wavelengths, frequently taken as the Rosseland mean opacity,

$$\frac{1}{\bar{\kappa}} \equiv \frac{\int_0^\infty \frac{1}{\kappa_\nu} \frac{\partial B_\nu}{\partial T} d\nu}{\int_0^\infty \frac{\partial B_\nu}{\partial T} d\nu}. \quad (1.39)$$

Note that $\bar{\kappa}$ corresponds to the harmonic mean of κ_ν , with the weighting function $\partial B(T)/\partial T$. Finally, from the relationship between flux and luminosity,

$$L_{\text{rad}} = 4\pi r^2 F, \quad (1.40)$$

one gets

$$L_{\text{rad}} = -4\pi r^2 \frac{4ac}{3} \frac{T^3}{\bar{\kappa}\rho} \frac{\partial T}{\partial r}, \quad (1.41)$$

or, equivalently, an expression for the radiative temperature gradient in the diffusion approximation

$$\frac{\partial T}{\partial r} = -\frac{3}{4ac} \frac{\bar{\kappa}\rho}{T^3} \frac{L_{\text{rad}}}{4\pi r^2}. \quad (1.42)$$

1.2.4.2 Conduction

In high-density environments, like in the interior of white dwarfs, energy can be transferred through frequent collisions during the random thermal motion of the particles. If the plasma is nondegenerate or weakly degenerate, each particle has an average energy $E = \frac{3}{2}kT$, which corresponds to a velocity

$$v = \sqrt{\frac{3kT}{m}}. \quad (1.43)$$

Accordingly, electrons move faster than ions (by the square root of the mass ratio between ions and electrons), and, therefore, electrons constitute the most relevant source of heat conduction¹⁰.

By analogy with radiative transport, the electron thermal conductivity can be expressed in terms of an energy flux, in the form of a diffusion equation:

$$F_{\text{cond}} = -D_{\text{cond}} \frac{dT}{dr}, \quad (1.44)$$

with D_{cond} being a thermal diffusion coefficient that depends on the conductive opacity, κ_{cond} ,

$$D_{\text{cond}} = \frac{4acT^3}{3\kappa_{\text{cond}}\rho}. \quad (1.45)$$

Globally, the energy flux carried by radiative and conductive heat transport can be expressed as

$$F_{\text{rad+cond}} = -\frac{4ac}{3} \frac{T^3}{\kappa_{\text{ef}}\rho} \frac{dT}{dr}, \quad (1.46)$$

where

$$\frac{1}{\kappa_{\text{ef}}} = \frac{1}{\kappa_{\text{rad}}} + \frac{1}{\kappa_{\text{cond}}}. \quad (1.47)$$

¹⁰Typical densities and temperatures of main sequence stars yield mean free paths for electrons several orders of magnitude smaller than for photons. Moreover, electrons travel at velocities much smaller than the speed of light. This translates into smaller electron diffusion coefficients, compared with those for photons.

1.2.4.3 Convection

Convective transport relies on macroscopic mass elements (usually called *bubbles*, *blobs*, or *convective elements*) exchanged between hotter and cooler layers. Such convective mass elements will ultimately dissolve in the surroundings, delivering their excess heat. The description of convective heat transfer is only possible through a phenomenological approach, due to inherent uncertainties and complexity. The most widely used prescription in stellar evolution codes to date is the *mixing-length theory*, developed by Ludwig Prandtl [1443], who sketched a simple description of convection in analogy to molecular heat transfer¹¹. This theory relies on the definition of the *mixing-length*, l_m , a free parameter that measures the distance travelled by a convective blob before dissolving in the surroundings. Despite its simplicity, the mixing-length theory yields a reasonable qualitative description of convective heat transfer. However, it is important to stress that the theory assumes hydrostatic equilibrium conditions, and their implementation in the modeling of stellar explosions has to be taken with caution. Unfortunately, no self-consistent prescriptions of convective transport exist, in 1D, for dynamic conditions and theoreticians have resigned themselves to rely on the mixing-length theory for their stellar evolution—and explosion!—calculations¹².

Arguments based on the buoyancy forces acting on moving convective elements, under the assumption of pressure equilibrium between the rising bubbles and their surroundings, yield a criterion for convective instability. That is, convection settles whenever

$$\left| \frac{dT}{dr} \right| > \left| \frac{dT}{dr} \right|_{\text{ad}} \quad (1.48)$$

or, in terms of $\nabla \equiv d \ln T / d \ln P$,

$$\nabla > \nabla_{\text{ad}}, \quad (1.49)$$

where ∇ is the *actual* gradient at a given grid point, and

$$\nabla_{\text{ad}} \equiv \left| \frac{d \ln T}{d \ln P} \right|_{\text{ad}} = - \frac{P \left(\frac{\partial P}{\partial T} \right)_V}{C_p \left(\frac{\partial P}{\partial V} \right)_T} \quad (1.50)$$

is the *adiabatic* gradient. C_p is the heat capacity at constant pressure, related to the heat capacity at constant volume, C_v , through

$$C_p = C_v - T \frac{\left(\frac{\partial P}{\partial T} \right)_V^2}{\left(\frac{\partial P}{\partial V} \right)_T} = \left(\frac{\partial U}{\partial T} \right)_V - T \frac{\left(\frac{\partial P}{\partial T} \right)_V^2}{\left(\frac{\partial P}{\partial V} \right)_T}. \quad (1.51)$$

Equation 1.49 is known as the *Schwarzschild criterion* for convection. A related expression, the *Ledoux criterion*, is used for chemically inhomogeneous regions:

$$\nabla > \nabla_{\text{ad}} + \frac{\phi}{\psi} \left(\frac{\partial \ln \mu}{\partial \ln P} \right)_{\rho, T}, \quad (1.52)$$

where

$$\phi = \left(\frac{\partial \ln \rho}{\ln \mu} \right)_{P, T} \quad (1.53)$$

¹¹See also Böhm-Vitense [214] and Cox and Giuli [384] for early detailed descriptions of the mixing-length theory. The classic Cox and Giuli book has been recently revised and extended by A. Weiss, W. Hillebrandt, H.-C. Thomas, and H. Ritter [1919].

¹²The rise of multidimensional simulations has allowed ways to overcome this limitation through the implementation of prescriptions based on 3D models of convection [70, 71, 1222, 1251].

$$\psi = - \left(\frac{\partial \ln \rho}{\ln T} \right)_{P,\mu}. \quad (1.54)$$

In the mixing-length theory, the myriad convective bubbles, characterized by a suite of different sizes, shapes, velocities, and lifetimes, are somewhat *averaged*, so that all bubbles located at a given distance r from the stellar center have the same physical properties.

A rising bubble is characterized by a lower density than the surroundings. Because of the assumption of pressure equilibrium, a lower density implies a higher temperature, and therefore, a rising bubble implies a thermal energy transport upwards. In mixing length theory, hot bubbles rise, traveling a distance given by the mixing length before dissolving in the surroundings, while cool bubbles sink about the same distance before losing their identity. Following Cox and Giuli [384], the relation between the temperature excess and the density deficit between a bubble and its surroundings is given by

$$\Delta\rho \simeq -Q \frac{\rho}{T} \Delta T, \quad (1.55)$$

where

$$-Q = \left(\frac{\partial \ln \rho}{\partial \ln \mu} \right)_{P,T} \left(\frac{\partial \ln \mu}{\partial \ln T} \right)_P + \left(\frac{\partial \ln \rho}{\partial \ln T} \right)_{\mu,P}, \quad (1.56)$$

which reduces to

$$Q = - \left(\frac{\partial \ln \rho}{\partial \ln T} \right)_{\mu,P} \quad (1.57)$$

in chemically homogeneous regions. Due to the density contrast, a buoyancy force per unit volume acts on any rising bubble, $f_b = -g\Delta\rho$. The velocity of this moving element can be estimated from the corresponding equation of motion

$$\frac{d^2r}{dt^2} = -g \frac{\Delta\rho}{\rho}. \quad (1.58)$$

Assuming that the initial velocity of the bubble at r is zero, and the density contrast increases linearly with r , from r to $r + \Delta r$, the work done by the buoyancy force per unit volume acting on the bubble along a distance Δr is given by

$$W(\Delta r) = \int_o^{\Delta r} f_b(r) dr = -\frac{1}{2} g \Delta\rho \cdot \Delta r \quad (1.59)$$

Accordingly, the average work done along a distance equal to the mixing length is given by

$$\overline{W} = \frac{1}{4} W(l_m) = -\frac{1}{8} g \Delta\rho l_m, \quad (1.60)$$

where the factor 1/4 is adopted in order to match Böhm-Vitense's work [214]. Assuming that one half of the average work translates into kinetic energy of the rising bubble, one gets

$$\frac{1}{2} \overline{W} = \frac{1}{2} \rho v^2 = \frac{1}{2} \rho \cdot \bar{v}^2 \quad (1.61)$$

And, since $v = 0$ at r ,

$$\bar{v}^2 = -\frac{1}{8} g \frac{\Delta\rho}{\rho} l_m = \frac{1}{8} g Q \frac{\Delta T}{T} l_m. \quad (1.62)$$

The temperature excess, ΔT , is often expressed in terms of the *pressure scale height*, H_P ,

$$H_P \equiv -\frac{dr}{d \ln P} = -P \frac{dr}{dP}, \quad (1.63)$$

a measure of the characteristic length of the radial variation of P , which under hydrostatic equilibrium conditions is simply given by

$$H_P = \frac{P}{\rho g}. \quad (1.64)$$

All in all, the temperature excess can be written as

$$\Delta T = T \frac{l_m}{H_P} (\nabla - \nabla'), \quad (1.65)$$

with $\nabla \equiv d \ln T / d \ln P$ being the average temperature gradient with respect to pressure of all the matter at a given location r , and $\nabla' \equiv d \ln T' / d \ln P$ the gradient of the rising (sinking) bubble, often approximated as [384, 1037]

$$\nabla' = \nabla_{\text{ad}}. \quad (1.66)$$

Equations 1.62, 1.65, and 1.66 yield the expression for the (local) convective velocity,

$$\bar{v} = \frac{1}{2^{3/2}} \frac{l_m}{r} \left[-\frac{Gm}{H_P} (\nabla - \nabla_{\text{ad}}) \left(\frac{\partial \ln \rho}{\partial \ln T} \right)_{P,\mu} \right]^{1/2}. \quad (1.67)$$

The convective energy flux can be obtained from the product of the thermal energy per gram carried by the rising bubble (which moves at constant pressure), $C_p \Delta T$, and the mass flux, $\frac{1}{2} \rho \bar{v}$. The factor 1/2 results from the assumption that upward and downward flows are identical, and, therefore, only one half of the matter moves upwards at any time:

$$F_{\text{conv}} = \frac{1}{2} \rho \bar{v} C_p \Delta T. \quad (1.68)$$

Finally, plugging Equations 1.65 and 1.67 into Equation 1.68, and recalling that $L = 4\pi r^2 F$, one gets an expression for the (local) convective luminosity:

$$L_{\text{conv}} = \pi \sqrt{-\frac{G}{2} \left(\frac{\partial \ln \rho}{\partial \ln T} \right)} H_P^{-3/2} l_m^2 C_p \frac{r T m^{1/2}}{V} (\nabla - \nabla_{\text{ad}})^{3/2}. \quad (1.69)$$

Equation 1.69, which appears explicitly in the energy transport equation whenever superadiabatic temperature gradients are established within the stellar plasma, depends on the mixing-length, l_m , which is taken as a free parameter. Different prescriptions are adopted for l_m on the basis of plausibility arguments. Frequently, l_m is taken as a multiple of the pressure scale height, in the form

$$l_m = \alpha H_P, \quad (1.70)$$

with adopted values for α in the range 1–3. There are reasons to favor $l_m \sim H_P$ (that is, $\alpha \sim 1$) [384]: On one hand, convective cells much smaller than one scale height in size would not efficiently carry energy away, first because of their small size (radiative energy losses will be important), and second because of the small distance travelled before dissolving. Therefore, only large convective bubbles play a relevant role in convective energy transport. On the other hand, convective elements cannot retain their identities when traveling through distances larger than a few scale heights. Empirical determinations of α around ~ 1.7 – 1.9 have been inferred by fitting stellar evolution models to the observed properties of the Sun [1181]. However, it is unclear how to extrapolate this value of α to other types of stars, particularly under explosive conditions¹³.

¹³Another limitation of the mixing-length theory is its inability to account for convective overshoot, that is, the displacement of fluid elements beyond the boundaries of the convective regions. In sharp contrast to mixing-length formulation, it is expected that convective mixing would not stop abruptly at the edge of a convective region. Indeed, evidence of convective overshoot has been observed in the Sun in the form of granulation at the surface.

It is finally worth noting that many phases of the evolution of stars are characterized by steady conditions, and, therefore, by large timescales. In such conditions, it is justified to assume a time-independent prescription for convective transport. However, when a star proceeds in a nearly dynamical timescale (i.e., during explosive stages or collapses; see Section 1.3.1), the assumption of a time-independent convection does not hold, and one should rely on a time-dependent formalism (see, e.g., reference [1955]).

1.3 A Touch of Hydrodynamics

1.3.1 Timescales

Some characteristic timescales have proved particularly useful in unveiling the physical mechanisms that drive stellar explosions and the conditions in which these take place. In this section, a number of relevant timescales employed within this book are reviewed.

The equation of momentum conservation (Equation 1.28) establishes that if the pressure gradient imbalances the gravitational force, an acceleration results. Let's assume, for convenience, that the pressure term just vanishes. Equation 1.28 then becomes

$$\frac{\partial u}{\partial t} = -G \frac{m}{r^2}, \quad (1.71)$$

or, in terms of the surface gravity, g ,

$$\frac{\partial^2 r}{\partial t^2} = g. \quad (1.72)$$

The resulting equation merely describes the unavoidable free-fall collapse of the star, which would take place with a characteristic timescale τ_{ff} that can be inferred by setting $\partial^2 r / \partial t^2 \sim R / \tau_{\text{ff}}^2$, with R being the radius of the star. All in all, we get

$$\frac{R}{\tau_{\text{ff}}^2} \sim g \rightarrow \tau_{\text{ff}} \sim \sqrt{\frac{R}{g}}, \quad (1.73)$$

which in terms of the average density of the star, $\bar{\rho} = 3M/4\pi R^3$, becomes

$$\tau_{\text{ff}} \sim \frac{1}{\sqrt{G\bar{\rho}}}. \quad (1.74)$$

Similar dynamical timescales, within factors of the order of unity, can be derived¹⁴. For instance, the free-fall (or escape velocity) in a gravitational field, $v_{\text{esc}} = \sqrt{2GM/R}$, yields

$$\tau_{\text{dyn}} \sim \frac{R}{v_{\text{esc}}} = \sqrt{\frac{R^3}{2GM}} \sim \frac{1}{\sqrt{G\bar{\rho}}}. \quad (1.75)$$

¹⁴Another frequently used estimate for τ_{ff} can be obtained by considering a spherical shell initially at a distance r_0 from the center of a star. The free-fall speed of a point in the shell during collapse, for an arbitrary distance to the center, r , can be inferred from energy conservation:

$$\frac{1}{2}u^2 = \frac{1}{2} \left(\frac{dr}{dt} \right)^2 = \left(-\frac{Gm(r_0)}{r_0} \right) - \left(-\frac{Gm(r_0)}{r} \right).$$

Defining $\tau_{\text{ff}} \equiv \int_0^{r_0} (1/u) dr$, and replacing u by a suitable expression from the energy conservation equation, one gets

$$\tau_{\text{ff}} = \sqrt{\frac{3\pi}{32\bar{\rho}G}}.$$

Note that such dynamical timescales provide an estimate of the time required by a star to recover hydrostatic equilibrium before a collapse or an explosion results. For a star like the Sun, $\tau_{\text{dyn}} \sim 1000$ s.

A crude estimate of the characteristic timescale for a stellar explosion can actually be inferred by, instead, setting the gravitational force to zero in the momentum conservation equation (Equation 1.28):

$$\frac{\partial^2 r}{\partial t^2} = -4\pi r^2 \left(\frac{\partial P}{\partial m} \right) = \frac{1}{\bar{\rho}} \left(\frac{\partial P}{\partial r} \right). \quad (1.76)$$

Imposing, as before, $\partial^2 r / \partial t^2 \sim R / \tau_{\text{expl}}^2$ and $\partial P / \partial r \sim \bar{P} / R$, one gets

$$\frac{R}{\tau_{\text{expl}}^2} \sim \frac{1}{\bar{\rho}} \frac{\bar{P}}{R} \rightarrow \tau_{\text{expl}} \sim R \sqrt{\frac{\bar{\rho}}{\bar{P}}}, \quad (1.77)$$

where \bar{P} and $\bar{\rho}$ are averaged over the whole star. Since the speed of sound of a wave propagating through an elastic medium is given by

$$c_s = \sqrt{\left(\frac{\partial P}{\partial \rho} \right)}, \quad (1.78)$$

τ_{expl} is of the order of R/c_s , which implies that the time required by an explosion to propagate from the center to the surface of a star is of the order of the sound-crossing time.

A suitable definition for the nuclear timescale is given by

$$\tau_{\text{nuc}} \sim \frac{c_p T}{\varepsilon}, \quad (1.79)$$

where c_p is the specific heat and ε the nuclear energy generation rate.

The relevance of convective transport, particularly for mixing of chemical species, can be evaluated by means of the convective turnover time, or ratio of the size of the convective region, l_{conv} , over the characteristic velocity of the rising blobs, v_{conv} (see Section 1.2.4.3):

$$\tau_{\text{conv}} \sim \frac{l_{\text{conv}}}{v_{\text{conv}}}. \quad (1.80)$$

Another useful timescale, particularly for accretion-driven stellar explosions, is the accretion timescale, defined in terms of the mass-accretion rate, \dot{M} , and the overall accreted mass, ΔM_{acc} :

$$\tau_{\text{acc}} \sim \frac{\Delta M_{\text{acc}}}{\dot{M}}. \quad (1.81)$$

Usually, mass-accretion is relevant whenever $\tau_{\text{acc}} \leq \tau_{\text{nuc}}$.

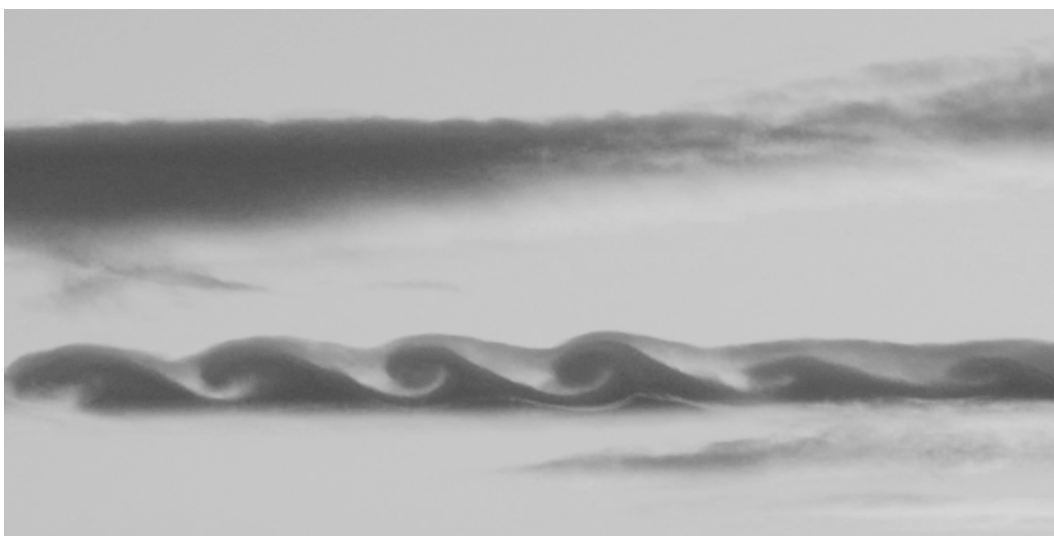
1.3.2 Instabilities

The astrophysical plasmas encountered in the study of stellar explosions frequently undergo shocks, turbulence, chaos, and a number of phenomena that drive the formation of a suite of different instabilities.

Mixing at the core-envelope interface during classical nova outbursts is likely driven by the onset of Kelvin–Helmholtz instabilities (see Chapter 4). Named after Lord Kelvin and Hermann von Helmholtz, these instabilities are driven by velocity differences across the interface between two fluids (or by a velocity shear in a single fluid). Kelvin–Helmholtz



(a)



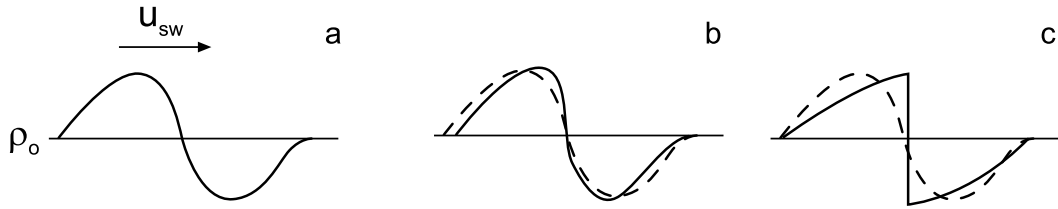
(b)

FIGURE 1.7

Characteristic Kelvin–Helmholtz instabilities in stormy clouds spotted at (a) the Birmingham–Shuttlesworth International Airport (USA) in December 2011, and (b) around Sagunt (Valencia, Spain). Color versions of these images are available at <http://fisica.upc.edu/ca/users/jjose/CRC-Downloads>. Credits: (a) WBMA-TV, Birmingham (Alabama, USA) and (b) Minerva Gracia; reproduced with permission.

instabilities develop into characteristic ripples that are often seen in terrestrial fluids, such as clouds (see Figure 1.7) or ocean/sea waves, and have even been spotted in Saturn's atmosphere and in the solar corona.

In sharp contrast, Rayleigh–Taylor instabilities require density gradients. Named after

**FIGURE 1.8**

Formation of a discontinuity in a pressure wave propagating through a uniform fluid.

Lord Rayleigh and Geoffrey I. Taylor, these instabilities appear in every fluid, or at the interface between two fluids, characterized by a density inversion, in particular when a lighter fluid pushes the heavier one. Therefore, the driving mechanism for Rayleigh–Taylor instabilities is buoyancy, not shear (unlike Kelvin–Helmholtz instabilities). The characteristic fingering accompanying Rayleigh–Taylor instabilities has been observed in terrestrial plasmas (e.g., in plasma fusion reactors; see also Section 1.7.2). They are also present in astrophysical plasmas, like in the Crab nebula, a famous supernova remnant (see Chapters 5 and 7), when accelerated gas from the innermost regions collides with a denser gas shell. Strong Rayleigh–Taylor instabilities have also been discussed in the context of SN 1987A [69, 1269] (see Chapter 7). Magnetically modulated Rayleigh–Taylor instabilities have also been spotted in the solar corona, in the form of upflow plumes, when a relatively dense solar prominence overlies a lower density plasma bubble [158].

A variation of Rayleigh–Taylor instabilities, known as Richtmyer–Meshkov instabilities, occur when a shock wave impinges perpendicularly upon an interface that separates two fluids with different densities [251, 1230, 1499]. Richtmyer–Meshkov instabilities develop, for instance, during implosion in inertial confinement fusion experiments and have been linked to the initiation of the deflagration to detonation transition in type Ia supernova models [1351, 1785] (see Chapter 5). The interested reader can find a detailed overview on fluid instabilities in Shore [1634].

1.3.3 Shock Waves and the Physics of Combustion

The nonlinear nature of the Navier–Stokes equations of fluid dynamics gives rise to a number of peculiar patterns, in the form of contact discontinuities, shock fronts, and rarefaction waves. See Section 1.7.1.1 for an example of a hydrodynamic problem in which these three types of discontinuities are actually encountered.

Discontinuities arise, for instance, when a large-amplitude pressure wave propagates through a uniform fluid [224]. Two distinct regions can be identified in the pressure pulse: A compression region, characterized by $\rho > \rho_0$, and a rarefaction region, where $\rho < \rho_0$ (with ρ_0 being the density of the unperturbed fluid; see Figure 1.8). As the pulse moves forward, and because the speed of sound increases as the density increases, the compression region begins to move faster than the rarefaction region. Eventually, a discontinuity develops¹⁵. Special numerical techniques must be implemented to handle such discontinuities, since they cannot be adequately represented by a grid.

Contact discontinuities are surfaces that separate regions of different density and temperature, while maintaining pressure constant on both sides. Let's consider the velocity

¹⁵A similar outcome is expected for a pulse that propagates outward across a star, through layers of decreasing density. Note that if the maximum pressure is not much larger than that of the unperturbed fluid, the wave will move at approximately the speed of sound.

vector describing a fluid flow, $\vec{u} = (u_n, u_t)$, where u_n and u_t represent the normal and tangential components of \vec{u} , with respect to the surface of the discontinuity. When u_t also varies substantially across the discontinuity, this is referred to as a slip discontinuity. In contrast, both shocks and rarefaction waves result from abrupt changes in pressure, with shock fronts associated to compression episodes and rarefaction waves accompanying fluid expansions. Shock fronts, in particular, separate regions characterized by different pressure, density, temperature, and velocity (normal component), which may vary abruptly across the discontinuity. Shock fronts frequently occur, for instance, in the context of stellar explosions.

While small-amplitude perturbations propagate throughout a fluid adiabatically, at the local speed of sound, c_s , strong perturbations can propagate supersonically. Here, a discontinuity between the regions behind and ahead of the disturbance will develop. Both regions would become locally disconnected. Indeed, the yet unperturbed fluid would not be able to react to the imminent arrival of the supersonic shock (through expansion, for instance), since such information is propagated at the speed of sound.

Let's assume that a strong shock wave, propagating at a supersonic speed u_{sw} , separates two regions of a fluid. The undisturbed region ahead of the shock wave, initially at rest ($u'_1 = 0$), is characterized by a pressure P_1 , density ρ_1 , and temperature T_1 . The postshocked region moves at speed u'_2 , with a pressure, density, and temperature given by P_2 , ρ_2 , and T_2 . In the reference frame comoving with the shock wave at speed u_{sw} (see Figure 1.9), the undisturbed fluid flows toward the discontinuity at speed $u_1 = u_{sw}$, while the postshocked fluid left behind moves at speed $u_2 = u_{sw} - u'_2$. Note that the speed of the shock front¹⁶ must fulfill $u_{sw} > c_s$, otherwise the discontinuity would smoothen and eventually disappear.

The relation between the physical variables in the unperturbed and postshocked regions of the fluid across a planar shock wave (i.e., a shock perpendicular to the flow) is given by the following set of conservation equations, known as *Rankine–Hugoniot, junction, or jump conditions* [854, 855, 1468]:

- Mass flux conservation

$$\rho_1 u_1 = \rho_2 u_2 \quad (1.82)$$

- Energy flux conservation

$$u_1 \left(\frac{1}{2} \rho_1 u_1^2 + E_1 \rho_1 + P_1 \right) = u_2 \left(\frac{1}{2} \rho_2 u_2^2 + E_2 \rho_2 + P_2 \right), \quad (1.83)$$

where E is the internal energy per unit mass.

- Momentum flux conservation

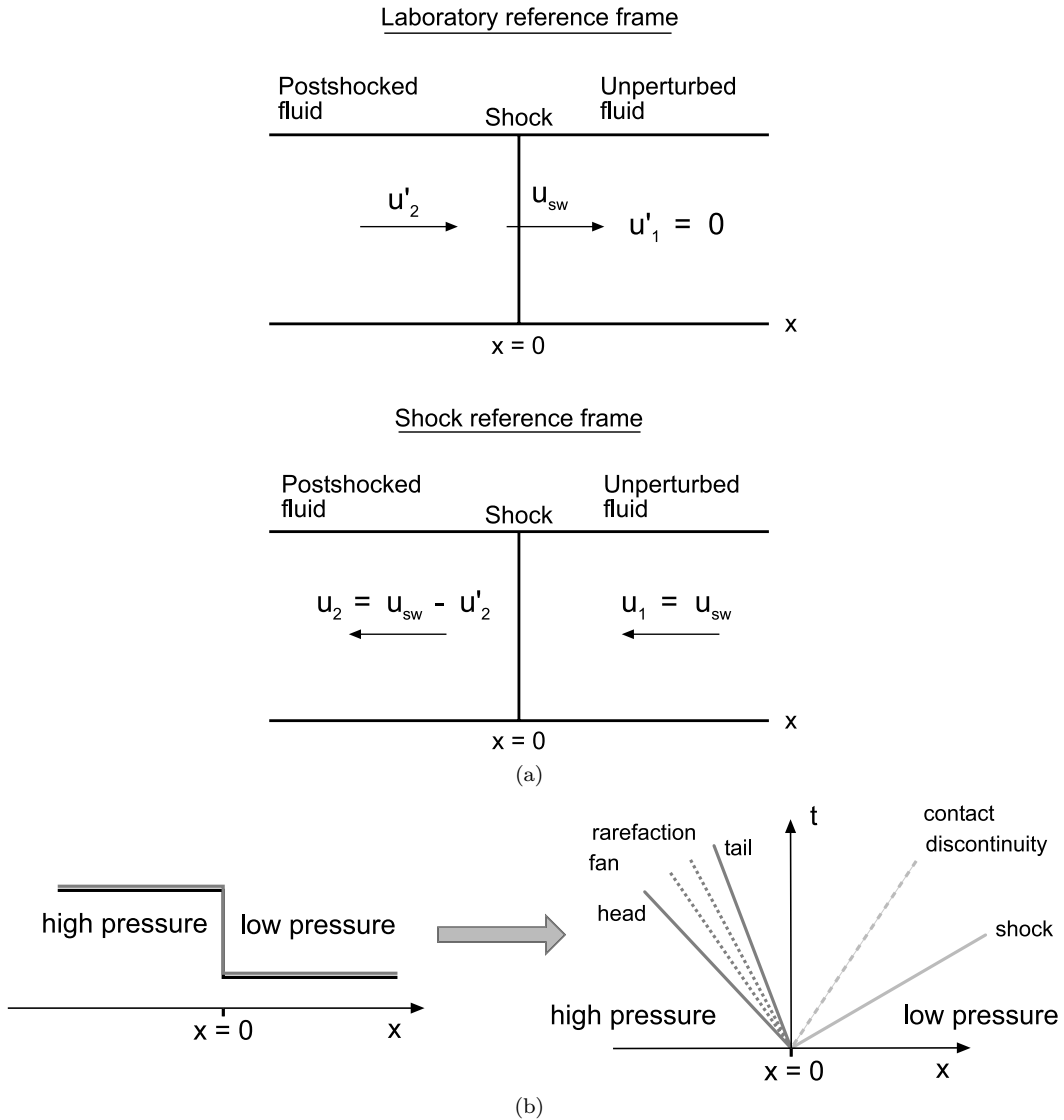
$$P_1 + \rho_1 u_1^2 = P_2 + \rho_2 u_2^2 \quad (1.84)$$

1.3.3.1 Deflagrations vs. Detonations

The passage of a shock wave may raise the temperature of the plasma to ignition values. The associated combustion front can propagate either subsonically (deflagration) or supersonically (detonation).

In a detonation, combustion proceeds on a timescale shorter than the characteristic hydrodynamic timescale. The corresponding burning front propagates simultaneously but slightly behind the shock (since the material needs first to be heated up to the characteristic burning temperature), incinerating the material lying right behind the shock front. Both

¹⁶It is also worth noting that the fluid dissipates part of its kinetic energy into heat upon crossing the shock. Therefore, an entropy jump is also encountered across the shock.

**FIGURE 1.9**

(Top) The passage of a shock wave as seen from the laboratory and from a reference frame comoving with the shock at speed u_{sw} . (Bottom) Diagram depicting the different types of discontinuities driven by a sharp pressure jump in a shock tube (see Section 1.7.1.1). A color version of this picture is available at <http://fisica.upc.edu/ca/users/jjose/CRC-Downloads>.

the detonation and the combustion fronts propagate at the same supersonic speed with respect to the unperturbed fluid.

A deflagration, instead, propagates by means of heat (and mass) exchange between preshocked and postshocked material. Here, the shock wave itself is unable to initiate the incineration of the plasma, and therefore both the (subsonic) burning front and the shock front propagate independently.

The evolution of a fluid from an initial state 1 to a postincineration state 2 is determined by a number of characteristic curves [1105, 1940] and is schematically shown on a $P - V$ plane in Figure 1.10(a). Let's define $J \equiv \rho_1 u_1 = \rho_2 u_2$ as the constant mass flux across the shock. Plugging this expression into the momentum flux conservation equation (Equation 1.84) yields

$$P_1 + Ju_1 = P_2 + Ju_2, \quad (1.85)$$

which, after rearranging terms, can be written as:

$$J^2 = \frac{P_2 - P_1}{u_1 - u_2}. \quad (1.86)$$

The energy flux conservation equation can be rewritten in the form

$$u_1 \left(\frac{1}{2} u_1^2 \rho_1 + H_1 \rho_1 \right) = u_2 \left(\frac{1}{2} u_2^2 \rho_2 + H_2 \rho_2 \right), \quad (1.87)$$

where H is the enthalpy of the fluid per unit mass ($H = E + PV$), and $V = 1/\rho$ the specific volume. It follows that

$$H_1 - H_2 = \frac{1}{2}(P_1 - P_2)(V_1 + V_2). \quad (1.88)$$

Equation 1.88 defines the *Hugoniot curve* or *shock adiabat*.

The combination of mass and momentum flux equations, in turn, yields

$$P_1 + \frac{J^2}{\rho_1} = P_2 + \frac{J^2}{\rho_2}. \quad (1.89)$$

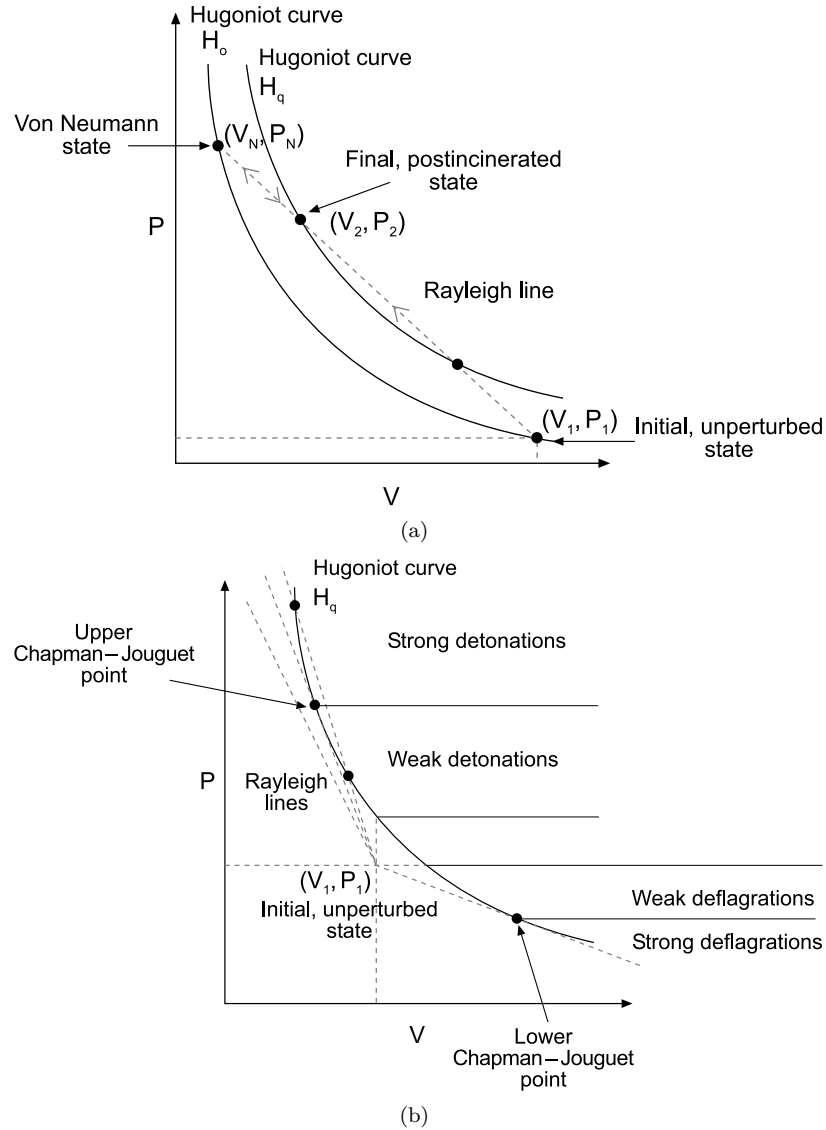
Note that, in terms of the specific volume, V , this corresponds to a straight line on the $P - V$ plane, $P + J^2 V$, known as the *Rayleigh line*. Equation 1.89 can be conveniently rewritten as

$$P_2 = P_1 + u_1^2 \left[\rho_1 - \frac{\rho_1^2}{\rho_2} \right] \equiv \alpha + \beta u_1^2 V_2, \quad (1.90)$$

which shows that the slope of the Rayleigh line is proportional to the square of the detonation velocity, u_1 . Therefore, one can think of a series of Rayleigh lines resulting for different values of u_1 . In the simplest theory of combustion developed by D. L. Chapman and J. C. E. Jouguet [313, 934, 935], the final state of the postshocked fluid (that is, the solution to the flux conservation equations) is determined by the intersection between the Rayleigh line and the Hugoniot curve (see reference [522] for details).

The upper left branch of the Hugoniot curve in Figure 1.10(b) identifies the possible postshocked states of the fluid after the passage of a detonation front, which precompresses the fluid prior to incineration. On a $P - V$ diagram, this corresponds to a trajectory given by the Rayleigh line from the initial (V_1, P_1) state up to the so-called Von Neumann state¹⁷ (V_N, P_N) on the shock adiabat H_o (or Hugoniot curve corresponding to zero energy released by nuclear reactions, as calculated by Equation 1.88). The Hugoniot curve shifts, however,

¹⁷The Von Neumann state corresponds to the high-pressure point on the unreacted Hugoniot curve, H_o , reached after compression of the fluid from the initial, unperturbed state along the Rayleigh line (see Figure 1.10).

**FIGURE 1.10**

(Top) The loci of all possible final states of a fluid after the passage of a combustion front. (Bottom) Final states reached through weak/strong deflagrations and detonations. Color versions of these plots are available at <http://fisica.upc.edu/ca/users/jjose/CRC-Downloads>.

toward the upper right corner of the $P - V$ diagram as nuclear fusion sets in. The final curve, H_q , corresponding to complete incineration, is determined by the addition of the nuclear energy released per unit mass, q_{nuc} , to the overall energy flux conservation Equation 1.84. As incineration goes to completion, the fluid moves from (V_N, P_N) down the Rayleigh line up to a point (V_2, P_2) on the Hugoniot curve H_q .

Depending on the specific value of u_1 , the Rayleigh line may actually intersect the Hugoniot curve at two distinct locations, may be tangent to the Hugoniot curve, or may not intersect at all (the latter corresponding to an unphysical case that does not satisfy the whole set of conservation equations). The single intersection point obtained when the Rayleigh line is tangent to the Hugoniot curve is known as the (upper) Chapman–Jouguet point, CJ (see Figure 1.10). This CJ point corresponds to a minimum of the detonation velocity, and splits the upper Hugoniot curve into regions of strong (I) and weak detonations (II). Chapman–Jouguet detonations (corresponding to the tangential solution) are characterized by postincinerated products flowing at the speed of sound relative to the shock front. In contrast, the flow moves supersonically in the case of weak detonations, and subsonically for strong detonations. This means that Chapman–Jouguet and weak detonations are self-sustained, since any pressure wave generated in the incinerated products cannot catch up with the detonation front and attenuate it. Strong detonations, being potentially hampered by rarefaction waves, are not self-propagating and require the support of a moving piston¹⁸ (see, for instance, reference [522]).

With regard to the lower right branch of the Hugoniot curve (Figure 1.10), it corresponds to deflagration fronts. Here, the fluid evolves from the initial state (V_1, P_1) directly onto a point on the Hugoniot curve H_q through a Rayleigh line. As in the detonation case, the Rayleigh line that intersects the Hugoniot curve in just one point, the lower Chapman–Jouguet point, separates the regions of weak (III) and strong deflagrations (IV). The lower CJ point represents in this case a maximum of the deflagration velocity, and as in the previous detonation case, corresponds to postincinerated material propagating at the speed of sound, in the reference frame of the combustion wave. Note that while the postincinerated material is characterized by subsonic speeds in the weak deflagration region, strong (supersonic) deflagrations actually correspond to unphysical solutions.

The interested reader can find more information on the physics of shock waves in the reference text books by Landau and Lifshitz [1048] and Zeldovich and Raizer [2018]. See also Bowers and Deeming [224], Shore [1634], Bodenheimer et al. [209], or Longair [1145] for thorough descriptions of shocks and supersonic flows in astrophysical environments.

1.4 Grid-Based Methods: The Realm of Finite Differences

Most of the numerical codes used in astrophysical hydrodynamics are based on finite difference approximations to the set of partial differential equations. Such schemes, as discussed in Section 1.1, rely on a computational grid or mesh¹⁹. The simplest hydrodynamic codes

¹⁸Even though three possible detonation states have been identified in the previous analysis, one must carefully take into account the structure of the detonation front to determine whether such states are actually feasible. Indeed, Y. B. Zeldovich [2019], J. von Neumann [1868], and W. Döring [459] independently came up in the 1940s with a simple model for the structure of the detonation (known as ZND theory), in which the leading front is a shock wave that travels at the CJ velocity through the undisturbed fluid. Thus, in the framework of the ZND theory, weak detonations cannot occur. However, Fickett and Davis [522] proved that weak detonations may result if some of the restrictions imposed by the ZND theory are relaxed. It is finally worth noting that weak detonations do actually occur but are very seldom observed.

¹⁹Meshfree codes, such as SPH, are discussed in Section 1.5.

assume spherical symmetry (1D) and are frequently implemented in Lagrangian formulation. This, unfortunately, is not always feasible in 2D and 3D, since Lagrangian meshes often suffer severe distortion and tangling in the presence of nonlinear phenomena, discontinuities, or singularities. Therefore, while the vast majority of 1D codes rely on Lagrangian grids, multidimensional codes are frequently Eulerian.

This section focuses on the main features of 1D, Lagrangian hydrodynamic codes²⁰. They rely on the following set of coupled mechanical and thermal equations that describe the structure and time evolution of a star (see Section 1.2):

- Conservation of mass

$$V = \frac{4}{3}\pi \frac{\partial r^3}{\partial m}. \quad (1.91)$$

- Conservation of momentum

$$\frac{\partial u}{\partial t} + 4\pi r^2 \frac{\partial(P + q)}{\partial m} = -G \frac{m}{r^2}, \quad (1.92)$$

where q is an artificial viscosity²¹ term.

- Conservation of energy

$$\frac{\partial E}{\partial t} = \varepsilon - \frac{\partial L}{\partial m} - (P + q) \frac{\partial V}{\partial t}, \quad (1.93)$$

where ε is the overall energy generation rate by nuclear reactions and energy losses by neutrinos ($\varepsilon = \varepsilon_{nuc} - \varepsilon_\nu$).

- Energy transport (by radiation and convection)

$$L = -256\sigma\pi^2 r^4 \frac{T^3}{3\kappa} \frac{\partial T}{\partial m} + L_{\text{conv}}, \quad (1.94)$$

where L_{conv} the convective luminosity (Section 1.2.4.3).

- Lagrangian velocity

$$\frac{\partial r}{\partial t} = u. \quad (1.95)$$

The set of partial differential equations is linked to the constitutive equations:

- Pressure and internal energy: $P = P(T, \rho, X)$, $E = E(T, \rho, X)$
- Opacity: $\kappa = \kappa(T, \rho, X)$
- Nuclear energy generation and neutrino losses: $\varepsilon = \varepsilon(T, \rho, X)$,

where X represents the mass fractions of the chemical species present in the stellar plasma (see Chapter 2).

²⁰For convenience, we will mostly rely on the choices adopted in building up the 1D, Lagrangian, implicit, hydrodynamic code SHIVA [919], extensively used in the modeling of classical nova explosions and type I X-ray bursts.

²¹The first hydrodynamic simulations of thermonuclear explosions (e.g., the implosion bomb model developed in 1943–1994) failed in the presence of shocks. Shock waves are modeled as discontinuities that are difficult to handle numerically unless certain tricks are implemented. One such trick relies on the inclusion of an unphysical term, known as artificial viscosity, to smear out discontinuities, thickening the narrow shock transition zones (which extend over a few mean-free paths) to widths that could be resolved computationally. Pioneering work on the use of artificial viscosity was performed by R. D. Richtmyer in 1948 (even if the author never used that term but the words *fictitious* or *mock* to describe the concept), remaining classified until 1993. His first report, LA-671, is actually available at <http://fas.org/sgp/othergov/doe/lanl/index1.html>. A paper on this subject, coauthored by von Neumann and Richtmyer, was published in 1950 [1870].

1.4.1 Equations of Stellar Structure in Finite Differences

Solutions to the system of partial differential equations, Equations 1.92–1.95, are obtained for a finite, discrete number of grid points that define the computational domain. To this end, the domain is subdivided into N individual cells (also called elements or shells). In a 1D framework, this corresponds to segments that define N concentric shells and the corresponding $N + 1$ intershells. Hereafter, each intershell will be labeled with a subscript i , ranging from 1 (at the star's center or innermost shell) to $N + 1$ (stellar surface).

The goal of any stellar hydrocode is to determine the time evolution of a set of physical variables (e.g., luminosity, L ; radius, r ; velocity, u ; temperature, T ; and specific volume, V) at each shell. Such variables must be assigned to specific grid points, frequently involving cell-centered locations or cell edges. The choice, however, is somewhat arbitrary and certainly not unique, as a thorough comparison between existing codes would prove. A convenient choice in 1D assigns variables L , r , and u to each of the $N + 1$ intershells, while V and T are regarded as shell-centered variables (i.e., assigned to a mass-coordinate given by the geometric mean $m_{i+1/2} = \sqrt{m_{i+1} m_i}$). Note that in a Lagrangian formulation, the most convenient independent variables are the mass interior to the i^{th} -intershell, m_i , and time, t^n .

In this chapter, a superscript will be used to indicate whether a given variable is evaluated at current time, t^{n+1} , or at previous time, t^n . Accordingly, note that the time-step is simply given by $\Delta t \equiv t^{n+1} - t^n$. Following Potter [1441], partial differential equations involving time-derivatives, in the form

$$\frac{\partial y}{\partial t} = Ly, \quad (1.96)$$

where L represents an operator, can be discretized in a general way as

$$y^{n+1} = y^n + Ly^n(1 - \beta)\Delta t + Ly^{n+1}\beta\Delta t, \quad (1.97)$$

where y^n and y^{n+1} are the values of function y at times t^n and t^{n+1} , respectively, while β is an interpolation parameter ($0 \leq \beta \leq 1$) that defines different numerical schemes. The choice $\beta = 0$ leads to an *explicit* determination of y^{n+1} from the previous, known value y^n . This condition defines the so-called *explicit* methods. Instead, the choice $\beta \neq 0$ defines *implicit* methods. In general, explicit schemes are easier to implement than implicit schemes. However, explicit schemes are only stable if the time-step is limited by the *Courant–Friedrichs–Levy condition* (see Problem P5 at the end of this chapter), that prevents any disturbance traveling at the sonic speed from traversing more than one numerical cell, thus leading to unphysical results [1500]. On the other hand, implicit schemes allow larger time-steps than explicit schemes, with no precondition on the time-step, but they require an iterative procedure to solve the system at each step. $\beta = 0.5$ is the only choice that ensures second-order accuracy in the time-derivatives, resulting in neither artificial damping nor unphysical amplification [1037, 1268].

The system of differential equations needs to be supplemented by a suitable set of boundary conditions at the edges of the computational grid. A convenient choice for a 1D, Lagrangian code (see, e.g., reference [1037]) is:

- Innermost shell: $m = m_1 \Rightarrow u = 0, L = L_1, r = r_1$. When the innermost shell corresponds to the star's center, $m_1 = 0 \Rightarrow u_1 = r_1 = L_1 = 0$.
- Surface: $m = M_{tot} \Rightarrow T^4 = \frac{3}{4}T_{\text{eff}}^4 \left(\frac{2}{3} + \tau\right), P = P_{\text{rad}}$, where τ is the optical depth, T_{eff} the effective temperature²², and P_{rad} the radiation pressure.

²²The effective temperature of a star is the temperature of a blackbody with the same luminosity of the star per surface area.

Prior to discretizing the set of differential equations into an algebraic system of equations in finite differences, one has to consider whether rescaling of certain variables is required to avoid potential numerical problems. A suitable choice, for instance, includes:

- $m_i \rightarrow Q_i = 1 - m_i/M_{\text{tot}}$
- $r_i \rightarrow R_i = \ln r_i$
- $V_{i+1/2} \rightarrow W_{i+1/2} = \ln V_{i+1/2}$
- $T_{i+1/2} \rightarrow Z_{i+1/2} = \ln T_{i+1/2}$
- $L_i \rightarrow B_i = L_i/L_\odot$,

where M_{tot} is the overall mass of the star and L_\odot is the solar luminosity.

All in all, the system of equations of stellar structure in finite difference form²³ can be written as:

- Conservation of mass

$$\frac{4\pi}{3M_{\text{tot}}} \frac{(r_i^3 - r_{i-1}^3)^{n+1}}{Q_i - Q_{i-1}} = -V_{i-1/2}^{n+1} \quad (1.98)$$

- Conservation of momentum

$$\begin{aligned} \frac{u_i^{n+1} - u_i^n}{\Delta t} &= (1 - \beta)\mathbf{F}_i^n + \beta\mathbf{F}_i^{n+1} + \frac{4\pi}{M_{\text{tot}}} \frac{1}{Q_{i+1/2} - Q_{i-1/2}} \\ &\left((1 - \beta)(r_i^2)^n \left[q_{i+1/2}^{n+1/2} \frac{V_{i+1/2}^{n+1}}{V_{i+1/2}^n} - q_{i-1/2}^{n+1/2} \frac{V_{i-1/2}^{n+1}}{V_{i-1/2}^n} \right] + \beta(r_i^2)^{n+1} (q_{i+1/2}^{n+1/2} - q_{i-1/2}^{n+1/2}) \right), \end{aligned} \quad (1.99)$$

where

$$\mathbf{F}_i^n = 4\pi \frac{(r_i^2)^n}{M_{\text{tot}}} \frac{P_{i+1/2}^n - P_{i-1/2}^n}{Q_{i+1/2} - Q_{i-1/2}} - G \frac{m_i}{(r_i^2)^n}$$

- Conservation of energy

$$\begin{aligned} \frac{E_{i-1/2}^{n+1} - E_{i-1/2}^n}{\Delta t} &= \varepsilon_{i-1/2}^n + (1 - \beta)\mathbf{G}_{i-1/2}^n + \beta\mathbf{G}_{i-1/2}^{n+1} \\ &- q_{i-1/2}^{n+1/2} V_{i-1/2}^{n+1} \frac{W_{i-1/2}^{n+1} - W_{i-1/2}^n}{\Delta t}, \end{aligned} \quad (1.100)$$

where

$$\mathbf{G}_{i-1/2}^{n+1} = \frac{L_\odot}{M_{\text{tot}}} \frac{B_i^{n+1} - B_{i-1}^{n+1}}{Q_i - Q_{i-1}} - P_{i-1/2}^{n+1} V_{i-1/2}^{n+1} \frac{W_{i-1/2}^{n+1} - W_{i-1/2}^n}{\Delta t}$$

²³Both convective energy transport and nuclear energy generation are implemented explicitly in the finite difference scheme outlined here (see also reference [1037]). Other fully implicit formulations are obviously possible.

- Energy transport (by radiation and convection²⁴⁾)

$$B_i^{n+1} = 256\sigma\pi^2(r_i^4)^{n+1} \frac{(T_i^4)^{n+1}}{3L_\odot M_{\text{tot}}\kappa_i^{n+1}} \frac{Z_{i+1/2}^{n+1} - Z_{i-1/2}^{n+1}}{Q_{i+1/2} - Q_{i-1/2}} - \mathbf{H}_i^n \frac{r_i^{n+1} T_i^{n+1}}{V_i^{n+1}}, \quad (1.101)$$

where

$$\mathbf{H}_i^n = \begin{cases} 0, & \text{if } \nabla_i^n \leq \nabla_{\text{ad},i}^n \\ \frac{\pi}{L_\odot} \sqrt{G/2} H_{p,i}^{-3/2} l_{m,i}^2 m^{1/2} c_{p,i} \sqrt{\left(\frac{\partial W}{\partial Z}\right)} (\nabla_i - \nabla_{\text{ad},i})^{3/2}, & \text{if } \nabla_i^n > \nabla_{\text{ad},i}^n \end{cases}$$

- Lagrangian velocity

$$\frac{R_i^{n+1} - R_i^n}{\Delta t} = (1 - \beta) \frac{u_i^n}{r_i^n} + \beta \frac{u_i^{n+1}}{r_i^{n+1}} \quad (1.102)$$

Special care has to be devoted to the implementation of the energy transport equation at the surface, taking into account the corresponding boundary conditions. Following Kutter and Sparks [1037], when convection is neglected between grid points $N + 1/2$ and $N + 1$, the energy transport equation becomes

$$B_{N+1}^{n+1} = 16\sigma\pi(r_{N+1}^2)^{n+1} \frac{(T_{N+1/2}^4)^{n+1}}{3L_\odot} \left[-\frac{M_{\text{tot}}}{4\pi} (Q_{N+1} - \right. \\ \left. Q_{N+1/2}) \frac{\kappa_{N+1/2}^{n+1}}{2\sqrt{(r_{N+1}^3 r_N)^{n+1}}} + \frac{2}{3} \right]^{-1}. \quad (1.103)$$

It is worth noting that an artificial viscosity term, q , has been included in the conservation of momentum (Equation 1.99) to handle shock waves. Following von Neumann and Richtmyer [1870], q can be expressed as the divergence of the velocity, which ensures that artificial viscosity remains negligible in the absence of shocks. A simple procedure switches on artificial viscosity whenever any mass-shell gets compressed (i.e., $\rho_{i+1/2}^{n+1} > \rho_{i+1/2}^n$):

$$q_{i+1/2}^{n+1/2} = \begin{cases} 0, & \text{if } \rho_{i+1/2}^{n+1} \leq \rho_{i+1/2}^n \\ q_o \frac{(r_{i+1}^{n+1} - r_i^{n+1})^2 (W_{i+1/2}^{n+1} - W_{i+1/2}^n)^2}{V_{i+1/2}^{n+1} (\Delta t^{n+1/2})^2}, & \text{if } \rho_{i+1/2}^{n+1} > \rho_{i+1/2}^n \end{cases}, \quad (1.104)$$

where q_o is a parameter of the order of unity [1037].

The algebraic system of finite difference equations in implicit formulation described above is solved through the application of an iterative procedure (a Newton–Raphson method; see Section 1.6 for a detailed account), until a given accuracy criterion is satisfied. Due to the inclusion of artificial viscosity, the overall conservation of energy²⁵ is carefully checked [332]:

$$\frac{\partial}{\partial t} \left[\frac{u^2}{2} - G \frac{m}{r} + E \right] + \frac{\partial L}{\partial m} + \frac{\partial}{\partial m} [4\pi r^2 u(P + q)] = \varepsilon_{\text{nuc}} - \varepsilon_\nu \quad \text{erg g}^{-1} \text{s}^{-1} \quad (1.105)$$

²⁴For simplicity, only the time-independent prescription for convection is given in the expression for the energy transport. Interested readers are referred to Wood [1955] for a suitable time-dependent scheme.

²⁵In most of the simulations performed with the 1D code SHIVA, energy is conserved to within a few percent.

1.4.2 Nuclear Reaction Networks

Even though the energetics of a stellar explosion can often be approximated by a handful of nuclides and nuclear processes, state-of-the-art nucleosynthesis studies require hundreds of isotopes linked through hundreds or thousands of nuclear interactions. Their implementation in a stellar evolution hydro code may cause a severe slowdown in its performance, becoming the truly time-limiting factor, to the point that nucleosynthesis calculations are often not viable without the aid of high-power supercomputers, unless postprocessing techniques are employed. Special care, therefore, has to be devoted to the numerical techniques used to handle nuclear reaction networks, in order to allow larger step-sizes in full hydrodynamical models or to increase the performance in postprocessing calculations.

The differential equations that dictate the time evolution of the abundances in a stellar plasma frequently contain terms that may lead to rapidly varying solutions. For a particular nuclide i , and in the absence of diffusion of chemical species, they can be written as:

$$\frac{dY_i}{dt} = \dot{R}_i, \quad (1.106)$$

where $Y_i = X_i/M_i$ is the mole fraction of species i , or ratio between mass-fraction abundance, X_i , and mass, M_i (see Chapter 2 for suitable definitions). \dot{R}_i is the overall reaction rate, that is, a balance of all reactions producing and destroying species i . Stiffness actually requires extremely small step-sizes to avoid potential numerical failures driven by severe instabilities, particularly in the context of explicit schemes. A number of implicit and semiimplicit techniques have been implemented over the last decades to overcome those problems. Some of these methods [73, 1826, 1873, 1969], particularly Wagoner's two-step linearization technique [1873], have become the standard in nucleosynthesis studies for nearly 40 years, and in spite of their limitations, are still widely used.

1.4.2.1 Wagoner's Method

Wagoner's two-step linearization technique [1873] is a semiimplicit, second-order Runge–Kutta method that can be viewed as an extension of the first numerical schemes employed in the study of type Ia supernova nucleosynthesis [62, 74, 1826] (see Chapter 5).

Let Y^n be the vector that contains the mole fractions of all species included in the network at time t^n (i.e., $Y_1^n, Y_2^n, \dots, Y_N^n$). In Wagoner's method, the change in mole fractions after one timestep, $t^{n+1} = t^n + \Delta t$, is estimated as

$$Y^{n+1} = Y^n + \frac{1}{2}\Delta t \left[\frac{dY}{dt}(Y^n, t^n) + \frac{dY}{dt}(\tilde{Y}^{n+1}, t^{n+1}) \right], \quad (1.107)$$

where

$$\tilde{Y}^{n+1} \equiv Y^n + \Delta t \frac{dY}{dt}(Y^n, t^n) \quad (1.108)$$

is actually determined from the Jacobian matrix $\mathbf{J} = \partial(dY^n/dt)/\partial Y$, through the equation

$$[\mathbf{I} - \Delta t \mathbf{J}] \tilde{Y}^{n+1} = Y^n, \quad (1.109)$$

where \mathbf{I} is the unity matrix. All in all, mole fractions at time t^{n+1} are determined by averaging the time-derivates of Y evaluated at times t^n and estimated for t^{n+1} .

The determination of \tilde{Y}^{n+1} is actually the most computationally challenging step in Wagoner's method. The Jacobian matrix \mathbf{J} , containing all possible forms of nuclear interaction between the N species of the network, can actually be quite large²⁶. It is, however, worth

²⁶A typical nova nucleosynthesis study is characterized by a Jacobian containing 100×100 species, about 400×400 species in the case of type Ia supernovae, and 600×600 species for X-ray bursts.

noting that nuclear interactions for a given species are mostly limited to proton, neutron, electron, or alpha captures, plus beta disintegrations (that is, involve only light particles). Indeed, reactions between heavier species are mostly prevented by the large Coulomb barriers at the temperatures of interest (exceptions include $^{12}\text{C} + ^{12}\text{C}$, or $^{12}\text{C} + ^{16}\text{O}$, for type Ia supernovae; see Chapter 2). Therefore, the matrix of interactions exhibits a characteristic sparse pattern, with large portions essentially containing zero elements, which could be efficiently handled by means of standard, optimized routines (see references [1148, 1804]).

While the best asset of Wagoner's method is its ease of implementation, it lacks a proper way to consistently infer the next time-step. Often, criteria based on the largest abundance variations from the previous step,

$$\Delta t' \sim \Delta t \left[\frac{Y^{n+1}}{Y^{n+1} - Y^n} \right]_{\min}, \quad (1.110)$$

are implemented to this end, while mass conservation within a given tolerance (i.e., $\sum_{i=1}^N X_i \equiv 1$) has to be satisfied to guarantee accuracy in the procedure.

1.4.2.2 Bader–Deuflhard's and Gear's Methods

Bader–Deuflhard's method [107] is a semiimplicit technique based on a generalization of the Bulirsch–Stoer algorithm (an application of Richardson extrapolation technique) for solving stiff systems of ordinary differential equations [1448]. The method relies on the following implicit form of the so-called midpoint rule, applied to a first-order differential equation $dY/dt = f(Y)$ (see Equation 1.106):

$$Y^{n+1} - Y^{n-1} = 2\Delta t f\left(\frac{Y^{n+1} + Y^{n-1}}{2}\right). \quad (1.111)$$

Linearization of the right-hand side of the equation about $f(Y^n)$ yields the semiimplicit midpoint rule:

$$\left[1 - \Delta t \frac{\partial f}{\partial Y}\right] Y^{n+1} = \left[1 + \Delta t \frac{\partial f}{\partial Y}\right] Y^{n-1} + 2\Delta t \left[f(Y^n) - \frac{\partial f}{\partial Y} Y^n\right]. \quad (1.112)$$

But rather than solving this equation for an arbitrary large timestep, $\Delta\tau$, Bader–Deuflhard's strategy adopts m substeps, each of length $\Delta t = \Delta\tau/m$. The method assumes that the solution corresponding to a large step $\Delta\tau$ is a function of the number of substeps, which can be proved by solving the equation for a suitable range of values of m . Once this function is found, the solution can be extrapolated to an infinite number of substeps, thus yielding converged abundances. Bader and Deuflhard inferred the values of m that provide best convergence. See references [1148, 1448, 1804] for details.

Bader–Deuflhard's technique requires that the system of equations is solved a large number of times, even if convergence is reached promptly. Therefore, the method requires large steps to offset their computational cost [1804]. In sharp contrast to Wagoner's technique, in Bader–Deuflhard's method a new timestep can be directly inferred from the extrapolation function truncation error for the desired accuracy.

Another useful method in the analysis of stiff differential equations (although much harder to implement) is Gear's backward differentiation technique [278, 619]. Gear's method relies on information available on previous steps to infer the evolution of a system. Two steps are used to determine the time evolution of the system from t^n to t^{n+1} : a predictor step and a corrector step²⁷. Aside from the possibility of directly inferring the new timestep, the main advantage of Gear's method relies on the relatively large step-sizes achievable while maintaining a moderate computational load.

²⁷The reader is referred to Longland et al. [1148] for details on the implementation of Gear's method.

The efficiency of Wagoner's, Bader–Deufhard's, and Gear's methods has been assessed through a test suite of reaction networks and postprocessing profiles from a variety of stellar nucleosynthesis sites by Richard Longland and collaborators [1148] (see also references [1804] for a detailed comparison between Wagoner's and Bader–Deufhard's schemes). According to this study, both Bader–Deufhard's and Gear's methods exhibit dramatic improvements in both speed and accuracy with respect to Wagoner's method.

1.5 Gridless Methods: Smoothed-Particle Hydrodynamics

The traditional, Lagrangian grid-based methods described in previous sections face potentially important shortcomings in 2D and 3D formulations. Indeed, the presence of shear or turbulence, for instance, may result in severe grid deformation and tangling, likely causing a computational failure. On the other hand, multidimensional Eulerian methods are harder to implement and have also a limited applicability, since they cannot handle expanding fluids properly—i.e., material may leave the computational domain. Alternative methods, specifically suited for astrophysics, have been developed to overcome the drawbacks of grid-based formulations.

This section focuses on SPH, a method that drastically eliminates grid distortions by removing the grid itself. In essence, SPH codes are closely related to *N-body methods*, where the traditional computational cells of grid-based methods are replaced by particles of a finite length. However, SPH codes need to include pressure terms to characterize stellar plasmas in most astrophysical applications²⁸. Pioneering implementations of Lagrangian SPH codes were developed by Lucy [1156] and Gingold and Monaghan [646], and were subsequently applied to a wide range of astrophysical scenarios²⁹. Those directly related with the contents of this book include type Ia supernovae [154, 245, 246, 613, 614], type II supernovae [770–772, 1278], and mergers of stellar binary systems (involving white dwarfs, neutron stars, and black holes; see Rosswog [1533] and references therein)³⁰.

1.5.1 Briefing on SPH Methods: Weighted Sums, Kernels, and Smoothing Lengths

In SPH, the physical properties of a fluid element are locally reconstructed by interpolating the properties of the neighboring particles. The *smoothed* value of a space-dependent physical variable, $f(\vec{r})$, is therefore defined as

$$\langle f(\vec{r}) \rangle = \int f(\vec{r}') W(\vec{r} - \vec{r}', h) d\vec{r}', \quad (1.113)$$

where \vec{r} is the location of particle i , $W(\vec{r}, h)$ is an interpolating (or weight) function known as *kernel*, and h is the *smoothing length*, a parameter that somehow defines the *size* of the

²⁸See, e.g., references [11, 209] for an in-depth comparison between SPH and grid-based methods.

²⁹See also references [647, 1256, 1260].

³⁰SPH has also been used in several movies that feature fluid simulations. This includes Gollum's fall into the lava, in *The Lord of the Rings: The Return of the King* (2003), and several scenes in *Superman Returns* (2006), to quote a few examples.

kernel³¹. Note that for $h \rightarrow 0$, $W(\vec{r})$ becomes a delta function [1257],

$$\lim_{h \rightarrow 0} W(\vec{r} - \vec{r}', h) = \delta(\vec{r} - \vec{r}'). \quad (1.115)$$

Two conditions are imposed to any kernel: First, it must be normalized,

$$\int W(\vec{r}, h) d\vec{r} \equiv 1, \quad \forall h \quad (1.116)$$

and second, it must correspond to an even function,

$$W(\vec{r}, h) = W(-\vec{r}, h). \quad (1.117)$$

In numerical applications, integrals are replaced by discrete summations, such that Equation 1.113 becomes

$$\langle f(\vec{r}) \rangle = \sum_j m_j \frac{f(\vec{r}_j)}{\rho(\vec{r}_j)} W(\vec{r} - \vec{r}_j, h), \quad (1.118)$$

where $m_j/\rho(\vec{r}_j)$ represents the discretized version of the volume element $d\vec{r}'$. Knowing the location and mass of the N particles of a system, one can determine the local density as

$$\langle \rho(\vec{r}) \rangle = \int \rho(\vec{r}') W(|\vec{r} - \vec{r}'|, h) d\vec{r}' = \sum_j m_j W(\vec{r} - \vec{r}_j, h). \quad (1.119)$$

The above definitions clearly stress the pivotal role played by the kernel in SPH simulations. However, the choice of the kernel is not unique, and different functions have been proposed in the literature, including the following expressions, second-order accurate in h :

- Gaussian [646]

$$W(r, h) = \frac{1}{\pi^{3/2} h^3} \exp(-w^2) \quad (1.120)$$

- Exponential [1953]

$$W(r, h) = \frac{1}{8\pi h^3} \exp(-w) \quad (1.121)$$

- Cubic spline [1261]

$$W(r, h) = \frac{1}{\pi h^3} \begin{cases} 1 - 3w^2/2 + 3w^3/4, & 0 \leq w \leq 1 \\ (2-w)^3/4, & 1 \leq w \leq 2 \\ 0, & \text{otherwise,} \end{cases} \quad (1.122)$$

³¹In this brief introduction to SPH methods, the smoothing length is considered constant, for simplicity. Certain practical situations, however, require a variable smoothing length to guarantee, for instance, a relatively constant number of neighbors throughout the computation. To this end, Hernquist and Katz [789] have proposed the simple prescription,

$$h_i^{t+\Delta t} = \frac{h_i^t}{2} \left[1 + (2^\eta - 1) \frac{n_n^0}{n_n^t} \right]^{1/\eta}, \quad (1.114)$$

where h_i^t and $h_i^{t+\Delta t}$ are the values of the smoothing length for particle i evaluated at times t and $t + \Delta t$, n_n^0 and n_n^t are the desired and actual number of neighbors for particle i , and η a parameter that controls the speed of the adjustments required to achieve $n_n^t \simeq n_n^0$. See also Price and Monaghan [1454] for another formalism based on the inclusion of a correction term to the gravitational force related to the gradient of the smoothing length.

where $w \equiv r/h$ and $r \equiv |\vec{r} - \vec{r}_j|$.

The cubic spline kernel has an important advantage with respect to other formalisms: It is defined on a *compact support*, that is, it has nonzero values only within a limited domain. This limits the number of neighbors that effectively interact with a given particle, thus reducing the computational load³². A more general cubic spline kernel, of the form

$$W(r, h) = \frac{M}{\pi h^3} \begin{cases} 1 + aw + bw^2 + cw^3, & 0 \leq w \leq 1 \\ d(2-w)^3, & 1 \leq w \leq 2 \\ 0, & \text{otherwise,} \end{cases} \quad (1.123)$$

has been introduced by Domingo García-Senz and collaborators [613]. Note that the choice $M = 1$, $a = 0$, $b = -3/2$, $c = 3/4$, and $d = 1/4$ reproduces Monaghan and Lattanzio's cubic spline kernel.

A similar procedure can be applied to calculate derivatives of an arbitrary function:

$$\begin{aligned} \langle \nabla_r f(\vec{r}) \rangle &= \sum_j \nabla_r \left(\frac{m_j}{\rho(\vec{r}_j)} f(\vec{r}_j) \right) W(\vec{r} - \vec{r}_j, h) + \frac{m_j}{\rho(\vec{r}_j)} f(\vec{r}_j) \nabla_r W(\vec{r} - \vec{r}_j, h) = \\ &\sum_j \frac{m_j}{\rho(\vec{r}_j)} f(\vec{r}_j) \nabla_r W(\vec{r} - \vec{r}_j, h), \end{aligned} \quad (1.124)$$

1.5.2 SPH Equations

SPH relies on the same set of conservation equations described for grid-based methods. Following, e.g., Hernquist and Katz [789] and Benz [153], to which the reader is referred for details, the SPH version of the main conservation equations describing an astrophysical plasma can be written as:

- Mass conservation

$$\langle \rho_i \rangle = \sum_j m_j W(\vec{r}_i - \vec{r}_j, h), \quad (1.125)$$

where ρ_i is the density of particle i (i.e., $\rho(\vec{r}_i)$).

- Energy conservation

$$\frac{dE_i}{dt} = \frac{P_i}{\rho_i^2} \sum_j m_j (\vec{u}_i - \vec{u}_j) \nabla_i W(|\vec{r}_i - \vec{r}_j|, h) + \frac{1}{2} \sum_j m_j \prod_{ij} (\vec{u}_i - \vec{u}_j) \nabla_i W(|\vec{r}_i - \vec{r}_j|, h), \quad (1.126)$$

where E_i , u_i , and P_i are the internal energy, the velocity, and the pressure of particle i , and ∇W is the derivative of the kernel. The term \prod_{ij} corresponds to the artificial viscosity (see Section 1.4), needed to handle shocks properly, and for which several prescriptions have been proposed. A widely used recipe is the one advised by Gingold and Monaghan [647], which relies on a local estimate of the divergence of the velocity:

$$\mu_{ij} = \frac{h(\vec{u}_i - \vec{u}_j)(\vec{r}_i - \vec{r}_j)}{|\vec{r}_i - \vec{r}_j|^2 + \epsilon h^2}, \quad (1.127)$$

³²Other kernels with higher-order accuracy (i.e., h^4) have also been proposed, but their applicability is challenged by a number of effects. See Benz [153] for a detailed discussion.

where ϵh^2 is added to avoid divergence for small values of $|\vec{r}_i - \vec{r}_j|$. This translates into a pressure term that is added to the momentum conservation equation in the form

$$\prod_{ij} = \frac{M}{\pi h^3} \begin{cases} \frac{-\alpha c_{ij} \mu_{ij} + \beta \mu_{ij}^2}{\rho_{ij}}, & \text{if } (\vec{u}_i - \vec{u}_j)(\vec{r}_i - \vec{r}_j) \leq 0 \\ 0, & \text{otherwise,} \end{cases} \quad (1.128)$$

where $c_{ij} \equiv (c_i + c_j)/2$ and $\rho_{ij} \equiv (\rho_i + \rho_j)/2$ are the average speed of sound and density, respectively.

- Momentum conservation

$$\frac{d\vec{u}_i}{dt} = - \sum_j \left(\frac{P_i}{\rho_i^2} + \frac{P_j}{\rho_j^2} + \prod_{ij} \right) \nabla W(\vec{r}_i - \vec{r}_j, h) - \nabla \Phi_i, \quad (1.129)$$

where $\nabla \Phi_i$ corresponds to the gravitational force per unit mass acting on particle i , which can be obtained by application of Poisson's equation as

$$\nabla \Phi_i = G \sum_j 4\pi \frac{\vec{r}_{ij}}{|\vec{r}_{ij}|^3} \int_0^{|\vec{r}_{ij}|} W(x, h) x^2 dx. \quad (1.130)$$

The above expression does not vanish unless the distance between particles i and j is infinite. Moreover, if the summation is not done properly, the method will translate into a computational cost proportional to N^2 , where N is the number of particles. A possible way out involves the use of a *hierarchical tree*, which allows a fast track of the neighboring particles and reduces the computational cost to $N \log N$. To this end, a widely used prescription in the Barnes–Hut algorithm [130], first implemented in SPH codes by Hernquist and Katz [789], to which the reader is referred for further details. Integration and time evolution of the system is finally handled by means of a simple algorithm (e.g., Runge–Kutta, predictor–corrector). Further details on SPH methods can be found in references [1120, 1258, 1259, 1531, 1533, 1688, 1689].

1.6 Building a 1D Hydrodynamic Code

In the absence of magnetic fields, a nonrotating stellar plasma can be described in spherical symmetry by the system of nonlinear, coupled differential equations discussed in Section 1.2. The system cannot be solved analytically, and numerical techniques need to be implemented.

This section outlines the basic strategies undertaken in the design of a stellar evolution code³³ in a simplified framework. To this end, a 1D, spherically symmetric, Lagrangian, implicit, hydrodynamic code, aimed at characterizing the free-fall collapse of a homogeneous sphere, will be built from scratch³⁴.

1.6.1 Differential Equations for the Free-Fall Collapse Problem

Let's consider a homogeneous, spherical plasma in hydrostatic equilibrium (i.e., the gravitational pull is balanced by a pressure gradient). If forces due to pressure gradients are

³³See Table 1.1 for examples of hydro codes used in the study of stellar explosions.

³⁴The computer program, `freefall.f`, written in Fortran, is actually listed in Appendix B and can also be downloaded from <http://fisica.upc.edu/ca/users/jjose/CRC-Downloads>.

TABLE 1.1

Examples of Hydro Codes Used in the Study of Stellar Explosions

Code	Stellar* explosion	Main properties and reference papers
AGILE	SNII, XRB	1D, implicit/explicit, Lagrangian, general relativistic [533, 1109]
AxisSPH	WD+WD mergers	2D (axisymmetric) SPH, explicit, Lagrangian; Parallelized [616]
DJEHUTY	CN, SNIa, SNII	3D, explicit, ALE; Parallelized [143, 421]
FLASH	CN, XRB, SNIa	3D, explicit, Eulerian; Parallelized [567]
FRANEC	SNII	1D, fully implicit, Lagrangian, with rotation [324, 1110]
GADGET2	CN	3D SPH, explicit, Lagrangian; Parallelized [1687]
KEPLER	CN, XRB, SNIa, GRB, SNII	1D, implicit, Lagrangian with rotation; Parallelized [1475, 1911]
MESA	CN, XRB, SNIa	1D, implicit/explicit, Lagrangian, with rotation; Parallelized [1396, 1397]
NOVA	CN, XRB, SNIa	1D, implicit/explicit, Lagrangian [1037, 1706]
PROMETHEUS	CN, SNIa SNII	3D, explicit, Eulerian; Parallelized [566, 985]
SHIVA	CN, XRB, SNIa	1D, implicit/explicit, Lagrangian, with rotation; Parallelized [919, 927]
SPH	WD+WD(NS) mergers	3D SPH, explicit, Lagrangian [97, 1151]
SPHYNX	SNIa, SNII	3D SPH, explicit, Lagrangian; Parallelized [613]
TYCHO	SNIa, SNII	1D, implicit/explicit, Lagrangian [67, 2007]
VULCAN	CN, SNIa, SNII	2D, implicit/explicit, ALE; Parallelized [649, 1130]

*Acronyms: Classical novae (CN); type Ia supernovae (SNIa); type II supernovae (SNII); X-ray bursts (XRB); γ -ray bursts (GRB); white dwarfs (WD); neutron stars (NS); smoothed-particle hydrodynamics (SPH); arbitrary Lagrangian–Eulerian (ALE).

neglected (i.e., $P = 0$), the dynamics of the system is governed only by gravity, and a free-fall collapse will ensue. Since no shock is expected during the collapse, artificial viscosity can be removed ($q = 0$). In such conditions, the collapse can be described by the following set of differential equations:

- Conservation of mass

$$\frac{1}{\rho} = \frac{4}{3}\pi \frac{\partial r^3}{\partial m} \quad (1.131)$$

- Conservation of momentum ($P = q = 0$)

$$\frac{\partial u}{\partial t} = -G \frac{m}{r^2} \quad (1.132)$$

- Lagrangian velocity

$$\frac{\partial r}{\partial t} = u \quad (1.133)$$

1.6.2 Variable Assignment

Solutions to the set of differential equations described in Section 1.6.1 will be obtained for a discrete number of points within the sphere. To this end, a suitable computational grid is built by dividing the sphere into N concentric layers or shells, with equal or different masses and sizes (for simplicity, we will assume hereafter that all concentric shells have the same mass).

A decision has to be made with regard to variable assignment to specific grid points. Let's assume, for instance, that radii and velocities are assigned to each intershell while densities are instead evaluated at midpoints, on the basis of symmetry arguments inspired by the form of the mass conservation equation (see Figure 1.11). For convenience, the mass enclosed in each spherical shell, or *interior mass*, m_i , is also assigned to each intershell. Note, however, that this choice is somewhat arbitrary and alternative criteria for variable assignment could be adopted.

1.6.3 Discretization

The set of partial differential equations reviewed in Section 1.6.1 is subsequently replaced by the following system in finite difference form:

- Conservation of mass

$$\frac{1}{(\rho_{i+1/2})^{n+1}} = \frac{4}{3}\pi \frac{(r_{i+1}^3)^{n+1} - (r_i^3)^{n+1}}{m_{i+1} - m_i} \quad (1.134)$$

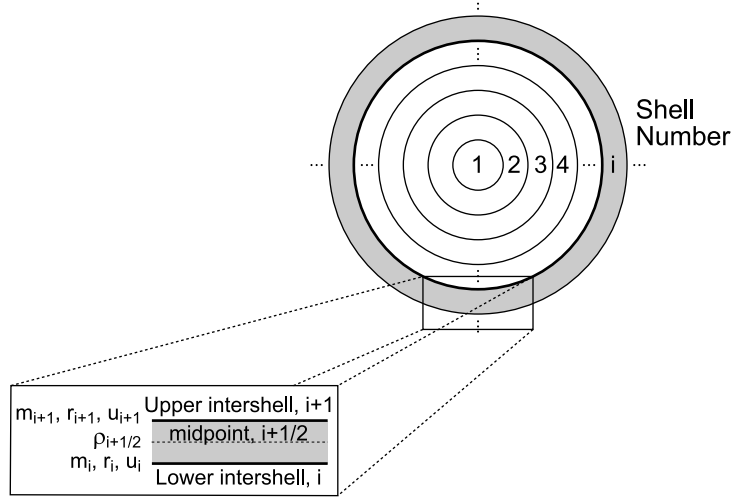
- Conservation of momentum

$$\frac{u_{i+1}^{n+1} - u_i^n}{\Delta t} = (1 - \beta) \left(\frac{-Gm_{i+1}}{r_{i+1}^2} \right)^n + \beta \left(\frac{-Gm_{i+1}}{r_{i+1}^2} \right)^{n+1} \quad (1.135)$$

- Lagrangian velocity

$$\frac{r_{i+1}^{n+1} - r_i^n}{\Delta t} = (1 - \beta)u_{i+1}^n + \beta u_{i+1}^{n+1}, \quad (1.136)$$

where superscripts n and $n + 1$ denote variables evaluated at times t^n and $t^{n+1} = t^n + \Delta t$. β is the interpolation parameter introduced in Equation 1.96 that characterizes explicit ($\beta = 0$) and implicit ($\beta \neq 0$) schemes.

**FIGURE 1.11**

Shell structure and variable assignment in the 1D free-fall collapse problem. Note that masses, radii, and velocities are assigned to the intershells, while densities are instead assigned to shell midpoints.

1.6.4 Initial Models, Boundary Conditions, and Scaling

If the N concentric shells contain the same mass, $\Delta m \equiv M_{\text{tot}}/N$, the interior mass variable m_i is simply given by:

$$m_{i+1} = i \Delta m \quad (i = 1, N). \quad (1.137)$$

Note that $m_{N+1} \equiv M_{\text{tot}}$, by construction, with $M_{\text{tot}} = \frac{4}{3}\pi R_o^3 \rho_o$ for a homogeneous sphere of initial radius R_o and density ρ_o .

If the computational domain extends all the way from the center of the sphere to its surface³⁵, the radius and interior mass variable at the first intershell trivially become $r_1 = m_1 = 0$. Moreover, for a homogenous sphere, $\rho_{i+1/2} \equiv \rho_o$ ($i = 1, N$), by definition, and assuming an initial static configuration, $u_i = 0$ ($i = 1, N + 1$) at $t = 0$.

Once boundary conditions are applied to the innermost shell, mass conservation equation becomes

$$r_2 = \left(\frac{3m_2}{4\pi\rho_{3/2}} \right)^{1/3} \quad (1.138)$$

for $r_1 = m_1 = 0$, while the radii of the subsequent intershells can be obtained through

$$\begin{aligned} r_{i+1} &= \left(\frac{3(m_{i+1} - m_i)}{4\pi\rho_{i+1/2}} + r_i^3 \right)^{1/3} = \\ &\left(\frac{3\Delta m}{4\pi\rho_{i+1/2}} + r_i^3 \right)^{1/3} \quad (i = 2, N). \end{aligned} \quad (1.139)$$

³⁵In some applications, the computational domain does not necessarily cover the whole physical system. Localized, stellar thermonuclear explosions, for instance, can be numerically handled by restricting to smaller computational domains, therefore increasing the resolution at the regions of interest while speeding up the calculations. In such cases, the innermost shell is not located at the center of the star (i.e., $m_1 \neq 0$), but placed at a suitable depth where no physical changes are actually expected. Accordingly, the inner boundary conditions are simply given by the initial values of the radius and velocity at m_1 , which are assumed to remain constant throughout the calculation.

Finally, rescaling of certain physical variables will be used to avoid numerical problems. In particular, the interior mass m_i will be rewritten as $Q_i = 1 - m_i/M_{\text{tot}}$, while $V_{i+1/2} = 1/\rho_{i+1/2}$ and r_i will be replaced by their natural logarithms, $R_i = \ln(r_i)$, $W_{i+1/2} = \ln(V_{i+1/2})$, thus limiting their ranges of variation.

1.6.5 Henyey Method

Several methods have been proposed for solving the stellar structure equations with fixed boundary conditions. They are often classified into two broad categories: shooting³⁶ and relaxation methods.

The most extensively used in stellar evolution are a class of relaxation methods generically known as Newton–Raphson. They rely on the linearization of the set of finite difference equations. The methodology adopted in a generalized Newton–Raphson method (sometimes called Henyey method³⁷) [764,987] will be the subject of an in-depth analysis in this section.

1.6.5.1 Equations for the Innermost Shell

The finite difference equations for the innermost shell of the sphere, with the corresponding boundary conditions, can be written in compact form as a function C that depends on a number of unknowns. Let's start with the mass conservation equation: for $m_1 = r_1 = u_1 = 0$, it can be written as

$$C^1 = \frac{1}{(\rho_{3/2})^{n+1}} - \frac{4}{3}\pi \frac{(r_2^3)^{n+1}}{m_2} = C^1(r_2, \rho_{3/2}) = 0. \quad (1.140)$$

Momentum conservation and the equation for the Lagrangian velocity can, in turn, be expressed as:

$$\begin{aligned} C^2 &= \frac{u_2^{n+1} - u_2^n}{\Delta t} - (1 - \beta) \left(\frac{-Gm_2}{r_2^2} \right)^n - \beta \left(\frac{-Gm_2}{r_2^2} \right)^{n+1} = \\ &C^2(u_2, r_2) = 0, \end{aligned} \quad (1.141)$$

$$C^3 = \frac{r_2^{n+1} - r_2^n}{\Delta t} - (1 - \beta)u_2^n - \beta u_2^{n+1} = C^3(u_2, r_2) = 0. \quad (1.142)$$

Globally, this set of equations can be written as a function of just 3 unknowns, u_2 , r_2 , and $\rho_{3/2}$, such that

$$C^j = C^j(\rho_{3/2}, u_2, r_2) = 0 \quad (j = 1, 3). \quad (1.143)$$

1.6.5.2 Equations for the Intermediate Shells

The same procedure is then applied to the $N - 2$ intermediate shells ($i = 2, N - 1$), in the form:

$$F_i^1 = \frac{1}{(\rho_{i+1/2})^{n+1}} - \frac{4}{3}\pi \frac{(r_{i+1}^3)^{n+1} - (r_i^3)^{n+1}}{m_{i+1} - m_i} = F_i^1(r_{i+1}, r_i, \rho_{i+1/2}) = 0, \quad (1.144)$$

³⁶Shooting methods, also known as fitting or matching point methods, rely on a double integration of the stellar structure equations, one starting from the center outward, the other from the surface inward. In general, both integrations do not match, and variations of the initial guess values adopted at both edges are required. While useful for constructing equilibrium configurations, it turned out that shooting methods are in general unsuitable for complex stellar models (see discussion in reference [988]).

³⁷See Appendix A for an extension of the Henyey method to arbitrary hydrodynamic problems. Further generalizations of the Henyey method for an arbitrary set of differential equations can be found, e.g., in references [1313, 1948].

$$F_i^2 = \frac{u_{i+1}^{n+1} - u_i^n}{\Delta t} - (1 - \beta) \left(\frac{-Gm_{i+1}}{r_{i+1}^2} \right)^n - \beta \left(\frac{-Gm_{i+1}}{r_{i+1}^2} \right)^{n+1} = F_i^2(u_{i+1}, r_{i+1}) = 0, \quad (1.145)$$

$$F_i^3 = \frac{r_{i+1}^{n+1} - r_i^n}{\Delta t} - (1 - \beta)u_{i+1}^n - \beta u_{i+1}^{n+1} = F_i^3(u_{i+1}, r_{i+1}) = 0, \quad (1.146)$$

or globally,

$$F_i^j = F_i^j(\rho_{i+1/2}, r_i, r_{i+1}, u_{i+1}) = 0 \quad (i = 2, N - 1; j = 1, 3). \quad (1.147)$$

1.6.5.3 Equations for the Outermost Shell

Finally, for the outermost shell ($i = N$), we have

$$S^1 = \frac{1}{(\rho_{N+1/2})^{n+1}} - \frac{4}{3}\pi \frac{(r_{N+1})^{n+1} - (r_N^n)^{n+1}}{m_{N+1} - m_N} = S^1(r_{N+1}, r_N, \rho_{N+1/2}) = 0, \quad (1.148)$$

$$S^2 = \frac{u_{N+1}^{n+1} - u_{N+1}^n}{\Delta t} - (1 - \beta) \left(\frac{-Gm_{N+1}}{r_{N+1}^2} \right)^n - \beta \left(\frac{-Gm_{N+1}}{r_{N+1}^2} \right)^{n+1} = S^2(u_{N+1}, r_{N+1}) = 0, \quad (1.149)$$

$$S^3 = \frac{r_{N+1}^{n+1} - r_{N+1}^n}{\Delta t} - (1 - \beta)u_{N+1}^n - \beta u_{N+1}^{n+1} = S^3(u_{N+1}, r_{N+1}) = 0, \quad (1.150)$$

which can be written as:

$$S^j = S^j(\rho_{N+1/2}, r_N, r_{N+1}, u_{N+1}) = 0 \quad (j = 1, 3). \quad (1.151)$$

1.6.6 Linearization

Let x^0 be a vector containing the *exact* values of the physical variables of the problem, r , ρ , and u , at $t^0 = 0$ (i.e., initial model), or, in general, at a given time, t^n . Let x^1 be the corresponding vector after one step, $t^1 = t^0 + \Delta t$. For small enough values of the timestep, Δt , all physical variables would have scarcely varied from their values at t^0 (i.e., $x^1 \sim x^0$). Therefore, let's consider, as a first approximate guess, that $x^1 \equiv x^0$. In general, such a choice would not yield the exact values of the variables at t^1 , so that $C^j(x^1) \neq 0$, $F_i^j(x^1) \neq 0$, and $S^j(x^1) \neq 0$. Nevertheless, since $x^1 \sim x^0$, one can think of a set of corrections, δx , that added to the first guess values, $x^1 = x^0 + \delta x$, will actually satisfy $C^j(x^1) = 0$, $F_i^j(x^1) = 0$, and $S^j(x^1) = 0$. For small corrections, the whole set of structure equations can be written in the form

$$\begin{aligned} C^j(x^1) &= C^j(x^0) + \delta C^j = 0 \\ F_i^j(x^1) &= F_i^j(x^0) + \delta F_i^j = 0 \\ S^j(x^1) &= S^j(x^0) + \delta S^j = 0, \end{aligned} \quad (1.152)$$

which correspond to the following linearized system of equations,

$$C^j + \frac{\partial C^j}{\partial \rho_{3/2}} \delta \rho_{3/2} + \frac{\partial C^j}{\partial u_2} \delta u_2 + \frac{\partial C^j}{\partial r_2} \delta r_2 = 0 \quad (1.153)$$

$$F_i^j + \frac{\partial F_i^j}{\partial \rho_{i+1/2}} \delta \rho_{i+1/2} + \frac{\partial F_i^j}{\partial r_i} \delta r_i + \frac{\partial F_i^j}{\partial r_{i+1}} \delta r_{i+1} + \frac{\partial F_i^j}{\partial u_{i+1}} \delta u_{i+1} = 0$$

$$(j = 1, 3; i = 2, N - 1) \quad (1.154)$$

$$S^j + \frac{\partial S^j}{\partial \rho_{N+1/2}} \delta \rho_{N+1/2} + \frac{\partial S^j}{\partial r_N} \delta r_N + \frac{\partial S^j}{\partial r_{N+1}} \delta r_{N+1} + \frac{\partial S^j}{\partial u_{N+1}} \delta u_{N+1} = 0 \\ (j = 1, 3), \quad (1.155)$$

where all partial derivatives can be determined analytically. For instance, for the innermost shell (see Section 1.6.5.1), we have:

$$\frac{\partial C^1}{\partial \rho_{3/2}} = -\frac{1}{\rho_{3/2}^2} \quad (1.156)$$

$$\frac{\partial C^1}{\partial u_2} = 0 \quad (1.157)$$

$$\frac{\partial C^1}{\partial r_2} = -4\pi \frac{r_2^2}{m_2} \quad (1.158)$$

$$\frac{\partial C^2}{\partial \rho_{3/2}} = 0 \quad (1.159)$$

$$\frac{\partial C^2}{\partial u_2} = \frac{1}{\Delta t} \quad (1.160)$$

$$\frac{\partial C^2}{\partial r_2} = -\beta \frac{G m_2}{r_2^2} \quad (1.161)$$

$$\frac{\partial C^3}{\partial \rho_{3/2}} = 0 \quad (1.162)$$

$$\frac{\partial C^3}{\partial u_2} = -\beta \quad (1.163)$$

$$\frac{\partial C^3}{\partial r_2} = \frac{1}{\Delta t}. \quad (1.164)$$

Note that all variables evaluated at previous time (i.e., t^0 , or in general, at an arbitrary time t^n) are fixed, therefore nonzero derivatives involve only variables evaluated at the current time, t^1 (t^{n+1} , in general).

This system of linearized equations can also be written in matrix form, $\mathbf{A} \cdot \mathbf{B} = \mathbf{C}$ (see Equation 1.165). In principle, one would be tempted to obtain the matrix containing the set of correction values δ from $\mathbf{B} = \mathbf{A}^{-1} \cdot \mathbf{C}$. Since typically 1D computational domains are discretized in $N \sim 100 - 1000$ shells, for the free-fall collapse problem with 3 unknowns per shell, matrix \mathbf{A} has a characteristic size $3N \times 3N$, that is, contains a number of elements ranging from 300×300 to 3000×3000 . Such large matrices are, in general, not easy to handle numerically. Note, however, that the linearized system of equations for the innermost shell corresponds to

$$C^j + \frac{\partial C^j}{\partial \rho_{3/2}} \delta \rho_{3/2} + \frac{\partial C^j}{\partial u_2} \delta u_2 + \frac{\partial C^j}{\partial r_2} \delta r_2 = 0, \quad (1.166)$$

$$\begin{pmatrix}
 \frac{\partial C^1}{\partial \rho_{3/2}} & \frac{\partial C^1}{\partial r_2} & 0 & 0 & 0 & 0 & 0 & 0 & 0 & \dots & 0 & 0 & 0 \\
 0 & \frac{\partial C^2}{\partial r_2} & \frac{\partial C^2}{\partial u_2} & 0 & 0 & 0 & 0 & 0 & 0 & \dots & 0 & 0 & 0 \\
 0 & \frac{\partial C^3}{\partial r_2} & \frac{\partial C^3}{\partial u_2} & 0 & 0 & 0 & 0 & 0 & 0 & \dots & 0 & 0 & 0 \\
 0 & \frac{\partial F_2^1}{\partial r_2} & 0 & \frac{\partial F_2^1}{\partial \rho_{5/2}} & \frac{\partial F_2^1}{\partial r_3} & 0 & 0 & 0 & 0 & \dots & 0 & 0 & 0 \\
 0 & 0 & 0 & 0 & \frac{\partial F_2^2}{\partial r_3} & \frac{\partial F_2^2}{\partial u_3} & 0 & 0 & 0 & \dots & 0 & 0 & 0 \\
 0 & 0 & 0 & 0 & \frac{\partial F_2^3}{\partial r_3} & \frac{\partial F_2^3}{\partial u_3} & 0 & 0 & 0 & \dots & 0 & 0 & 0 \\
 0 & 0 & 0 & 0 & \frac{\partial F_3^1}{\partial r_3} & 0 & \frac{\partial F_3^1}{\partial \rho_{7/2}} & \frac{\partial F_3^1}{\partial r_4} & 0 & \dots & 0 & 0 & 0 \\
 0 & 0 & 0 & 0 & 0 & 0 & 0 & \frac{\partial F_3^2}{\partial r_4} & \frac{\partial F_3^2}{\partial u_4} & \dots & 0 & 0 & 0 \\
 0 & 0 & 0 & 0 & 0 & 0 & 0 & \frac{\partial F_3^3}{\partial r_4} & \frac{\partial F_3^3}{\partial u_4} & \dots & 0 & 0 & 0 \\
 \vdots & \dots & \vdots & \vdots & \vdots \\
 0 & 0 & 0 & 0 & 0 & 0 & 0 & 0 & 0 & \dots & \frac{\partial S^1}{\partial \rho_{N+1/2}} & \frac{\partial S^1}{\partial r_{N+1}} & 0 \\
 0 & 0 & 0 & 0 & 0 & 0 & 0 & 0 & 0 & \dots & 0 & \frac{\partial S^2}{\partial r_{N+1}} & \frac{\partial S^2}{\partial u_{N+1}} \\
 0 & 0 & 0 & 0 & 0 & 0 & 0 & 0 & 0 & \dots & 0 & \frac{\partial S^3}{\partial r_{N+1}} & \frac{\partial S^3}{\partial u_{N+1}}
 \end{pmatrix} = \begin{pmatrix} \delta \rho_{3/2} \\ \delta r_2 \\ \delta u_2 \\ \delta \rho_{5/2} \\ \delta r_3 \\ \delta u_3 \\ \delta \rho_{7/2} \\ \delta r_4 \\ \delta u_4 \\ \dots \\ \delta \rho_{N+1/2} \\ \delta r_{N+1} \\ \delta u_{N+1} \end{pmatrix} = \begin{pmatrix} -C^1 \\ -C^2 \\ -C^3 \\ -F_2^1 \\ -F_2^2 \\ -F_2^3 \\ -F_3^1 \\ -F_3^2 \\ -F_3^3 \\ \dots \\ -S^1 \\ -S^2 \\ -S^3 \end{pmatrix} \quad (1.165)$$

which, after moving the C^j term to the right-hand side of the equation, can be written in the following simple matrix form:

$$\begin{pmatrix} \frac{\partial C^1}{\partial \rho_{3/2}} & \frac{\partial C^1}{\partial u_2} & \frac{\partial C^1}{\partial r_2} \\ \frac{\partial C^2}{\partial \rho_{3/2}} & \frac{\partial C^2}{\partial u_2} & \frac{\partial C^2}{\partial r_2} \\ \frac{\partial C^3}{\partial \rho_{3/2}} & \frac{\partial C^3}{\partial u_2} & \frac{\partial C^3}{\partial r_2} \end{pmatrix} \begin{pmatrix} \delta \rho_{3/2} \\ \delta u_2 \\ \delta r_2 \end{pmatrix} = \begin{pmatrix} -C^1 \\ -C^2 \\ -C^3 \end{pmatrix}, \quad (1.167)$$

Since the system contains 3 equations and just 3 unknowns (i.e., $\delta \rho_{3/2}$, δu_2 , and δr_2), it can be solved in a straightforward way.

Now, let's scrutinize the linearized system of equations for the $N - 2$ intermediate shells,

$$F_i^j + \frac{\partial F_i^j}{\partial \rho_{i+1/2}} \delta \rho_{i+1/2} + \frac{\partial F_i^j}{\partial r_i} \delta r_i + \frac{\partial F_i^j}{\partial r_{i+1}} \delta r_{i+1} + \frac{\partial F_i^j}{\partial u_{i+1}} \delta u_{i+1} = 0 \\ (j = 1, 3; i = 2, N - 1), \quad (1.168)$$

which as well can be written in matrix form:

$$\begin{pmatrix} \frac{\partial F_i^1}{\partial \rho_{i+1/2}} & \frac{\partial F_i^1}{\partial u_{i+1}} & \frac{\partial F_i^1}{\partial r_{i+1}} \\ \frac{\partial F_i^2}{\partial \rho_{i+1/2}} & \frac{\partial F_i^2}{\partial u_{i+1}} & \frac{\partial F_i^2}{\partial r_{i+1}} \\ \frac{\partial F_i^3}{\partial \rho_{i+1/2}} & \frac{\partial F_i^3}{\partial u_{i+1}} & \frac{\partial F_i^3}{\partial r_{i+1}} \end{pmatrix} \begin{pmatrix} \delta \rho_{i+1/2} \\ \delta u_{i+1} \\ \delta r_{i+1} \end{pmatrix} = \begin{pmatrix} -F_i^1 - \frac{\partial F_i^1}{\partial r_i} \delta r_i \\ -F_i^2 - \frac{\partial F_i^2}{\partial r_i} \delta r_i \\ -F_i^3 - \frac{\partial F_i^3}{\partial r_i} \delta r_i \end{pmatrix}. \quad (1.169)$$

For $i = 2$, δr_2 is no longer an unknown, since such correction was already obtained in the analysis of the innermost shell. The same applies to δr_i for an arbitrary intermediate shell, i . For convenience, δr_i can be simply moved to the right-hand side of the equations. As for the innermost shell, the system contains 3 equations ($j = 1, 3$) and just 3 unknowns (i.e., $\delta \rho_{i+1/2}$, δu_{i+1} , and δr_{i+1}) and can again be easily solved. The procedure described above for the first intermediate shell can be extended to the additional intermediate shells, as well as to the surface layer. Therefore, the solution of the system that characterizes the free-fall collapse problem involves N matrices containing 3×3 elements, rather than dealing with a huge $3N \times 3N$ matrix³⁸.

The freshly determined δ corrections are then added to the first guess values x^o , such that $x^1 = x^o + \delta x$. The process is then iterated: Functions and derivatives are recalculated with the improved values x^1 , and a new set of δ corrections is obtained. When small enough corrections result, for all variables at all shells, satisfying $\delta X/X < \epsilon$ (with ϵ being a pre-determined accuracy parameter), the iteration process is halted, and the system is advanced one step, $t^2 = t^1 + \Delta t$.

1.6.7 Theory vs. Simulation

The procedure described above (Sections 1.6.2–1.6.6) has been specifically designed for the simulation of the free-fall collapse of a homogeneous sphere. The problem has an analytical

³⁸Unfortunately, the usual situation faced in computational hydrodynamics is not that simple, and one has to deal unavoidably with the decomposition of the overall matrix, for which special techniques have been developed (see Appendix A).

solution [366] that can be obtained inserting the definition of velocity in the momentum conservation equation (with $P = 0$, and no artificial viscosity), while assuming that the homogeneous sphere is initially at rest ($u = 0 \text{ cm s}^{-1}$, at $t = t_o$). All in all, the corresponding solution can be written as:

$$\left(8\pi G \frac{\rho_o}{3}\right)^{1/2} (t - t_o) = \left(1 - \frac{R}{R_o}\right)^{1/2} \left(\frac{R}{R_o}\right)^{1/2} + \arcsin\left(1 - \frac{R}{R_o}\right)^{1/2}, \quad (1.170)$$

where ρ_o and R_o are the initial density and radius of the sphere, and G is the gravitational constant.

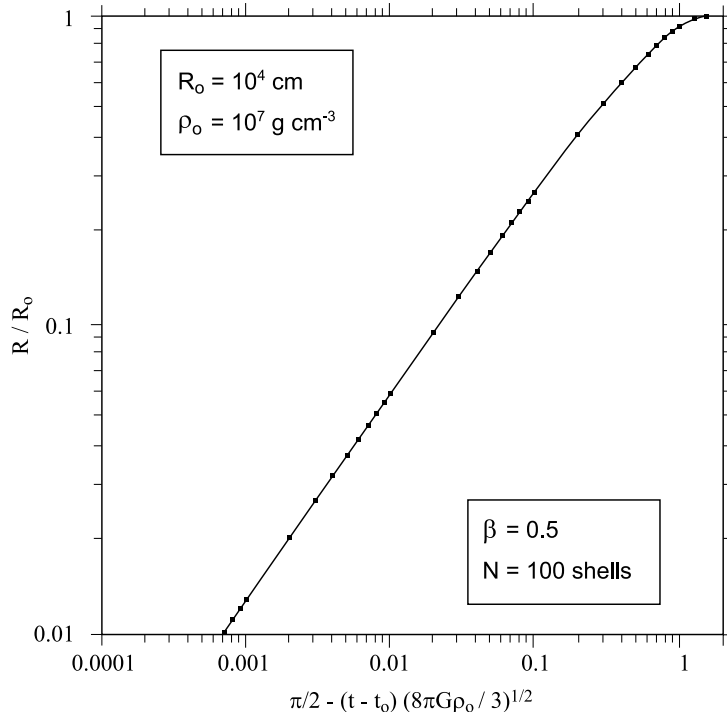
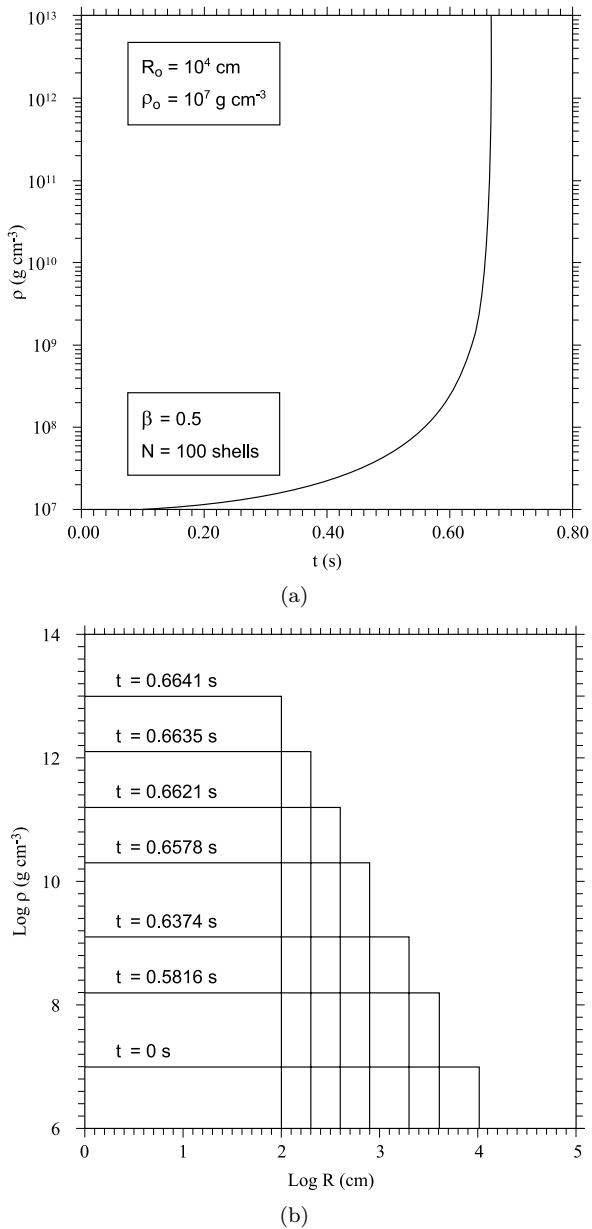


FIGURE 1.12

Simulation of the free-fall collapse of a homogeneous sphere. Note the agreement between the analytical solution (solid line) and the numerical results (points). Simulation performed with the code `freefall.f` (see Appendix B), with $\beta = 0.5$.

Results of a simulation for an initial density $\rho_o = 10^7 \text{ g cm}^{-3}$ and radius $R_o = 10^4 \text{ cm}$, modeled as 100 equal mass, numerical shells, with the code `freefall.f` (see Appendix B) are shown in Figures 1.12 and 1.13. Note the excellent agreement between the numerical results and the analytical solution, even when the sphere has already shrunk in size by two orders of magnitude.

In about 0.6 s, the density of the sphere has already increased by six orders of magnitude (Figure 1.13) but, as theoretically predicted, homogeneity is maintained throughout the sphere (with a relative error $\leq 10^{-6}\%$). This defines a homologous collapse, with a constant temperature and a uniform density across the sphere. Note also that since $\rho \propto R^{-3}$, a plot of the density versus radius has a constant slope in a log-log R plane.

**FIGURE 1.13**

(a) Evolution of the central density as a function of time and (b) density profile versus radius, for the free-fall collapse problem.

1.7 Code Validation and Verification

Hydrocodes are computer-friendly models of nature, in which the standard suite of partial differential equations (often representing conservation laws) are commonly replaced by simpler, approximate expressions. As such, the way in which a hydrocode describes a physical phenomenon can only be regarded as approximate. The degree in which a numerical solution represents the true solution of a problem is a major concern for theorists and often implies substantial tests to validate and verify each code's capabilities and their performance.

Verification and validation are fundamental aspects in code development [996, 1338, 1505, 1790]. While a verification assessment is aimed at proving whether the computational implementation of the conceptual model is correct, validation basically determines whether a simulation agrees with nature [283]. As nicely summarized by P. Roache [1505], verification tests whether a code “solves the equations right”, while validation checks whether a code is “solving the right equations”. Remarkably, verification and validation are necessary but not sufficient strategies to check the performance of a code, and one should not forget that through such tests, one can never prove whether a code works correctly, only that a code fails or does not work properly.

Verification tests often rely on a suite of problems with analytical solution. The performance of the code is therefore checked by means of a thorough comparison between the analytical and the numerical solutions. Unfortunately, test cases with analytical solution are frequently so simple and rare that only a subset of code modules or subroutines are actually checked. Code-to-code comparison turns out to be an appealing alternative, although it is not always easy to overcome the natural reluctance of competing teams in showing “the kitchen”, so to speak³⁹.

On the other hand, validation involves confirmation of the numerical results through laboratory experiments. Often, validation problems are much more complex than verification tests, and therefore are frequently devoid of analytical solution. Validation tests are used to assess resolution issues and the level of refinement required to reproduce the relevant physics of a problem. Such tests may be hampered by a number of experimental issues, such as limited experimental resolution, or not well-known material properties. On the computational side, main difficulties arise from the impossibility to resolve all the relevant length- and timescales of the problem, which make a direct comparison with experiments sometimes hard to interpret. And frequently, stellar codes lack fundamental physics inputs to reproduce a real experiment in terrestrial conditions (e.g., thermal diffusion, appropriate equation of state, viscosity).

All in all, verification and validation can be regarded as important but challenging stages in the art of scientific computing and, in particular, in the modeling of stellar explosions.

1.7.1 Verification Tests

The free-fall collapse problem of a homogeneous sphere, discussed in Section 1.6.7, is just one of myriad classical tests frequently used in the verification of hydrodynamic codes. Other examples, computed with the multidimensional code FLASH, are described in the following subsections.

³⁹While a common practice in multidimensional hydrodynamics, comparison between stellar evolution codes is much more scarce. An initiative in this regard was pushed by the AGB modeling community back in the 1990s, in the framework of the early Torino workshops, in an effort to share and compare the performance of the different codes used in their simulations.

1.7.1.1 Sod's Shock Tube Test

Sod's shock tube problem, a standard Riemann problem in Newtonian fluid dynamics, has become the quintessential benchmark test for hydro codes. Named after Gary Sod [1675], it tests the ability of a numerical algorithm to handle discontinuities and shocks (in particular, whether the Rankine–Hugoniot conditions are satisfied; see Section 1.3.3). An asset of this test relies on the possibility of comparing results with an analytical solution when a simple equation of state⁴⁰ is implemented.

The test consists of two fluids, initially at rest, with different densities and pressures, separated by a planar interface. When the interface is removed ($t = 0$), a characteristic fluid pattern that can be experimentally validated emerges [1724]. Five distinct regions are identified (Figure 1.14): the undisturbed left fluid (region I), the expanding left fluid (II), the decompressed left fluid (III), the compressing right fluid (IV), and the undisturbed right fluid (V).

Even though the analytical solution of Sod's shock tube problem is rather complex, a number of relevant features can be easily addressed⁴¹. The flow in regions III and IV is characterized by a constant density. Such regions are actually separated by a *contact discontinuity*, that is, a dividing line that separates two fluids with different entropy but identical pressure and velocity (see Figures 1.14 and 1.15). Therefore, $u_{\text{III}} = u_{\text{IV}}$ and $P_{\text{III}} = P_{\text{IV}}$. The contact discontinuity propagates with the fluid, at $u_{\text{cont}} = u_{\text{III}}$, and hence, its location is determined by $x_{\text{cont}} = u_{\text{cont}} t + x_0$, with x_0 being the initial position of the planar interface. Region II, the only nonsteady region in the solution, is instead characterized by an x -dependent density profile, imposed by the propagation of an expansion wave that moves to the left (i.e., a *rarefaction fan*; see Figure 1.14).

Regions IV and V are in turn separated by a shock wave that propagates to the right. Since region V is unperturbed, $u_V = 0$. The speed at which the shock wave propagates can be directly evaluated from mass conservation,

$$u_{\text{shock}} = u_{\text{IV}} \frac{\rho_{\text{IV}}}{\rho_{\text{IV}} - \rho_V}, \quad (1.171)$$

while the location of the shock is simply given by $x_{\text{shock}} = u_{\text{shock}} t + x_0$.

Following Bodenheimer et al. [209], the velocity in region IV is given by

$$u_{\text{IV}} = (P_{\text{IV}} - P_V) \sqrt{\frac{1 - \omega^2}{\rho_V (P_{\text{IV}} + \omega^2 P_V)}}, \quad (1.172)$$

while the relation between u and P in region II can be written as

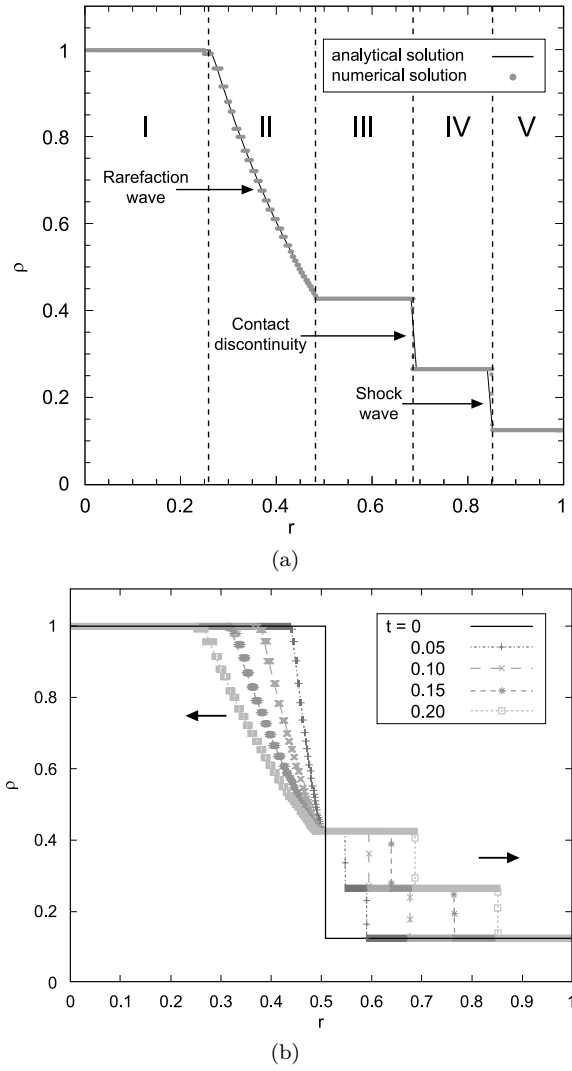
$$u_{\text{II}} = (P_{\text{I}}^\psi - P_{\text{II}}^\psi) \sqrt{\frac{P_{\text{I}}^{1/\gamma} (1 - \omega^4)}{\rho_{\text{I}} \omega^4}}, \quad (1.173)$$

where $\psi = (\gamma - 1)/2\gamma$ (see reference [741] for a full derivation of Equations 1.172 and 1.173).

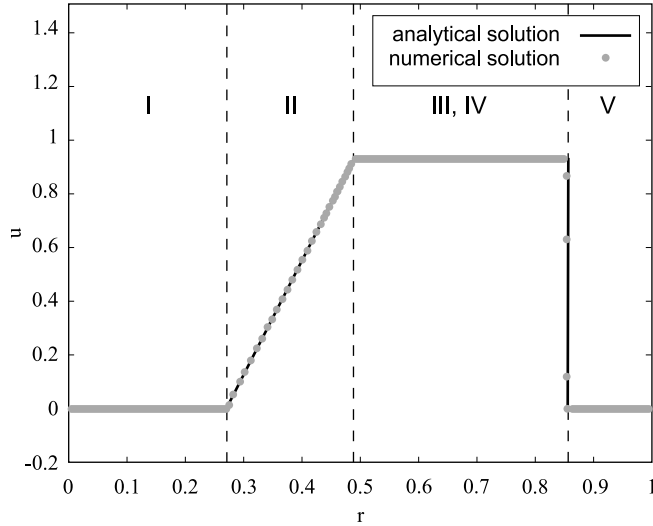
On a $P - u$ plane, Equations 1.172 and 1.173 represent the loci of all the possible states of the fluid in regions II to IV. Both curves intersect at a point, where the portion of the fluid expanded in regions II and III smoothly matches the shocked flow in region IV. Therefore,

⁴⁰In this section, a polytropic equation of state, $P = K\rho^\gamma = K\rho^{(n+1)/n}$, is adopted, with K the polytropic constant, and n the polytropic index.

⁴¹See references [741, 1149] for a detailed derivation. A Fortran code aimed at testing Sod's shock tube problem, developed by Bruce Fryxell and Frank Timmes, is available at http://cococubed.asu.edu/code_pages/exact_riemann.shtml.

**FIGURE 1.14**

(a) Density profile at $t = 0.2$, in Sod's shock tube problem, as computed with the FLASH code. The plot displays the five distinct regions predicted theoretically, as well as the formation of a rarefaction wave, a shock wave, and a contact discontinuity (see text for details).
 (b) Density profiles at times $t = 0, 0.05, 0.1, 0.15$, and 0.2 units, in Sod's shock tube problem. Color plots and a movie portraying the time-evolution of the density in the shock tube test are available at <http://fisica.upc.edu/ca/users/jjose/CRC-Downloads>.

**FIGURE 1.15**

Comparison between the numerical velocity profile at $t = 0.2$ units and the analytical solution in Sod's shock tube problem. A color version of this plot is available at <http://fisica.upc.edu/ca/users/jjose/CRC-Downloads>.

since $u_{\text{III}} = u_{\text{IV}}$ and $P_{\text{III}} = P_{\text{IV}}$, P_{III} can be determined numerically by imposing $u_{\text{II}} = u_{\text{IV}}$:

$$(P_{\text{III}} - P_{\text{V}}) \sqrt{\frac{1 - \omega^2}{\rho_{\text{V}}(P_{\text{III}} + \omega^2 P_{\text{V}})}} = (P_{\text{I}}^\psi - P_{\text{III}}^\psi) \sqrt{\frac{P_{\text{I}}^{1/\gamma} (1 - \omega^4)}{\rho_{\text{I}} \omega^4}}. \quad (1.174)$$

Once P_{III} (P_{IV}) is found, u_{III} (u_{IV}) can be determined from Equation 1.172.

The density and pressure ratios across the shock (i.e., at the boundary between regions IV and V) are given by the Rankine–Hugoniot conditions:

$$\frac{\rho_{\text{IV}}}{\rho_{\text{V}}} = \frac{P_{\text{IV}} + \omega^2 P_{\text{V}}}{P_{\text{V}} + \omega^2 P_{\text{IV}}}, \quad (1.175)$$

with $\omega^2 = (\gamma - 1)/(\gamma + 1)$. This yields the value of ρ_{IV} .

Regions I, II, and III have not been perturbed by the shock wave, and therefore are characterized by the same equation of state. Accordingly,

$$\rho_{\text{III}} = \rho_{\text{I}} \left(\frac{P_{\text{III}}}{P_{\text{I}}} \right)^{1/\gamma}, \quad (1.176)$$

which yields ρ_{III} .

Finally, the physical conditions in the x -dependent region II are given by (see reference [741]):

$$u_{\text{II}}(x, t) = (1 - \omega^2) \left(\frac{x - x_{\text{o}}}{t} + c_{\text{s,I}} \right) \quad (1.177)$$

and

$$\rho_{\text{II}}(x, t) = \left(\frac{\rho_{\text{I}}^\gamma}{\gamma P_{\text{I}}} \left[u_{\text{II}}(x, t) - \frac{x - x_{\text{o}}}{t} \right]^2 \right)^{1/\gamma-1}, \quad (1.178)$$

where $c_{s,I} = \sqrt{\gamma P_I / \rho_I}$ is the speed of sound in region I. Note that the location of the head and tail of the rarefaction wave as a function of time are simply given by:

$$x_{\text{head}}(t) = x_o - c_{s,I} t \quad (1.179)$$

and

$$x_{\text{tail}}(t) = x_o + (u_{\text{III}} - c_{s,\text{III}}) t, \quad (1.180)$$

where $c_{s,\text{III}}$ is the speed of sound in region III.

The time evolution of the system, solved numerically, is depicted in Figures 1.14 and 1.15. Calculations have been performed with the multidimensional code FLASH. To this end, two ideal fluids, characterized by a polytropic equation of state, $P = K\rho^\gamma$, with an adiabatic index corresponding to a diatomic molecular gas, $\gamma = 7/5$, are placed inside of a 1 unit-long tube, and separated by a planar interface located at $x_o = 0.5$ units. The initial conditions of the fluids are $\rho_I = 1$ and $P_I = 1$ units at the left-hand side of the interface, and $\rho_V = 0.125$ and $P_V = 0.1$ at the right-hand side. Once the interface is removed, the presence of a sharp discontinuity induces a shock that propagates to the right, into the undisturbed, low-density and low-pressure fluid. Simultaneously, a contact discontinuity drifts to the right, while a rarefaction wave propagates to the left.

The simulation, performed with a minimum resolution of 0.00056 units, shows excellent agreement with the analytical solution. In particular, it keeps the fluid discontinuities sharp, particularly when special techniques (e.g., adaptive mesh refinement⁴²) are implemented to invest more resolution in the regions of the computational grid, where physical variables exhibit the largest variations.

It is worth noting that Sod's shock tube test⁴³ (and any test, in general) only checks a few specific features of a code (e.g., its ability to handle shocks), and, therefore, only a handful of subroutines are effectively tested and verified.

1.7.1.2 Emery's Wind Tunnel Test

Another problem aimed at testing the performance of a hydrodynamic code is the *wind tunnel test with a step*, first described by Ashley Emery [495]. Specifically, the test checks the code's ability to handle multiple shock interactions in a multidimensional framework, particularly with irregular computational boundaries. The problem, however, has no analytical solution, and the performance of a specific code has to be tested by comparison with previously reported simulations of the same problem (e.g., references [567, 1958]).

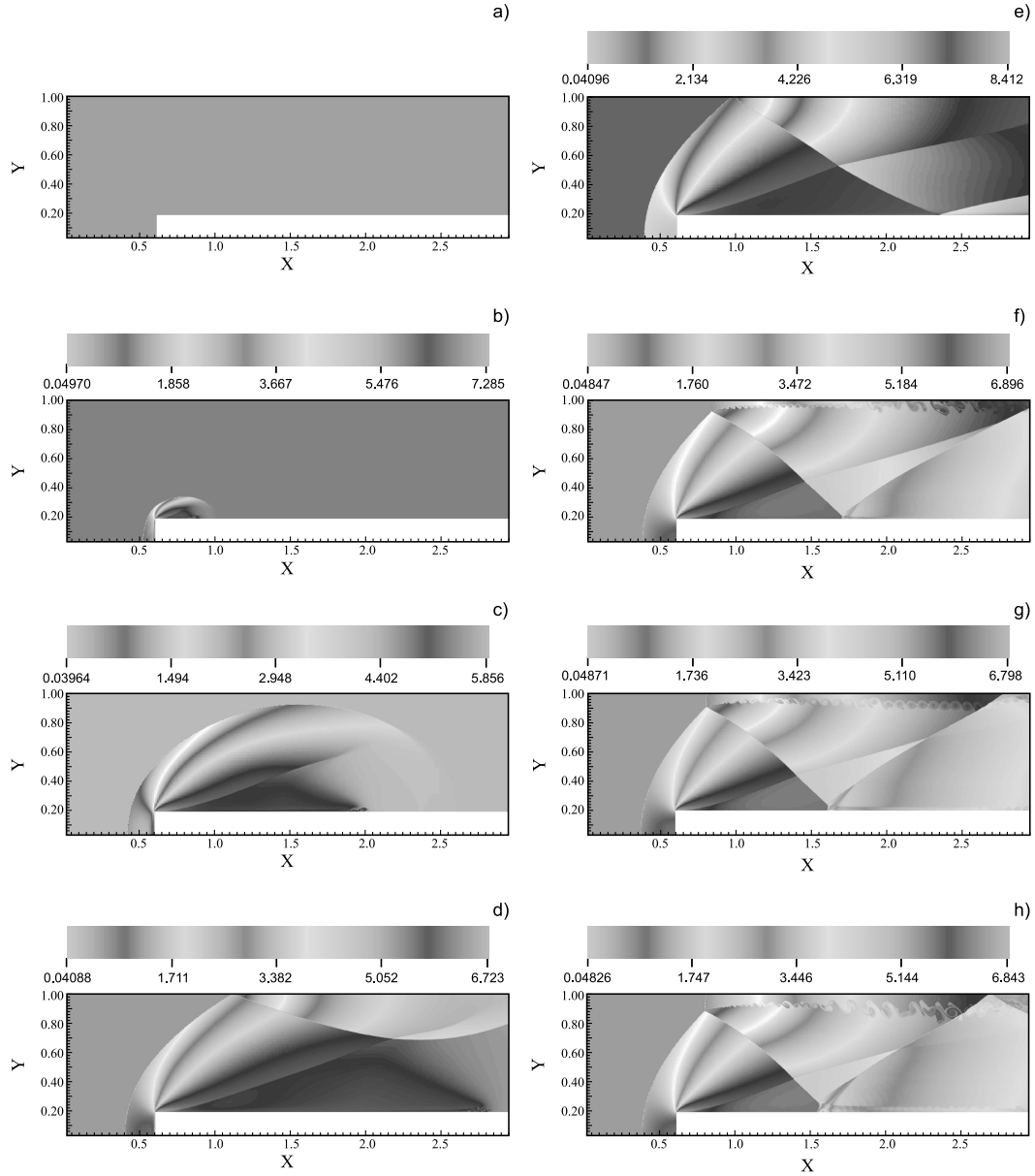
Figure 1.16 displays the response of the FLASH code to Emery's wind tunnel test. The simulation relies on a 2-dimensional, rectangular domain, with a dimensionless area of 3×1 , containing a 0.2 units high and 2.4 units wide step. The resolution adopted is 0.0016. A horizontal wind, with a dimensionless velocity of 3, is imposed on the left-hand wall. The fluid embedded in the domain is set to a pressure $P_o = 1$ and a density $\rho_o = 1.4$ ($\gamma = 1.4$), such that the local speed of sound yields a value of

$$c_s = \sqrt{\frac{\gamma P_o}{\rho_o}} = 1, \quad (1.181)$$

and hence, the wind corresponds to a supersonic, Mach 3 flow.

⁴²See references [156, 157, 282, 1141, 1174] for an introduction to adaptive mesh refinement techniques in computational hydrodynamics.

⁴³A variety of Sod's test, the *strong shock tube problem*, relies on larger pressure and density contrasts between both fluids (e.g. $P_I/P_V = 100$ and $\rho_I/\rho_V = 10$, a factor of 10 larger than in the standard Sod's test) [567, 741, 742]. This test is used to check the performance of a code in handling much stronger discontinuities and narrower density peaks, and hence becomes a much more demanding test than Sod's.

**FIGURE 1.16**

Evolution of the density field in Emery's wind tunnel test, at times 0 (panel a), 0.1 (b), 0.5 (c), 0.8 (d), 1.3 (e), 2.6 (f), 3.3 (g), and 4 (h). See text for details. Color plots and a movie portraying the time-evolution of the density in Emery's wind tunnel test are available at <http://fisica.upc.edu/ca/users/jjose/CRC-Downloads>.

A shock wave develops in front of the step ($t \sim 0.1$), curving progressively around the step's corner and growing in size until it eventually hits the upper boundary of the computational domain ($t \sim 0.7$), where reflecting boundary conditions have been imposed. Indeed, the step's corner acts as a “rarefaction fan”, connecting the unperturbed gas located above the step and the shocked gas in front of it [567]. A numerical boundary layer is formed

all along the surface of the step, which translates into a small overexpansion of the gas and a weak shock, generated when the gas falls back onto the step. The first reflected wave experiences additional reflections when colliding, back and forth, with the surface of the step (at $t = 1.2$) and with the upper boundary ($t = 3.3$). The merging of the primary and the first reflected shock waves gives rise to a so-called *Mach stem* at about $t = 1.8$. At $t = 3$, a second, spurious Mach stem seems to develop at the second reflection point, on the surface of the step, but this feature disappears in higher resolution runs [567]. The shear zone behind the upper Mach stem gives rise to Kelvin–Helmholtz instabilities, clearly visible in the fluid at $t > 2$, likely originated by the amplification of numerical errors produced at the shock intersection. This stresses the need of an in-depth analysis when interpreting numerical results [567]. Indeed, simulations should be ideally repeated at different levels of refinement in order to assess whether a specific feature is spurious (e.g., driven by noise amplification) or real [1958].

1.7.1.3 Sedov's Blast Wave Problem

The *Sedov blast wave test* checks a code's ability to handle strong shocks in nonplanar symmetry. The test follows the evolution of a cylindrical or spherical blast wave driven by the deposition of an instantaneous amount of energy in a small area of an otherwise homogeneous medium. The problem attracted the interest of several physicists during World War II, when nuclear weapons became feasible. L. I. Sedov and J. von Neumann [1602, 1869] (see also reference [1048]), independently derived an analytical solution⁴⁴ to the problem of a blast wave propagating into a cold gas.

The relevant magnitudes for the dynamics of the explosion are the energy released, E ; the density of the unperturbed gas, ρ_0 ; and the time since the explosion, t . Dimensional analysis yields the following dependences:

$$[E] = ML^2T^{-2} \quad (1.182)$$

$$[\rho] = ML^{-3}. \quad (1.183)$$

To get rid of the mass, not considered a relevant magnitude in this problem, one can simply write

$$\left[\frac{E}{\rho} \right] = L^5T^{-2} \rightarrow \left[\frac{E}{\rho} \right]^{1/5} = LT^{-2/5}, \quad (1.184)$$

which conveniently multiplied by $t^{2/5}$ yields

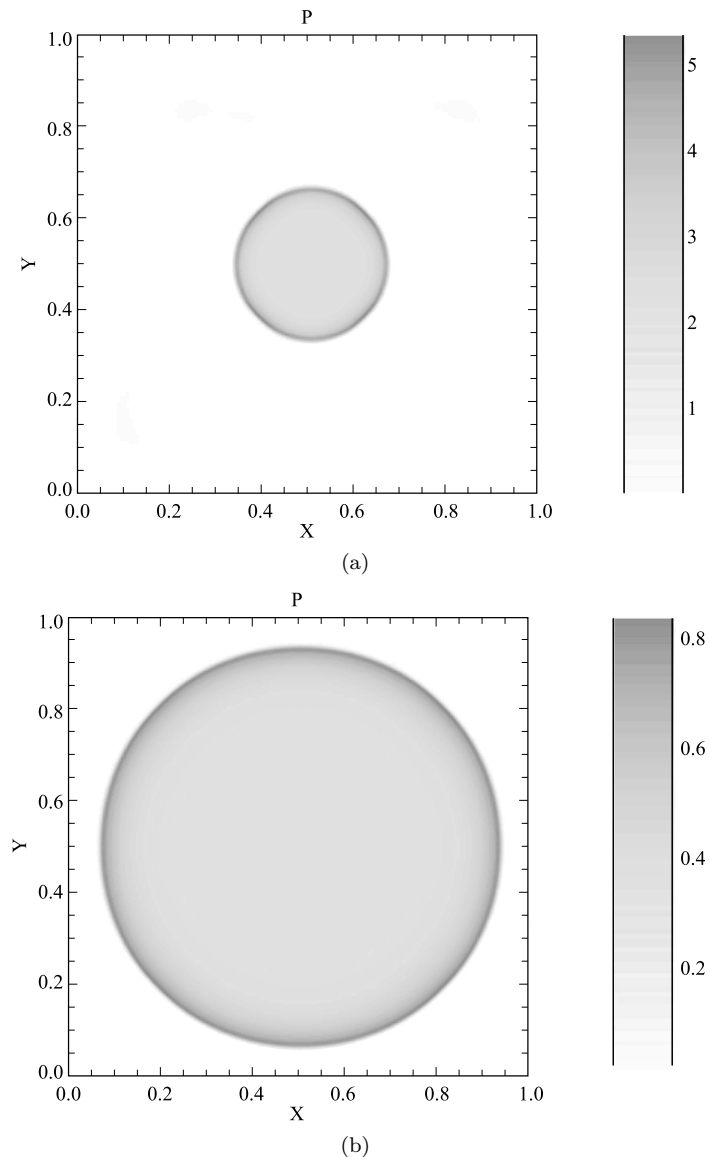
$$R(t) = k \left(\frac{E}{\rho} \right)^{1/5} t^{2/5}. \quad (1.185)$$

Equation 1.185 defines the characteristic length-scale of the expanding blast wave or *fireball*⁴⁵, with k a normalization constant of the order of unity.

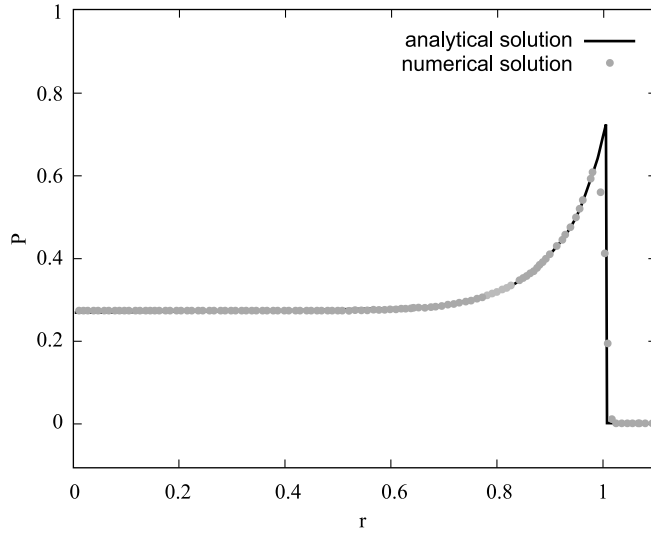
The three partial differential equations governing the evolution of the system (i.e., mass, momentum, and energy conservation) can be transformed into a set of ordinary differential

⁴⁴The backbone of the Sedov blast wave theory, the similarity relations, was also derived by G. I. Taylor in the 1940s [1783, 1784]. Using a series of snapshots of the Trinity explosion, Taylor tested his scaling hypothesis and calculated the energy of the blast (see Problem P8 at the end of this chapter).

⁴⁵Arguments based on the energetics of the explosion yield the same scaling law: The mass of swept-up gas after a time t , when the fireball has expanded to a size R , is given by $m(t) \sim \rho_0 R^3$. The postshocked material velocity, immediately behind the shock, is of the order of the speed of the shock front, $u \sim R/t$. Therefore, the kinetic energy of the swept-up gas can be estimated as $\sim \rho_0 R^3 u^2 \sim \rho_0 R^5/t^2$. A similar expression can be obtained for the internal energy of the postshocked fluid. All in all, a scaling law $R = k(E/\rho_0)^{1/5}t^{2/5}$ can be inferred.

**FIGURE 1.17**

Snapshots of the pressure at (a) $t = 0.03$ and (b) 0.21 units, in Sedov's blast wave problem, showing that the spherical symmetry of the blast wave is preserved as the detonation sweeps the computational domain. Color plots and a movie portraying the time-evolution of the pressure in Sedov's blast wave test are available at <http://fisica.upc.edu/ca/users/jjose/CRC-Downloads>.

**FIGURE 1.18**

Comparison between the analytical pressure and the numerical value at $t = 0.27$ units, in Sedov's blast wave problem. A color version of this plot is available at <http://fisica.upc.edu/ca/users/jjose/CRC-Downloads>.

equations with analytical solution by considering that the time-evolution of the sphere is independent of the details of the initial expansion. That is, the shape of the radial profiles of pressure, density, and velocity are assumed to be time-independent (i.e., a similarity solution). Once the characteristic length-scale of the explosion is identified with the radius of the blast wave, $R(t)$, the thermodynamic variables of the system can be expressed as functions of the dimensionless variable

$$\xi = \frac{r}{R(t)}. \quad (1.186)$$

Assuming strong shock jump conditions⁴⁶, thus neglecting the preshock pressure, one can get the postshocked values of u , ρ , and P immediately behind the shock (i.e., at $\xi = 1$):

$$u = \frac{2}{\gamma + 1} u_{\text{sw}} \quad (1.187)$$

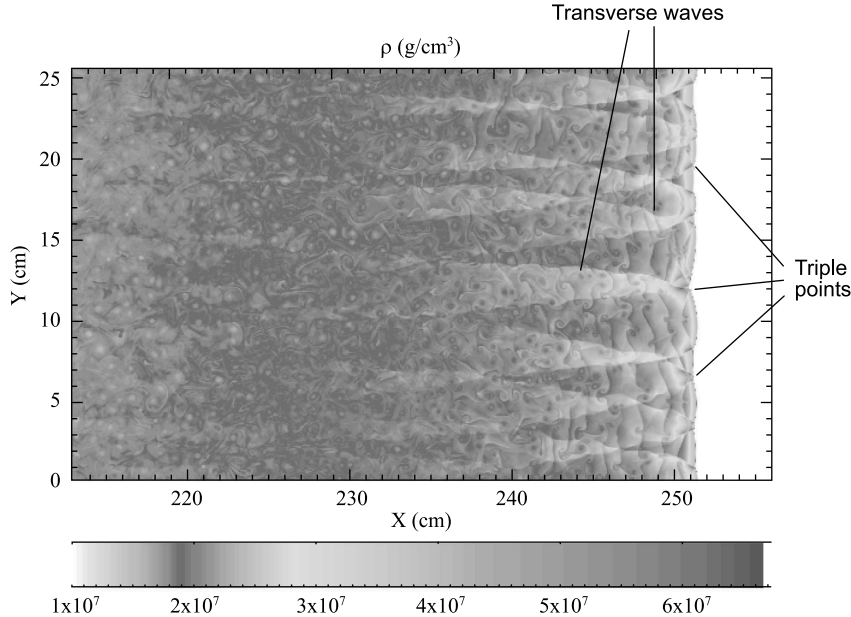
$$\rho = \rho_o \frac{\gamma + 1}{\gamma - 1} \quad (1.188)$$

$$P = \rho_o u_{\text{sw}}^2 \frac{2}{\gamma + 1}, \quad (1.189)$$

where ρ_o is the immediate preshock density and $u_{\text{sw}} \equiv dR(t)/dt \sim (2/5)(E/\rho_o)^{1/5}t^{-3/5}$ is the speed of the shock wave.

The Sedov's blast wave problem has also been tested with the FLASH code, assuming an ideal-gas fluid (with $\gamma = 1.4$) at rest in a square, two-dimensional computational domain of 1×1 . The resolution adopted was 0.0039 in both coordinates. The initial dimensionless density was set to 1, while the adopted dimensionless pressure was 10^{-5} . A dimensionless

⁴⁶This assumption limits the applicability of the formulae derived up to the time when the shock moves at \sim Mach 1, and therefore, the hypothesis of a strong shock no longer holds.

**FIGURE 1.19**

Snapshot of the density field at $t = 185$ ns, in the cellular problem. Incident shock waves, triple points, and transverse waves can be identified, with a postshock structure extending about 20 cm behind the front. A color plot and a movie portraying the time-evolution of the density in the cellular problem are available at <http://fisica.upc.edu/ca/users/jjose/CRC-Downloads>.

energy $E = 0.85$ was deposited in a small region of radius $\delta r \sim 0.014$, centered in the domain. Following Fryxell and collaborators [567], the pressure inside this tiny volume is given by

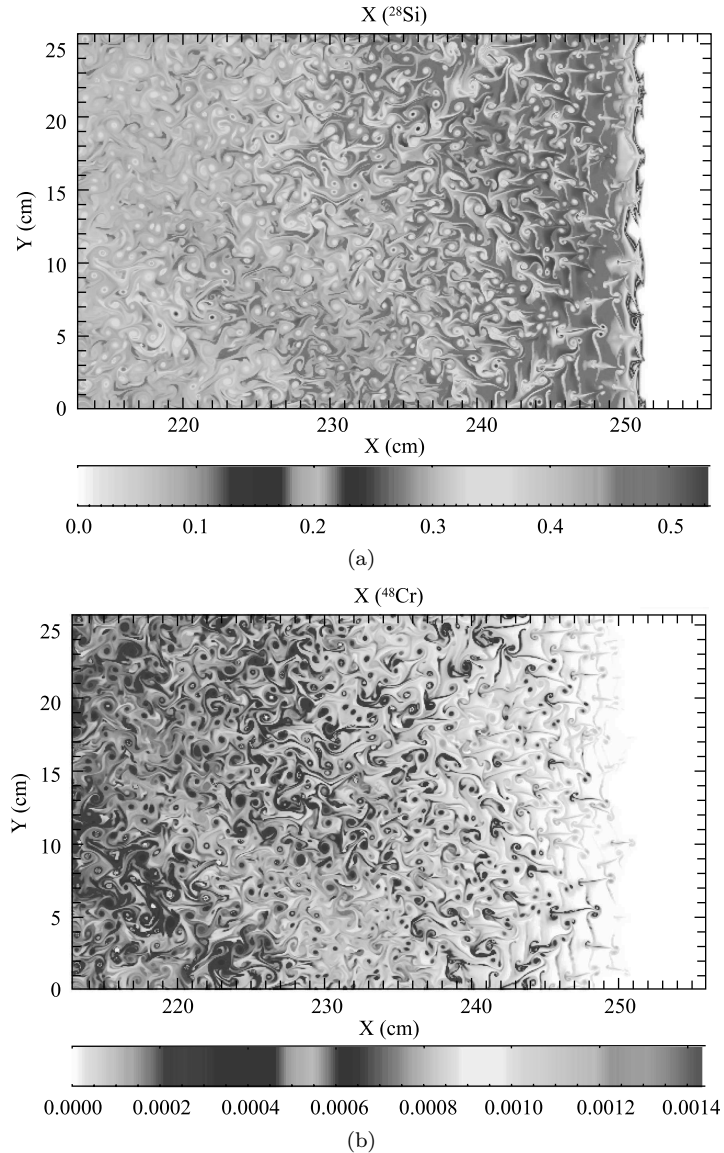
$$\delta P = \frac{3(\gamma - 1)\epsilon}{(\nu + 1)\pi\delta r^\nu}, \quad (1.190)$$

with $\nu = 3$ for a spherical geometry. Snapshots of the evolution of the system, at $t = 0.03$ and $t = 0.21$ units, are shown in Figure 1.17.

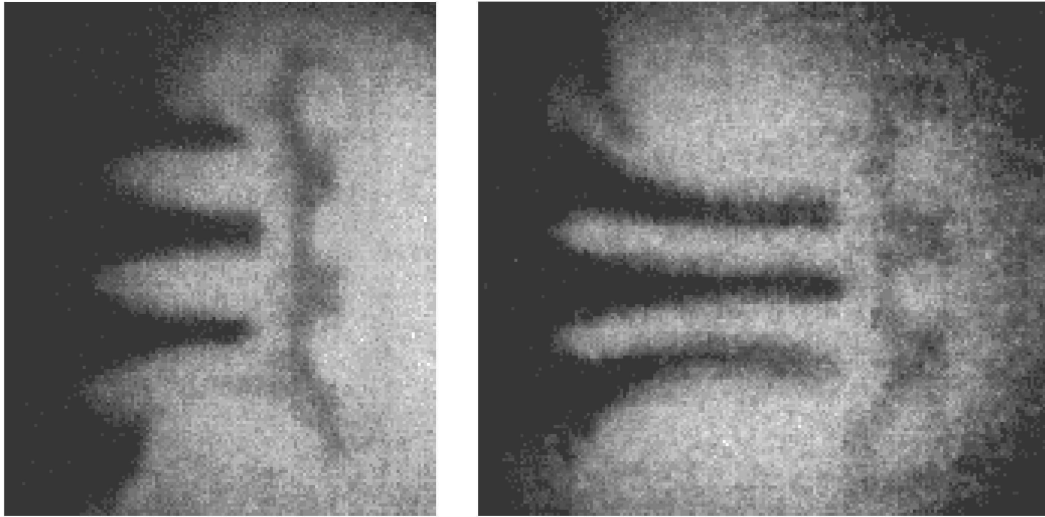
The simulation is stopped at $t = 0.21$, when the explosion hits the boundaries of the computational domain. A comparison between the numerical results and the analytical solution (Figure 1.18) reveals that the simulation qualitatively reproduces the analytical solution, but the shock discontinuity is not well resolved. Indeed, the pressure peak, for instance, is reduced by 13% with respect to the analytical solution. The same pattern applies to the density peak, which exhibits a reduction by 20%. The velocity peak, instead, is just 4% below the analytical value. Better agreement between the numerical results and the analytical solution can be obtained with higher resolution runs.

1.7.1.4 Cellular Test

Another test, specifically suited for stellar explosion codes—type Ia supernovae, in particular—is the *cellular problem*. The test explores the performance of a code in handling detonations under extreme physical conditions [216, 601, 1809], allowing the analysis of detonation structures in a multidimensional framework, which lie beyond current detonation theory [1940].

**FIGURE 1.20**

Distribution of ^{28}Si and ^{48}Cr in mass fractions at $t = 185$ ns in the cellular problem, showing the onset of Kelvin–Helmholtz instabilities. Note that while ^{28}Si increases from left to right, the abundance of ^{48}Cr decreases from left to right. Color plots and movies portraying the time-evolution of the abundances of ^{28}Si and ^{48}Cr in the cellular problem are available at <http://fisica.upc.edu/ca/users/jjose/CRC-Downloads>.

**FIGURE 1.21**

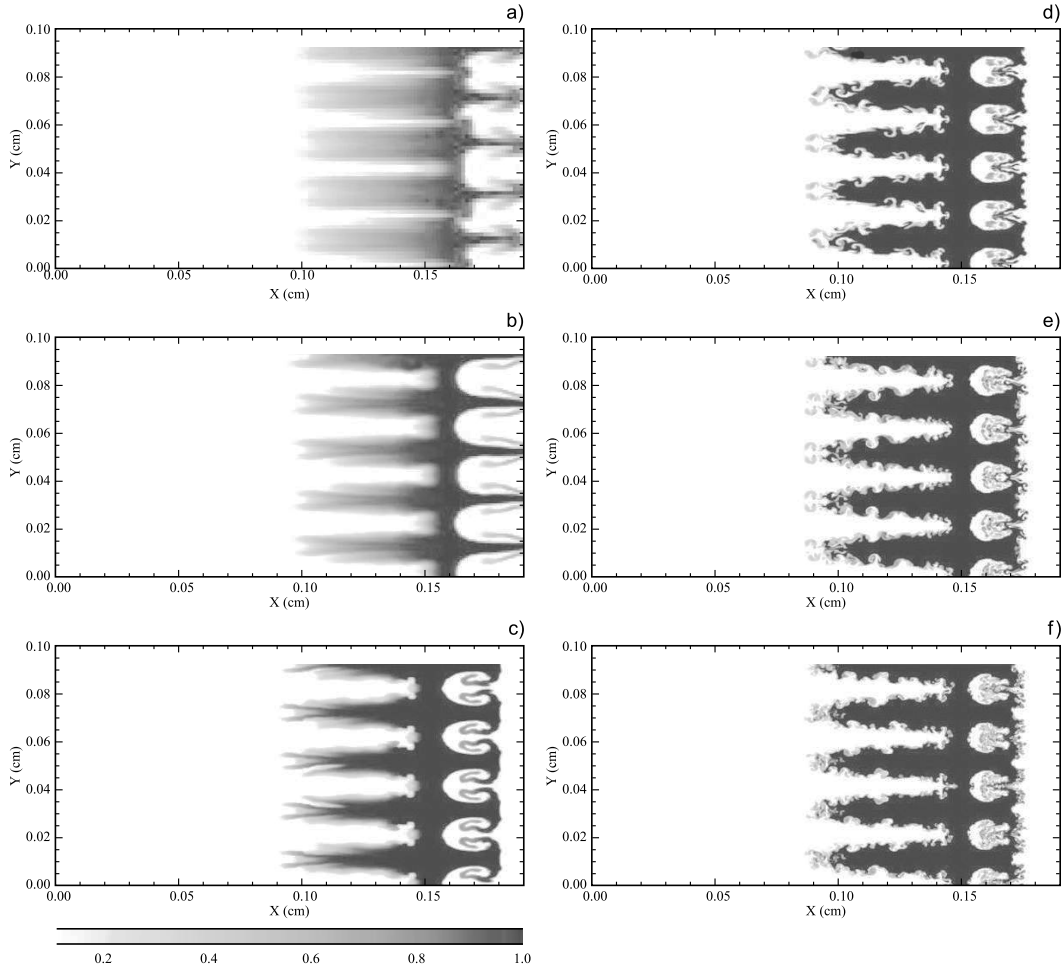
X-ray radiographs taken at 39.9 ns (left panel) and 66.0 ns (right panel) in a laser-driven shock experiment. The shock propagates through layers of decreasing density, made of Cu, polyimide plastic (with an embedded strip of a brominated hydrocarbon), and a carbonized resorcinol formaldehyde (CRF) foam, driving the development and growth of Richtmyer–Meshkov instabilities (see text for details). Figure from A. Calder, B. Fryxell, T. Plewa, and collaborators [282], reproduced with permission.

The test consists of a pure ^{12}C plasma, at $T_0 = 2 \times 10^8$ K and $\rho_0 = 10^7$ g cm $^{-3}$, initially at rest. The fluid is encapsulated in a tiny two-dimensional, computational domain of 256×25.6 cm 2 . The evolution of the system has been followed with the FLASH code, as in previous tests, with a resolution of 0.025 cm.

The region $x < 25.6$ cm is perturbed by artificially increasing the initial temperature to 4.4×10^9 K and the density to 4.2×10^7 g cm $^{-3}$. The velocity of this postshocked material is fixed at 2.9×10^8 cm s $^{-1}$. As a result, a detonation moving forward to the right is born. When $t = 45$ ns, density perturbations show up, transforming the initial, planar detonation into a complex cellular structure, with incident shocks moving forward, triple points⁴⁷, and transverse shock waves (generated at the triple points) moving backward. The interaction between backward and forward shock waves yields, in turn, the formation of new triple points (see Figure 1.19).

The rich nucleosynthesis accompanying this complex detonation structure is characterized by a fast ^{12}C consumption, accompanied by the synthesis of a number of intermediate-mass species. Figure 1.20 depicts the distribution of two species, ^{28}Si and ^{48}Cr , at $t = 185$ ns, when Kelvin–Helmholtz hydrodynamic instabilities are clearly appreciated. All in all, the test has proved the FLASH code performance in handling complex hydrodynamical structures, such as Kelvin–Helmholtz instabilities, under challenging physical conditions that require extremely small timesteps (i.e., $\Delta t \sim 9 \times 10^{-12}$ s).

⁴⁷Triple points appear in steady and unsteady flows when shocks interfere in the presence of a wall. At a triple point three shocks intersect: the incident shock, a reflected shock, and a Mach stem [761].

**FIGURE 1.22**

Plots based on laser-driven shock simulations depicting the onset of Richtmyer–Meshkov instabilities in a CH abundance map at 66.0 ns. Spatial resolution increases from panels a to f. Figure from A. Calder, B. Fryxell, T. Plewa, and collaborators [282], reproduced with permission.

1.7.2 Validation Tests

One of the active research areas in the emerging field of laboratory astrophysics is the analysis of astrophysical hydrodynamic problems through laboratory experiments. Astrophysical objects are obviously characterized by much larger scales than laboratory systems. Therefore, any laboratory experiment aimed at addressing a specific astrophysical phenomenon must be able to be extrapolated with the aid of a good scaling model. In this regard, numerical simulations seem better suited than experiments to tackle astrophysical plasmas, but they face the impossibility to reach the extremely small scales required by microphysics.

A number of experiments have been conducted in the lab to address specific phenomena produced in astrophysical plasmas during supernova explosions (see references [466,1486] for reviews). Among others: unmagnetized expansion experiments with the Helios laser system at Los Alamos National Laboratory, aimed at characterizing the dynamics of supernova

remnants [220,1773]; blast-wave deceleration experiments at the KI-1 facility at Novosibirsk (Russia), aimed at simulating the deceleration of the blast wave in supernova remnants [53, 93, 1352]; blast-wave instability experiments conducted at the Naval Research Laboratory, designed to study the formation of instabilities driven by reverse shocks in young supernova remnants [690]; contact-surface hydrodynamic experiments aimed at addressing the local, hydrodynamic evolution of supernova remnants at the Nova laser facility of the Lawrence Livermore National Laboratory [467,468]; fuel burning experiments aimed at understanding the physics of deflagration-to-detonation transitions in type Ia supernovae (see Chapter 5) [981,982,1626]; and interface instability experiments with the Nova laser, aimed at testing the role played by several hydrodynamic instabilities during core-collapse supernovae (see Chapter 7) [942,943,1483–1485].

Hereafter, we will briefly focus on some experiments conducted with high-energy-density lasers, aimed at testing the performance of the FLASH code, as an example of the difficulties faced in validation assessments. Figure 1.21 shows two X-ray radiographs taken at 39.9 ns and 66.0 ns in an experiment with laser-driven shocks conducted at the Omega laser facility (Laboratory for Laser Energetics, University of Rochester, New York). Shock waves propagate through a multilayered target of decreasing density, made of Cu, polyimide plastic (with an embedded strip of a brominated hydrocarbon), and a carbonized resorcinol formaldehyde (CRF) foam, generating Rayleigh–Taylor and Richtmyer–Meshkov instabilities (see Section 1.3.2) [283,447,753,944]. The long, dark fingers of the images are actually spikes of expanding Cu, while the horizontal band to the right of the spikes corresponds to the brominated plastic showing how the instabilities grow at the plastic-foam interface. The validation experiment revealed an observed pattern qualitatively in agreement with the results of the numerical simulations performed with the FLASH code and reproduced in Figure 1.22. Unfortunately, a thorough comparison between simulation and experiment is frequently hampered by the experimental diagnostic resolution [1917]. Imaging of the evolution of the driven instabilities through face-on or side-on X-ray radiography turns out to be challenging. Moreover, while the experiment confirmed that the code under scrutiny can actually reproduce the main observational properties of the flow and the resolvable morphology, higher-resolution runs revealed a degradation in the agreement between simulations and experiments. Indeed, the increase of resolution translates into the development of small-scale structures that affect the long-term evolution of larger structures, such as the spikes. This likely reveals the lack of key physics modules that, while irrelevant in the astrophysical scenarios of interest, turn out to be essential for a perfect match with terrestrial experiments. This stresses the need (as well as the challenge) to find out the appropriate experiments that can successfully lead to the validation of a numerical code under the same physical conditions in which it will be used.

Box I. The Computational Hydrodynamics “Hall of Fame”

A selection of facts on numerical modeling and hydrodynamic codes

1. Stellar codes rely on a set of conservation equations (mass, momentum, and energy), energy sources, and energy transport mechanisms (radiation, conduction, and convection).
2. The most extensively used form of discretization in stellar evolution codes of the original set of coupled, partial differential equations into a system of algebraic equations that could be solved numerically are finite differences. Other methods, such as finite elements or finite volumes, are frequently used in other areas of computational fluid dynamics.
3. Different numerical tools have been used to date in the modeling of stellar explosions and their associated nucleosynthesis, ranging from one-zone to multi-dimensional models. State-of-the-art nucleosynthesis in novae and X-ray bursts relies mostly on 1D, spherically symmetric, hydrodynamic models, while nucleosynthesis in (types Ia and II) supernovae and stellar mergers requires a postprocessing approach based on temperature and density versus time profiles.
4. Traditional Lagrangian methods, with a computational grid attached to the fluid, constitute the simplest choice for building a hydrodynamic code, in the context of nonturbulent fluids. Eulerian methods, with a grid fixed in space, provide a good alternative to Lagrangian methods in the framework of turbulent fluids, because of the lack of grid distortion. While the vast majority of 1D hydro codes are Lagrangian, grid-based multidimensional codes mostly rely on an Eulerian formulation.
5. Gridless or meshfree methods, such as smoothed-particle hydrodynamics, provide a suitable alternative to avoid mesh tangling and distortion, frequently encountered in traditional grid-based methods in the presence of nonlinear behavior, discontinuities, or singularities.
6. The dawn of supercomputing has provided theoreticians with the appropriate arena in which truly multidimensional processes can be tested. The last decades had witnessed a number of multidimensional models of stellar explosions, with increasing levels of resolution.
7. The degree in which a numerical solution represents the true solution of a problem requires efforts aimed at verifying and validating each code’s capabilities. A suite of classical tests (e.g., Sod’s shock tube, Sedov’s blast wave) is frequently used in the verification stage of hydrodynamic codes. Laboratory experiments (e.g., laser-driven shocks) offer an appealing but challenging path for validation.

Box II. Mysteries, Unsolved Problems, and Challenges

- 1D, stellar evolution codes face severe limitations in the treatment of convection, a key mechanism for energy transport in stars. Convection is a truly multidimensional process that is, however, implemented through phenomenological approaches—frequently, the mixing-length theory—due to inherent uncertainties and complexity. New prescriptions based on multidimensional models are needed for further implementation in 1D codes, particularly in the framework of stellar explosions, such as novae or X-ray bursts.
- Some stellar evolution codes are still constructed, for simplicity, as nonrotating and nonmagnetic. In contrast, stars obviously rotate and a number of relevant magnetic effects frequently accompany stellar plasmas. Efforts to include rotation and magnetic fields in current stellar hydro codes are highly advisable.
- A number of implicit and semiimplicit schemes have been proposed to tackle the stiff differential equations that govern the time evolution of the abundances in a stellar plasma. While in the past most hydro codes relied on Wagoner's two-step linearization technique, other schemes like Bader–Deuflhard's or Gear's backward differentiation proved far more accurate and fast. Since nuclear reactions often constitute the time-limiting factor, at least in most 1D codes, it would be advisable to rely on faster reaction network integration schemes.
- Most multidimensional codes implemented to date are explicit, with a time-step limited by the Courant–Friedrichs–Levy condition. Fully implicit multidimensional codes are needed to address full cycles of stellar explosions, from the long, quiet accretion stages—unaffordable with explicit schemes—to the truly dynamic stages of the event.
- ALE codes are still not widely used in astrophysical hydrodynamics. They reduce the shortcomings of purely Lagrangian or Eulerian codes by combining the best features of both formulations. Multidimensional ALE codes are particularly well suited to simultaneously address mixing and convection (which result in undesired mesh tangling and distortion in Lagrangian schemes), as well as the dynamic explosion and ejection stages (which cannot be easily followed with an Eulerian scheme).
- Nucleosynthesis accompanying stellar explosions mostly relies on 1D hydrodynamic models or on postprocessing techniques. To date, multidimensional models frequently implement reduced nuclear reaction networks, containing only a handful of isotopes to approximately account for the energetics of the explosion.
- Special efforts must be devoted to develop and implement new ways to tackle the vast range of relevant length scales that characterize most stellar explosions, which are currently impossible to resolve. In this regard, the advances made in type Ia supernova modeling (e.g., level-set techniques [1354, 1518, 1525]) should also be applied to models of classical novae and X-ray bursts.

1.8 Exercises

P1. A strong shock wave, propagating at a supersonic speed, separates two regions of a fluid. Prove that a fluid characterized by a polytropic equation of state, $P = K\rho^\gamma$, satisfies the following relations:

$$\frac{P_2}{P_1} = \frac{2\gamma Ma_1^2 - (\gamma - 1)}{\gamma + 1}$$

$$\frac{\rho_2}{\rho_1} = \frac{u_2}{u_1} = \frac{\gamma + 1}{(\gamma - 1) + 2/Ma_1^2},$$

where subscript 1 refers to the unperturbed fluid, subscript 2 to the postshocked fluid, and $Ma_1 = u_1/c_{s,1}$ is the Mach number in the unperturbed fluid.

Show also that in the limit of very strong shocks, $Ma_1 \gg 1$:

$$\frac{P_2}{P_1} = \frac{2\gamma Ma_1^2}{\gamma + 1}$$

$$\frac{\rho_2}{\rho_1} = \frac{\gamma + 1}{\gamma - 1}.$$

P2. Derive the analytical solution of the free-fall collapse problem (i.e., Equation 1.170).

P3. Use program `freefall.f` (Appendix B) and compute the free-fall collapse of a homogeneous sphere, for the same initial conditions described in Section 1.6.7 but different choices of β (i.e., 0, 0.25, 0.5, 0.75, 1). Compare the results obtained with the corresponding analytical solution.

P4. A variable $y(t)$ varies according to the equation

$$\frac{dy}{dt} = Cy, \quad (1.191)$$

where C is a constant.

- a) Solve the differential equation exactly. Determine y for $t \rightarrow \infty$ and $C < 0$.
- b) Solve the differential equation numerically, using Euler's method (the simplest numerical scheme, corresponding to a first-order Taylor expansion):

$$y(t + \Delta t) = y(t) + \frac{dy}{dt} \Delta t. \quad (1.192)$$

c) Compare qualitatively the exact and the numerical solution for $C > 0$, $-1 < \Delta t C < 0$, and $-2 < \Delta t C < -1$.

d) Solve the differential equation using a second-order Runge–Kutta scheme:

$$y(t + \Delta t) = y(t) + \Delta t F \left[t + \frac{\Delta t}{2}, y(t) + \frac{\Delta t}{2} F(t, y(t)) \right], \quad (1.193)$$

with $F \equiv dy/dt$.

P5. A simple method to assess the stability of a numerical scheme (that is, a way to determine the robustness of a scheme when small perturbations are introduced in an equation)

was derived by John von Neumann at Los Alamos National Lab around 1944 (see reference [153]). Let's consider the (hyperbolic) partial differential equation:

$$\frac{\partial u}{\partial t} = -v \frac{\partial u}{\partial x} \quad (1.194)$$

whose solution has the form $u(x, t) = f(x - vt)$. A possible numerical scheme to approximate the equation (assuming $\Delta x = \text{constant}$ and $\Delta t = \text{constant}$) is given by

$$\frac{u_j^{n+1} - u_j^n}{\Delta t} = -v \frac{u_{j+1}^n - u_{j-1}^n}{2\Delta x}, \quad (1.195)$$

where superscripts n and $n + 1$ refer to times t^n and $t^{n+1} = t^n + \Delta t$, and subscripts $j - 1$, j , and $j + 1$ correspond to grid points $x_{j-1} = x_j - \Delta x$, x_j , and $x_{j+1} = x_j + \Delta x$.

a) Prove that the scheme is first-order accurate in time while second-order accurate in space.

The scheme can also be written as:

$$u_j^{n+1} = u_j^n - \frac{v\Delta t}{2\Delta x} (u_{j+1}^n - u_{j-1}^n). \quad (1.196)$$

In von Neumann's stability analysis, the solution is expanded in a finite Fourier series, in the form

$$u_j^n = A^n e^{ikjx}. \quad (1.197)$$

Plugging this expression into the numerical scheme (Equation 1.196) yields

$$A^{n+1} e^{ikjx} = A^n e^{ikjx} - \frac{v\Delta t}{2\Delta x} (A^n e^{ik(j+1)x} - A^n e^{ik(j-1)x}). \quad (1.198)$$

b) Show that the amplification factor from t^n to t^{n+1} is given by

$$A = 1 - i \frac{v\Delta t}{\Delta x} \sin(kx) \quad (1.199)$$

and prove that whenever $|A| > 1$ the scheme is unstable.

c) Consider a similar scheme in which u_j^n is replaced by an average between neighbors (i.e., Lax method):

$$u_j^{n+1} = \frac{u_{j+1}^n - u_{j-1}^n}{2} - \frac{v\Delta t}{2\Delta x} (u_{j+1}^n - u_{j-1}^n). \quad (1.200)$$

Show that the amplification factor is now given by

$$A = \cos(kx) - i \frac{v\Delta t}{\Delta x} \sin(kx) \quad (1.201)$$

and prove that $|A| \leq 1$ requires

$$\frac{|v| \Delta t}{\Delta x} \leq 1, \quad (1.202)$$

which is known as the Courant–Friedrichs–Levy (CFL) stability condition (i.e., the velocity at which information propagates within the algorithm, $\Delta x/\Delta t$, must be faster than the velocity of the solution, v).

P6. Consider the 1D diffusion equation (an example of parabolic equation), with a constant diffusion coefficient, D :

$$\frac{\partial u}{\partial t} = \frac{\partial}{\partial x} \left(D \frac{\partial u}{\partial x} \right) = D \frac{\partial^2 u}{\partial x^2}. \quad (1.203)$$

- a) Determine the performance of the following numerical scheme through von Neumann's stability analysis

$$\frac{u_j^{n+1} - u_j^n}{\Delta t} = D \frac{u_{j+1}^n - 2u_j^n + u_{j-1}^n}{(\Delta x)^2} \quad (1.204)$$

and prove that the method is stable only for small step sizes, Δx .

- b) Repeat the analysis for the alternative scheme (i.e., Crank–Nicolson)

$$\frac{u_j^{n+1} - u_j^n}{\Delta t} = \frac{D}{2} \frac{(u_{j+1}^{n+1} - 2u_j^{n+1} + u_{j-1}^{n+1}) + (u_{j+1}^n - 2u_j^n + u_{j-1}^n)}{(\Delta x)^2} \quad (1.205)$$

and determine the corresponding stability condition.

P7. The surface blackbody temperature of the Sun is 5780 K. Use Stefan's law to determine the Sun's rest mass lost per second and the fraction lost each century to radiation by the Sun.

P8. Consider the snapshots of the test explosion of the world's first atomic bomb (Trinity site, near Alamogordo, New Mexico, July 16, 1945) shown in Figure 1.23. Measure the radius of the spherical shock wave or *fireball*, for each shot.

- a) Plot the radius, r (m), as a function of time, t (s), in a logarithmic scale (i.e., $5/2 \log r$ vs. $\log t$) and prove that the data points can be fitted by a straight line.

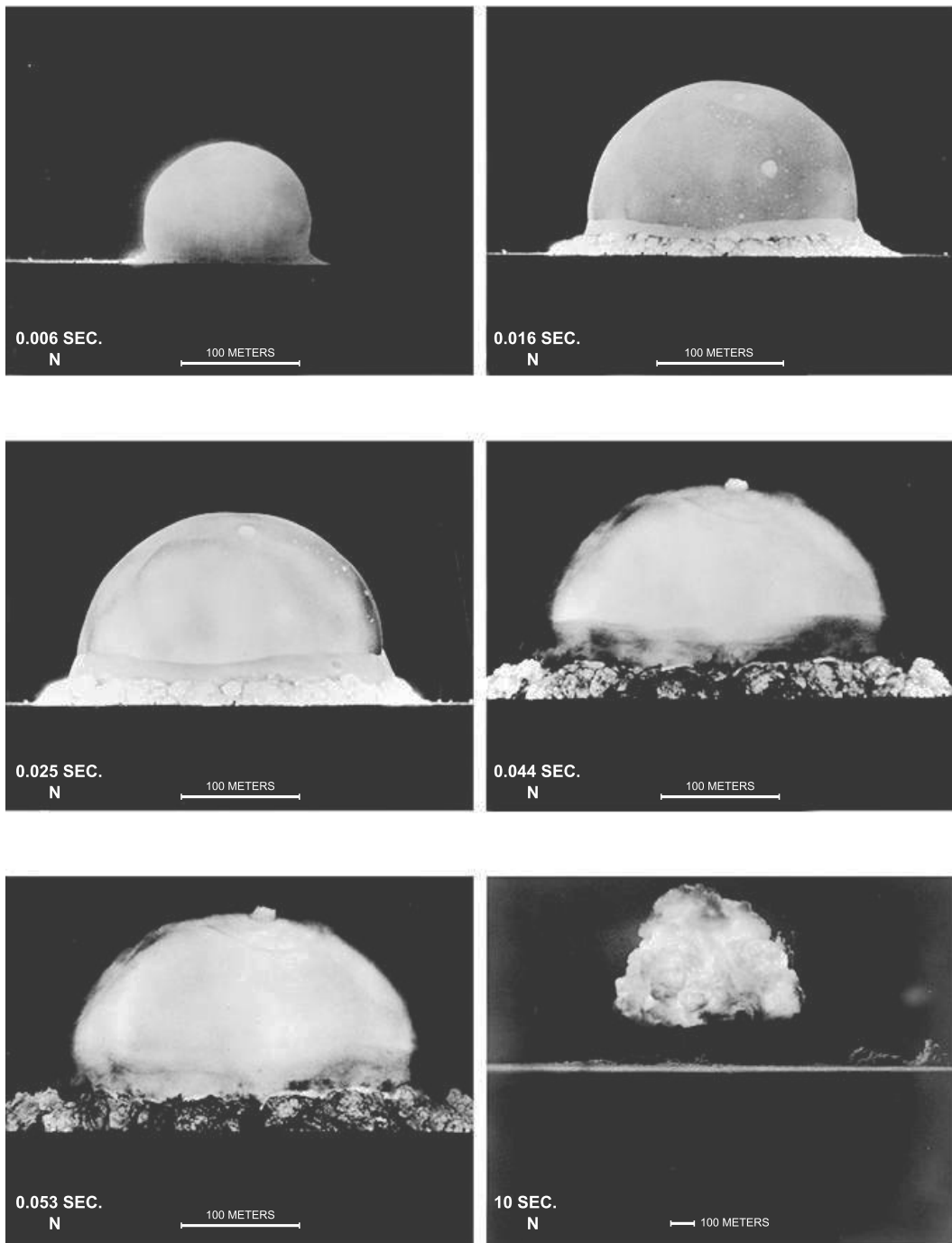
b) Assume that the time-evolution of the fireball follows a Sedov–Taylor explosion until $t \sim 100$ ms, and consider a density for the nonperturbed air surrounding the explosion of $\rho = 1.25 \text{ g cm}^{-3}$. Estimate the energy released by the explosion in kilotons [1784]. Compare the result with the on-site estimate performed by Enrico Fermi, ~ 10 kilotons, on the basis of the displacement of small pieces of paper, before, during, and after the passage of the blast wave, at about 10 miles from the explosion site⁴⁸.

- c) Consider the expansion of the Crab nebula, a supernova remnant (see Chapters 5 and 7). Rewrite Equation 1.185 in the convenient form

$$R(t) = 2.3 \text{ pc} \left(\frac{E}{10^{51} \text{ erg}} \right)^{1/5} \left(\frac{\rho_o}{10^{-24} \text{ g cm}^{-3}} \right)^{-1/5} \left(\frac{t}{100 \text{ yr}} \right)^{2/5}, \quad (1.206)$$

and assume that the energy released in a supernova explosion is about 10^{51} erg, the density of the interstellar medium swept by the supernova blast has a mean density of $10^{-24} \text{ g cm}^{-3}$, and the size of the Crab nebula is ~ 3 pc. Estimate the age of the supernova remnant and its expansion velocity.

⁴⁸For a detailed account, see *The Day the Sun Rose Twice* (1984) by F. M. Szasz [1757].

**FIGURE 1.23**

Snapshots of the test explosion of the world's first atomic bomb (Trinity site, near Alamogordo, New Mexico, July 16, 1945). Image courtesy of Los Alamos National Laboratory.

Appendix A

Henyey Method for Arbitrary Hydrodynamic Problems

A primer on spherically symmetric, hydrodynamic code development was presented in Chapter 1, in the framework of a simple problem: the free-fall collapse of a homogeneous sphere. This appendix extends the analysis to a general, 1D stellar evolution code. Let's start with the set of partial differential equations that describe a stellar plasma (i.e., conservation and transport equations; see Sections 1.2 and 1.4):

- Conservation of mass

$$\frac{1}{\rho} = \frac{4}{3}\pi \frac{\partial r^3}{\partial m}. \quad (\text{A.1})$$

- Conservation of momentum

$$\frac{\partial u}{\partial t} + 4\pi r^2 \frac{\partial(P+q)}{\partial m} = -G \frac{m}{r^2}. \quad (\text{A.2})$$

- Conservation of energy

$$\frac{\partial E}{\partial t} = \varepsilon - \frac{\partial L}{\partial m} + \frac{P+q}{\rho^2} \frac{\partial \rho}{\partial t}. \quad (\text{A.3})$$

- Energy transport (by radiation and convection)

$$L = -256\sigma\pi^2 r^4 \frac{T^3}{3\kappa} \frac{\partial T}{\partial m} + L_{conv}. \quad (\text{A.4})$$

- Lagrangian velocity

$$\frac{\partial r}{\partial t} = u. \quad (\text{A.5})$$

Suitable expressions for this set of equations in finite difference form can be found in Section 1.4.1.

Following the same methodology applied to the free-fall collapse problem, three different regions of interest can be distinguished in a computational grid consisting of N concentric shells: the innermost (or central) shell, the $N - 2$ intermediate shells, and the outermost (or surface) shell. The five equations that characterize the innermost shell can be rewritten in compact form as a function, C^j , that depends on eight unknowns:

$$C^j = C^j(\rho_{3/2}, T_{3/2}, r_2, L_2, u_2, \rho_{5/2}, T_{5/2}, r_3) = 0 \quad (j = 1, 5). \quad (\text{A.6})$$

The same approach is applied to the $N - 2$ intermediate shells,

$$F_i^j = F_i^j(r_i, L_i, \rho_{i+1/2}, T_{i+1/2}, r_{i+1}, L_{i+1}, u_{i+1}, \rho_{i+3/2}, T_{i+3/2}, r_{i+2}) = 0 \\ (i = 2, N - 1; j = 1, 5), \quad (\text{A.7})$$

and to the outermost shell,

$$S^j = S^j(r_N, L_N, \rho_{N+1/2}, T_{N+1/2}, r_{N+1}, L_{N+1}, u_{N+1}) = 0. \quad (\text{A.8})$$

The system contains as many unknowns as equations, $5N$ (i.e., 5 for the innermost shell, $5(N - 2)$ for the intermediate shells, and 5 for the surface shell).

As discussed in Section 1.6.6, one may think of a series of values of the unknowns, x^1 , which satisfy the whole set of equations described above. The unknowns x^1 can be determined, through an iterative procedure, from guess values¹ and correction terms, in the form $x^1 = x^0 + \delta X$. Assuming small corrections, δX , the system of equations can be written in the form

$$\begin{aligned} C^j + \frac{\partial C^j}{\partial \rho_{3/2}} \delta \rho_{3/2} + \frac{\partial C^j}{\partial T_{3/2}} \delta T_{3/2} + \frac{\partial C^j}{\partial r_2} \delta r_2 + \frac{\partial C^j}{\partial L_2} \delta L_2 + \frac{\partial C^j}{\partial u_2} \delta u_2 + \\ + \frac{\partial C^j}{\partial \rho_{5/2}} \delta \rho_{5/2} + \frac{\partial C^j}{\partial T_{5/2}} \delta T_{5/2} + \frac{\partial C^j}{\partial r_3} \delta r_3 = 0 \quad (j = 1, 5) \end{aligned} \quad (\text{A.9})$$

$$\begin{aligned} F_i^j + \frac{\partial F_i^j}{\partial r_i} \delta r_i + \frac{\partial F_i^j}{\partial L_i} \delta L_i + \frac{\partial F_i^j}{\partial \rho_{i+1/2}} \delta \rho_{i+1/2} + \frac{\partial F_i^j}{\partial T_{i+1/2}} \delta T_{i+1/2} + \\ + \frac{\partial F_i^j}{\partial r_{i+1}} \delta r_{i+1} + \frac{\partial F_i^j}{\partial L_{i+1}} \delta L_{i+1} + \frac{\partial F_i^j}{\partial u_{i+1}} \delta u_{i+1} + \frac{\partial F_i^j}{\partial \rho_{i+3/2}} \delta \rho_{i+3/2} + \\ + \frac{\partial F_i^j}{\partial T_{i+3/2}} \delta T_{i+3/2} + \frac{\partial F_i^j}{\partial r_{i+2}} \delta r_{i+2} = 0 \quad (i = 2, N - 1; j = 1, 5) \end{aligned} \quad (\text{A.10})$$

$$\begin{aligned} S^j + \frac{\partial S^j}{\partial r_N} \delta r_N + \frac{\partial S^j}{\partial L_N} \delta L_N + \frac{\partial S^j}{\partial \rho_{N+1/2}} \delta \rho_{N+1/2} + \frac{\partial S^j}{\partial T_{N+1/2}} \delta T_{N+1/2} + \\ + \frac{\partial S^j}{\partial r_{N+1}} \delta r_{N+1} + \frac{\partial S^j}{\partial L_{N+1}} \delta L_{N+1} + \frac{\partial S^j}{\partial u_{N+1}} \delta u_{N+1} = 0 \\ (j = 1, 5). \end{aligned} \quad (\text{A.11})$$

Let's focus first on the system of equations corresponding to the innermost shell (Equations A.9): All terms that involve physical variables evaluated at the next shell, $i = 2$ (i.e., $\delta \rho_{5/2}$, $\delta T_{5/2}$, and δr_3), are moved to the right-hand side of the equation, in the form

$$\begin{aligned} \frac{\partial C^j}{\partial \rho_{3/2}} \delta \rho_{3/2} + \frac{\partial C^j}{\partial T_{3/2}} \delta T_{3/2} + \frac{\partial C^j}{\partial u_2} \delta u_2 + \frac{\partial C^j}{\partial L_2} \delta L_2 + \frac{\partial C^j}{\partial r_2} \delta r_2 = \\ -C^j - \frac{\partial C^j}{\partial \rho_{5/2}} \delta \rho_{5/2} - \frac{\partial C^j}{\partial T_{5/2}} \delta T_{5/2} - \frac{\partial C^j}{\partial r_3} \delta r_3 \quad (j = 1, 5), \end{aligned}$$

¹Extrapolation from the last two converged models is frequently used to this end.

which can be rewritten in matrix form as

$$\begin{pmatrix} \frac{\partial C^1}{\partial \rho_{3/2}} & \frac{\partial C^1}{\partial T_{3/2}} & \frac{\partial C^1}{\partial u_2} & \frac{\partial C^1}{\partial L_2} & \frac{\partial C^1}{\partial r_2} \\ \frac{\partial C^2}{\partial \rho_{3/2}} & \frac{\partial C^2}{\partial T_{3/2}} & \frac{\partial C^2}{\partial u_2} & \frac{\partial C^2}{\partial L_2} & \frac{\partial C^2}{\partial r_2} \\ \frac{\partial C^3}{\partial \rho_{3/2}} & \frac{\partial C^3}{\partial T_{3/2}} & \frac{\partial C^3}{\partial u_2} & \frac{\partial C^3}{\partial L_2} & \frac{\partial C^3}{\partial r_2} \\ \frac{\partial C^4}{\partial \rho_{3/2}} & \frac{\partial C^4}{\partial T_{3/2}} & \frac{\partial C^4}{\partial u_2} & \frac{\partial C^4}{\partial L_2} & \frac{\partial C^4}{\partial r_2} \\ \frac{\partial C^5}{\partial \rho_{3/2}} & \frac{\partial C^5}{\partial T_{3/2}} & \frac{\partial C^5}{\partial u_2} & \frac{\partial C^5}{\partial L_2} & \frac{\partial C^5}{\partial r_2} \end{pmatrix} \begin{pmatrix} \delta \rho_{3/2} \\ \delta T_{3/2} \\ \delta u_2 \\ \delta L_2 \\ \delta r_2 \end{pmatrix} = \begin{pmatrix} -C^1 - \frac{\partial C^1}{\partial \rho_{5/2}} \delta \rho_{5/2} - \frac{\partial C^1}{\partial T_{5/2}} \delta T_{5/2} - \frac{\partial C^1}{\partial r_3} \delta r_3 \\ -C^2 - \frac{\partial C^2}{\partial \rho_{5/2}} \delta \rho_{5/2} - \frac{\partial C^2}{\partial T_{5/2}} \delta T_{5/2} - \frac{\partial C^2}{\partial r_3} \delta r_3 \\ -C^3 - \frac{\partial C^3}{\partial \rho_{5/2}} \delta \rho_{5/2} - \frac{\partial C^3}{\partial T_{5/2}} \delta T_{5/2} - \frac{\partial C^3}{\partial r_3} \delta r_3 \\ -C^4 - \frac{\partial C^4}{\partial \rho_{5/2}} \delta \rho_{5/2} - \frac{\partial C^4}{\partial T_{5/2}} \delta T_{5/2} - \frac{\partial C^4}{\partial r_3} \delta r_3 \\ -C^5 - \frac{\partial C^5}{\partial \rho_{5/2}} \delta \rho_{5/2} - \frac{\partial C^5}{\partial T_{5/2}} \delta T_{5/2} - \frac{\partial C^5}{\partial r_3} \delta r_3 \end{pmatrix}. \quad (\text{A.12})$$

Note that the matrix at the right-hand side of Equation A.12 has dimensions 5×1 .

Corrections to the variables evaluated at the innermost shell (i.e., $\delta \rho_{3/2}$, $\delta T_{3/2}$, δr_2 , δL_2 , δu_2) can be conveniently expressed as a linear function of those variables evaluated at the next shell (i.e., $\delta \rho_{5/2}$, $\delta T_{5/2}$, δr_3), which are taken as parameters [824]

$$\begin{aligned} \delta \rho_{3/2} &= A_{12} \delta \rho_{5/2} + B_{12} \delta T_{5/2} + C_{12} \delta r_3 + D_{12} \\ \delta T_{3/2} &= A_{22} \delta \rho_{5/2} + B_{22} \delta T_{5/2} + C_{22} \delta r_3 + D_{22} \\ \delta u_2 &= A_{32} \delta \rho_{5/2} + B_{32} \delta T_{5/2} + C_{32} \delta r_3 + D_{32} \\ \delta L_2 &= A_{42} \delta \rho_{5/2} + B_{42} \delta T_{5/2} + C_{42} \delta r_3 + D_{42} \\ \delta r_2 &= A_{52} \delta \rho_{5/2} + B_{52} \delta T_{5/2} + C_{52} \delta r_3 + D_{52}. \end{aligned} \quad (\text{A.13})$$

Equivalently,

$$\begin{pmatrix} \delta \rho_{3/2} \\ \delta T_{3/2} \\ \delta u_2 \\ \delta L_2 \\ \delta r_2 \end{pmatrix} = \begin{pmatrix} A_{12} & B_{12} & C_{12} & D_{12} \\ A_{22} & B_{22} & C_{22} & D_{22} \\ A_{32} & B_{32} & C_{32} & D_{32} \\ A_{42} & B_{42} & C_{42} & D_{42} \\ A_{52} & B_{52} & C_{52} & D_{52} \end{pmatrix} \begin{pmatrix} \delta \rho_{5/2} \\ \delta T_{5/2} \\ \delta r_3 \\ 1 \end{pmatrix}. \quad (\text{A.14})$$

Moreover, the matrix at the right-hand side of Equation A.12 can be rewritten as the product

$$\begin{pmatrix} -C^1 - \frac{\partial C^1}{\partial \rho_{5/2}} \delta \rho_{5/2} - \frac{\partial C^1}{\partial T_{5/2}} \delta T_{5/2} - \frac{\partial C^1}{\partial r_3} \delta r_3 \\ -C^2 - \frac{\partial C^2}{\partial \rho_{5/2}} \delta \rho_{5/2} - \frac{\partial C^2}{\partial T_{5/2}} \delta T_{5/2} - \frac{\partial C^2}{\partial r_3} \delta r_3 \\ -C^3 - \frac{\partial C^3}{\partial \rho_{5/2}} \delta \rho_{5/2} - \frac{\partial C^3}{\partial T_{5/2}} \delta T_{5/2} - \frac{\partial C^3}{\partial r_3} \delta r_3 \\ -C^4 - \frac{\partial C^4}{\partial \rho_{5/2}} \delta \rho_{5/2} - \frac{\partial C^4}{\partial T_{5/2}} \delta T_{5/2} - \frac{\partial C^4}{\partial r_3} \delta r_3 \\ -C^5 - \frac{\partial C^5}{\partial \rho_{5/2}} \delta \rho_{5/2} - \frac{\partial C^5}{\partial T_{5/2}} \delta T_{5/2} - \frac{\partial C^5}{\partial r_3} \delta r_3 \end{pmatrix} =$$

$$\begin{pmatrix} -\frac{\partial C^1}{\partial \rho_{5/2}} & -\frac{\partial C^1}{\partial T_{5/2}} & -\frac{\partial C^1}{\partial r_3} & -C^1 \\ -\frac{\partial C^2}{\partial \rho_{5/2}} & -\frac{\partial C^2}{\partial T_{5/2}} & -\frac{\partial C^2}{\partial r_3} & -C^2 \\ -\frac{\partial C^3}{\partial \rho_{5/2}} & -\frac{\partial C^3}{\partial T_{5/2}} & -\frac{\partial C^3}{\partial r_3} & -C^3 \\ -\frac{\partial C^4}{\partial \rho_{5/2}} & -\frac{\partial C^4}{\partial T_{5/2}} & -\frac{\partial C^4}{\partial r_3} & -C^4 \\ -\frac{\partial C^5}{\partial \rho_{5/2}} & -\frac{\partial C^5}{\partial T_{5/2}} & -\frac{\partial C^5}{\partial r_3} & -C^5 \end{pmatrix} \begin{pmatrix} \delta \rho_{5/2} \\ \delta T_{5/2} \\ \delta r_3 \\ 1 \end{pmatrix}. \quad (\text{A.15})$$

Plugging Equations A.14 and A.15 into Equation A.12 yields

$$\begin{pmatrix} \frac{\partial C^1}{\partial \rho_{3/2}} & \frac{\partial C^1}{\partial T_{3/2}} & \frac{\partial C^1}{\partial u_2} & \frac{\partial C^1}{\partial L_2} & \frac{\partial C^1}{\partial r_2} \\ \frac{\partial C^2}{\partial \rho_{3/2}} & \frac{\partial C^2}{\partial T_{3/2}} & \frac{\partial C^2}{\partial u_2} & \frac{\partial C^2}{\partial L_2} & \frac{\partial C^2}{\partial r_2} \\ \frac{\partial C^3}{\partial \rho_{3/2}} & \frac{\partial C^3}{\partial T_{3/2}} & \frac{\partial C^3}{\partial u_2} & \frac{\partial C^3}{\partial L_2} & \frac{\partial C^3}{\partial r_2} \\ \frac{\partial C^4}{\partial \rho_{3/2}} & \frac{\partial C^4}{\partial T_{3/2}} & \frac{\partial C^4}{\partial u_2} & \frac{\partial C^4}{\partial L_2} & \frac{\partial C^4}{\partial r_2} \\ \frac{\partial C^5}{\partial \rho_{3/2}} & \frac{\partial C^5}{\partial T_{3/2}} & \frac{\partial C^5}{\partial u_2} & \frac{\partial C^5}{\partial L_2} & \frac{\partial C^5}{\partial r_2} \end{pmatrix} \begin{pmatrix} A_{12} & B_{12} & C_{12} & D_{12} \\ A_{22} & B_{22} & C_{22} & D_{22} \\ A_{32} & B_{32} & C_{32} & D_{32} \\ A_{42} & B_{42} & C_{42} & D_{42} \\ A_{52} & B_{52} & C_{52} & D_{52} \end{pmatrix} =$$

$$\begin{pmatrix} -\frac{\partial C^1}{\partial \rho_{5/2}} - \frac{\partial C^1}{\partial T_{5/2}} - \frac{\partial C^1}{\partial r_3} - C^1 \\ -\frac{\partial C^2}{\partial \rho_{5/2}} - \frac{\partial C^2}{\partial T_{5/2}} - \frac{\partial C^2}{\partial r_3} - C^2 \\ -\frac{\partial C^3}{\partial \rho_{5/2}} - \frac{\partial C^3}{\partial T_{5/2}} - \frac{\partial C^3}{\partial r_3} - C^3 \\ -\frac{\partial C^4}{\partial \rho_{5/2}} - \frac{\partial C^4}{\partial T_{5/2}} - \frac{\partial C^4}{\partial r_3} - C^4 \\ -\frac{\partial C^5}{\partial \rho_{5/2}} - \frac{\partial C^5}{\partial T_{5/2}} - \frac{\partial C^5}{\partial r_3} - C^5 \end{pmatrix}, \quad (\text{A.16})$$

from which constants A_{k2}, B_{k2}, C_{k2} , and D_{k2} ($k = 1, 5$) can be obtained.

The outlined procedure is subsequently extended to the $N - 2$ intermediate shells. First, the linear dependence between variables evaluated at the first and second shells described above (Equation A.13) is generalized for shells $(i - 1)^{th}$ and i^{th} as follows:

$$\begin{aligned}\delta\rho_{i-1/2} &= A_{1i}\delta\rho_{i+1/2} + B_{1i}\delta T_{i+1/2} + C_{1i}\delta r_{i+1} + D_{1i} \\ \delta T_{i-1/2} &= A_{2i}\delta\rho_{i+1/2} + B_{2i}\delta T_{i+1/2} + C_{2i}\delta r_{i+1} + D_{2i} \\ \delta u_i &= A_{3i}\delta\rho_{i+1/2} + B_{3i}\delta T_{i+1/2} + C_{3i}\delta r_{i+1} + D_{3i} \\ \delta L_i &= A_{4i}\delta\rho_{i+1/2} + B_{4i}\delta T_{i+1/2} + C_{4i}\delta r_{i+1} + D_{4i} \\ \delta r_i &= A_{5i}\delta\rho_{i+1/2} + B_{5i}\delta T_{i+1/2} + C_{5i}\delta r_{i+1} + D_{5i}.\end{aligned}\quad (\text{A.17})$$

Plugging the last two relations, for δL_i and δr_i , into Equation A.10 yields

$$\begin{aligned}&\left[\frac{\partial F_i^j}{\partial \rho_{i+1/2}} + A_{4i} \frac{\partial F_i^j}{\partial L_i} + A_{5i} \frac{\partial F_i^j}{\partial r_i} \right] \delta\rho_{i+1/2} + \left[\frac{\partial F_i^j}{\partial T_{i+1/2}} + B_{4i} \right. \\ &\left. \frac{\partial F_i^j}{\partial L_i} + B_{5i} \frac{\partial F_i^j}{\partial r_i} \right] \delta T_{i+1/2} + \frac{\partial F_i^j}{\partial u_{i+1}} \delta u_{i+1} + \frac{\partial F_i^j}{\partial L_{i+1}} \delta L_{i+1} + \left[\frac{\partial F_i^j}{\partial r_{i+1}} + C_{4i} \frac{\partial F_i^j}{\partial L_i} + \right. \\ &\left. + C_{5i} \frac{\partial F_i^j}{\partial r_i} \right] \delta r_{i+1} + \frac{\partial F_i^j}{\partial \rho_{i+3/2}} \delta\rho_{i+3/2} + \frac{\partial F_i^j}{\partial T_{i+3/2}} \delta T_{i+3/2} + \frac{\partial F_i^j}{\partial r_{i+2}} \delta r_{i+2} = \\ &-F_i^j - D_{4i} \frac{\partial F_i^j}{\partial L_i} + D_{5i} \frac{\partial F_i^j}{\partial r_i} \quad (j = 1, 5),\end{aligned}\quad (\text{A.18})$$

which represents a system of 5 linearized equations with 8 unknowns. For convenience, three of the unknowns are, as before, taken as parameters and subsequently moved to the right-hand side of the equation, in the form

$$\begin{aligned}&\alpha_i^j \delta\rho_{i+1/2} + \beta_i^j \delta T_{i+1/2} + \frac{\partial F_i^j}{\partial u_{i+1}} \delta u_{i+1} + \frac{\partial F_i^j}{\partial L_{i+1}} \delta L_{i+1} + \gamma_i^j \delta r_{i+1} + \frac{\partial F_i^j}{\partial \rho_{i+3/2}} \delta\rho_{i+3/2} + \\ &+ \frac{\partial F_i^j}{\partial T_{i+3/2}} \delta T_{i+3/2} + \frac{\partial F_i^j}{\partial r_{i+2}} \delta r_{i+2} = -F_i^j - D_{4i} \frac{\partial F_i^j}{\partial L_i} - \\ &- D_{5i} \frac{\partial F_i^j}{\partial r_i} \quad (j = 1, 5),\end{aligned}\quad (\text{A.19})$$

where

$$\begin{aligned}\alpha_i^j &\equiv \frac{\partial F_i^j}{\partial \rho_{i+1/2}} + A_{4i} \frac{\partial F_i^j}{\partial L_i} + A_{5i} \frac{\partial F_i^j}{\partial r_i} \\ \beta_i^j &\equiv \frac{\partial F_i^j}{\partial T_{i+1/2}} + B_{4i} \frac{\partial F_i^j}{\partial L_i} + B_{5i} \frac{\partial F_i^j}{\partial r_i} \\ \gamma_i^j &\equiv \frac{\partial F_i^j}{\partial r_{i+1}} + C_{4i} \frac{\partial F_i^j}{\partial L_i} + C_{5i} \frac{\partial F_i^j}{\partial r_i}.\end{aligned}$$

Equation A.19 can now be written in the matrix form

$$\begin{pmatrix} \alpha_i^1 & \beta_i^1 & \frac{\partial F_i^1}{\partial u_{i+1}} & \frac{\partial F_i^1}{\partial L_{i+1}} & \gamma_i^1 \\ \alpha_i^2 & \beta_i^2 & \frac{\partial F_i^2}{\partial u_{i+1}} & \frac{\partial F_i^2}{\partial L_{i+1}} & \gamma_i^2 \\ \alpha_i^3 & \beta_i^3 & \frac{\partial F_i^3}{\partial u_{i+1}} & \frac{\partial F_i^3}{\partial L_{i+1}} & \gamma_i^3 \\ \alpha_i^4 & \beta_i^4 & \frac{\partial F_i^4}{\partial u_{i+1}} & \frac{\partial F_i^4}{\partial L_{i+1}} & \gamma_i^4 \\ \alpha_i^5 & \beta_i^5 & \frac{\partial F_i^5}{\partial u_{i+1}} & \frac{\partial F_i^5}{\partial L_{i+1}} & \gamma_i^5 \end{pmatrix} \begin{pmatrix} \delta\rho_{i+1/2} \\ \delta T_{i+1/2} \\ \delta u_{i+1} \\ \delta L_{i+1} \\ \delta r_{i+1} \end{pmatrix} = \begin{pmatrix} \delta_i^1 \\ \delta_i^2 \\ \delta_i^3 \\ \delta_i^4 \\ \delta_i^5 \end{pmatrix}, \quad (\text{A.20})$$

where

$$\begin{aligned} \delta_i^j \equiv & -F_i^j - D_{4i} \frac{\partial F_i^j}{\partial L_i} - D_{5i} \frac{\partial F_i^j}{\partial r_i} - \frac{\partial F_i^j}{\partial \rho_{i+3/2}} \delta\rho_{i+3/2} - \\ & - \frac{\partial F_i^j}{\partial T_{i+3/2}} \delta T_{i+3/2} - \frac{\partial F_i^j}{\partial r_{i+2}} \delta r_{i+2}. \end{aligned}$$

Expressing the 5 unknowns of the i^{th} shell in terms of the variables $\delta\rho_{i+3/2}, \delta T_{i+3/2}$, and δr_{i+2} ,

$$\begin{aligned} \delta\rho_{i+1/2} &= A_{1,i+1} \delta\rho_{i+3/2} + B_{1,i+1} \delta T_{i+3/2} + C_{1,i+1} \delta r_{i+2} + D_{1,i+1} \\ \delta T_{i+1/2} &= A_{2,i+1} \delta\rho_{i+3/2} + B_{2,i+1} \delta T_{i+3/2} + C_{2,i+1} \delta r_{i+2} + D_{2,i+1} \\ \delta u_{i+1} &= A_{3,i+1} \delta\rho_{i+3/2} + B_{3,i+1} \delta T_{i+3/2} + C_{3,i+1} \delta r_{i+2} + D_{3,i+1} \\ \delta L_{i+1} &= A_{4,i+1} \delta\rho_{i+3/2} + B_{4,i+1} \delta T_{i+3/2} + C_{4,i+1} \delta r_{i+2} + D_{4,i+1} \\ \delta r_{i+1} &= A_{5,i+1} \delta\rho_{i+3/2} + B_{5,i+1} \delta T_{i+3/2} + C_{5,i+1} \delta r_{i+2} + D_{5,i+1}, \end{aligned}$$

the constants $A_{k,i+l}, B_{k,i+l}, C_{k,i+l}$, and $D_{k,i+l}$ ($k = 1, 5$; $i = 2, N - 1$) can be determined by solving the matrix system

$$\begin{pmatrix} \alpha_i^1 & \beta_i^1 & \frac{\partial F_i^1}{\partial u_{i+1}} & \frac{\partial F_i^1}{\partial L_{i+1}} & \gamma_i^1 \\ \alpha_i^2 & \beta_i^2 & \frac{\partial F_i^2}{\partial u_{i+1}} & \frac{\partial F_i^2}{\partial L_{i+1}} & \gamma_i^2 \\ \alpha_i^3 & \beta_i^3 & \frac{\partial F_i^3}{\partial u_{i+1}} & \frac{\partial F_i^3}{\partial L_{i+1}} & \gamma_i^3 \\ \alpha_i^4 & \beta_i^4 & \frac{\partial F_i^4}{\partial u_{i+1}} & \frac{\partial F_i^4}{\partial L_{i+1}} & \gamma_i^4 \\ \alpha_i^5 & \beta_i^5 & \frac{\partial F_i^5}{\partial u_{i+1}} & \frac{\partial F_i^5}{\partial L_{i+1}} & \gamma_i^5 \end{pmatrix} \begin{pmatrix} A_{1,i+1} & B_{1,i+1} & C_{1,i+1} & D_{1,i+1} \\ A_{2,i+1} & B_{2,i+1} & C_{2,i+1} & D_{2,i+1} \\ A_{3,i+1} & B_{3,i+1} & C_{3,i+1} & D_{3,i+1} \\ A_{4,i+1} & B_{4,i+1} & C_{4,i+1} & D_{4,i+1} \\ A_{5,i+1} & B_{5,i+1} & C_{5,i+1} & D_{5,i+1} \end{pmatrix} =$$

$$\begin{pmatrix} -\frac{\partial F_i^1}{\partial \rho_{i+3/2}} & -\frac{\partial F_i^1}{\partial T_{3+1/2}} & -\frac{\partial F_i^1}{\partial r_{i+2}} & \epsilon_i^1 \\ -\frac{\partial F_i^2}{\partial \rho_{i+3/2}} & -\frac{\partial F_i^2}{\partial T_{3+1/2}} & -\frac{\partial F_i^2}{\partial r_{i+2}} & \epsilon_i^2 \\ -\frac{\partial F_i^3}{\partial \rho_{i+3/2}} & -\frac{\partial F_i^3}{\partial T_{3+1/2}} & -\frac{\partial F_i^3}{\partial r_{i+2}} & \epsilon_i^3 \\ -\frac{\partial F_i^4}{\partial \rho_{i+3/2}} & -\frac{\partial F_i^4}{\partial T_{3+1/2}} & -\frac{\partial F_i^4}{\partial r_{i+2}} & \epsilon_i^4 \\ -\frac{\partial F_i^5}{\partial \rho_{i+3/2}} & -\frac{\partial F_i^5}{\partial T_{3+1/2}} & -\frac{\partial F_i^5}{\partial r_{i+2}} & \epsilon_i^5 \end{pmatrix}, \quad (\text{A.21})$$

where

$$\epsilon_i^j \equiv -F_i^j - D_{4i} \frac{\partial F_i^j}{\partial L_i} - D_{5i} \frac{\partial F_i^j}{\partial r_i}.$$

Finally, the same procedure is applied to the system of equations for the outermost shell. Expressing all variables in terms of quantities belonging to the N^{th} shell,

$$\begin{aligned} \delta\rho_{N-1/2} &= A_{1N}\delta\rho_{N+1/2} + B_{1N}\delta T_{N+1/2} + C_{1N}\delta r_{N+1} + D_{1N} \\ \delta T_{N-1/2} &= A_{2N}\delta\rho_{N+1/2} + B_{2N}\delta T_{N+1/2} + C_{2N}\delta r_{N+1} + D_{2N} \\ \delta u_N &= A_{3N}\delta\rho_{N+1/2} + B_{3N}\delta T_{N+1/2} + C_{3N}\delta r_{N+1} + D_{3N} \\ \delta L_N &= A_{4N}\delta\rho_{N+1/2} + B_{4N}\delta T_{N+1/2} + C_{4N}\delta r_{N+1} + D_{4N} \\ \delta r_N &= A_{5N}\delta\rho_{N+1/2} + B_{5N}\delta T_{N+1/2} + C_{5N}\delta r_{N+1} + D_{5N}, \end{aligned}$$

and, subsequently, plugging these relations into the system of linearized equations for the surface layer, Equations A.11, yields

$$\begin{aligned} &\left[\frac{\partial S^j}{\partial \rho_{N+1/2}} + A_{4N} \frac{\partial S^j}{\partial L_N} + A_{5N} \frac{\partial S^j}{\partial r_N} \right] \delta\rho_{N+1/2} + \left[\frac{\partial S^j}{\partial T_{N+1/2}} + B_{4N} \frac{\partial S^j}{\partial L_N} + \right. \\ &\left. + B_{5N} \frac{\partial S^j}{\partial r_N} \right] \delta T_{N+1/2} + \frac{\partial S^j}{\partial u_{N+1}} \delta u_{N+1} + \frac{\partial S^j}{\partial L_{N+1}} \delta L_{N+1} + \left[\frac{\partial S^j}{\partial r_{N+1}} + C_{4N} \frac{\partial S^j}{\partial L_N} + \right. \\ &\left. + C_{5N} \frac{\partial S^j}{\partial r_N} \right] \delta r_{N+1} = -S^j - D_{4N} \frac{\partial S^j}{\partial L_N} + D_{5N} \frac{\partial S^j}{\partial r_N} \\ &\quad (j = 1, 5). \end{aligned} \quad (\text{A.22})$$

Equation A.22 can now be rewritten in the following matrix form

$$\begin{pmatrix} \alpha_{N+1}^1 & \beta_{N+1}^1 & \frac{\partial S^1}{\partial u_{N+1}} & \frac{\partial S^1}{\partial L_{N+1}} & \gamma_{N+1}^1 \\ \alpha_{N+1}^2 & \beta_{N+1}^2 & \frac{\partial S^2}{\partial u_{N+1}} & \frac{\partial S^2}{\partial L_{N+1}} & \gamma_{N+1}^2 \\ \alpha_{N+1}^3 & \beta_{N+1}^3 & \frac{\partial S^3}{\partial u_{N+1}} & \frac{\partial S^3}{\partial L_{N+1}} & \gamma_{N+1}^3 \\ \alpha_{N+1}^4 & \beta_{N+1}^4 & \frac{\partial S^4}{\partial u_{N+1}} & \frac{\partial S^4}{\partial L_{N+1}} & \gamma_{N+1}^4 \\ \alpha_{N+1}^5 & \beta_{N+1}^5 & \frac{\partial S^5}{\partial u_{N+1}} & \frac{\partial S^5}{\partial L_{N+1}} & \gamma_{N+1}^5 \end{pmatrix} \begin{pmatrix} \delta\rho_{N+1/2} \\ \delta T_{N+1/2} \\ \delta u_{N+1} \\ \delta L_{N+1} \\ \delta r_{N+1} \end{pmatrix} =$$

$$\begin{pmatrix} \delta_{N+1}^1 \\ \delta_{N+1}^2 \\ \delta_{N+1}^3 \\ \delta_{N+1}^4 \\ \delta_{N+1}^5 \end{pmatrix}, \quad (\text{A.23})$$

where

$$\begin{aligned} \alpha_{N+1}^j &\equiv \frac{\partial S^j}{\partial \rho_{N+1/2}} + A_{4N} \frac{\partial S^j}{\partial L_N} + A_{5N} \frac{\partial S^j}{\partial r_N} \\ \beta_{N+1}^j &\equiv \frac{\partial S^j}{\partial T_{N+1/2}} + B_{4N} \frac{\partial S^j}{\partial L_N} + B_{5N} \frac{\partial S^j}{\partial r_N} \\ \gamma_{N+1}^j &\equiv \frac{\partial S^j}{\partial r_{N+1}} + C_{4N} \frac{\partial S^j}{\partial L_N} + C_{5N} \frac{\partial S^j}{\partial r_N} \\ \delta_{N+1}^j &\equiv -S^j - D_{4N} \frac{\partial S^j}{\partial L_N} - D_{5N} \frac{\partial S^j}{\partial r_N}. \end{aligned}$$

The solution of this matrix equation yields a first set of corrections for the variables belonging to the surface layer, $\delta\rho_{N+1/2}$, $\delta T_{N+1/2}$, δu_{N+1} , δL_{N+1} , and δr_{N+1} . From these values, and the stored auxiliar quantities A_{kl} , B_{kl} , C_{kl} , and D_{kl} ($k = 1, 5; l = 2, N$), first corrections to the variables for the whole grid can also be obtained:

$$\begin{aligned} \delta\rho_{i-1/2} &= A_{1,i} \delta\rho_{i+1/2} + B_{1,i} \delta T_{i+1/2} + C_{1,i} \delta r_{i+1} + D_{1,i} \\ \delta T_{i-1/2} &= A_{2,i} \delta\rho_{i+1/2} + B_{2,i} \delta T_{i+1/2} + C_{2,i} \delta r_{i+1} + D_{2,i} \\ \delta u_i &= A_{3,i} \delta\rho_{i+1/2} + B_{3,i} \delta T_{i+1/2} + C_{3,i} \delta r_{i+1} + D_{3,i} \\ \delta L_i &= A_{4,i} \delta\rho_{i+1/2} + B_{4,i} \delta T_{i+1/2} + C_{4,i} \delta r_{i+1} + D_{4,i} \\ \delta r_i &= A_{5,i} \delta\rho_{i+1/2} + B_{5,i} \delta T_{i+1/2} + C_{5,i} \delta r_{i+1} + D_{5,i} \\ &\quad (i = N, 2). \end{aligned}$$

These corrections are finally applied to the first guess values, in the form

$$\begin{aligned} \rho_{i+1/2}^1 &= \rho_{i+1/2}^o + \delta\rho_{i+1/2} \\ T_{i+1/2}^1 &= T_{i+1/2}^o + \delta T_{i+1/2} \\ u_{i+1}^1 &= u_{i+1}^o + \delta u_{i+1} \\ L_{i+1}^1 &= L_{i+1}^o + \delta L_{i+1} \\ r_{i+1}^1 &= r_{i+1}^o + \delta r_{i+1} \quad (i = 1, N). \end{aligned}$$

The overall procedure is then iterated until a given accuracy criterion (i.e., corrections smaller than a given quantity) is satisfied.